NANO-STRUCTURED MICRO-GRANULES: SYNTHESIS AND CHARACTERIZATION

By

PRIYANKA BISWAS
Enrolment No. PHYS01201404010

Bhabha Atomic Research Centre, Mumbai

A thesis submitted to the
Board of Studies in Physical Sciences
In partial fulfillment of requirements
for the Degree of

DOCTOR OF PHILOSOPHY
of
HOMI BHABHA NATIONAL INSTITUTE

June, 2018

Homi Bhabha National Institute[1]

Recommendations of the Viva Voce Committee

As members of the Viva Voce Committee, we certify that we have read the dissertation prepared by **Ms. Priyanka Biswas** entitled **Nano-structured Micro-granules: Synthesis and Characterization** and recommend that it may be accepted as fulfilling the thesis requirement for the award of Degree of Doctor of Philosophy.

Chairman – Dr. Saibal Basu **Date:** 09/01/2019

Debasis Sen. 09/01/2019

Guide / Convener – Dr. Debasis Sen **Date:** 09/01/2019

Examiner – Dr. Vivek Polshettiwar **Date:**

09-01-2019

Member 1- Dr. P.A. Hassan **Date:**

Tmahata 09.01.2019.

Member 2- Dr. T. Mahata **Date:**

Dr. A.K. Pandey Pandey 9.1.2019

Final approval and acceptance of this thesis is contingent upon the candidate's submission of the final copies of the thesis to HBNI.

I/We hereby certify that I/we have read this thesis prepared under my/our direction and recommend that it may be accepted as fulfilling the thesis requirement.

Date: 09/01/2019

Place: Mumbai

Debasis Sen.

Guide

---

[1] This page is to be included only for final submission after successful completion of viva voce.

STATEMENT BY AUTHOR

This dissertation has been submitted in partial fulfillment of requirements for an advanced degree at Homi Bhabha National Institute (HBNI) and is deposited in the Library to be made available to borrowers under rules of the HBNI.

Brief quotations from this dissertation are allowable without special permission, provided that accurate acknowledgement of source is made. Requests for permission for extended quotation from or reproduction of this manuscript in whole or in part may be granted by the Competent Authority of HBNI when in his or her judgment the proposed use of the material is in the interests of scholarship. In all other instances, however, permission must be obtained from the author.

(Priyanka Biswas)

DECLARATION

I, hereby declare that the investigation presented in the thesis has been carried out by me. The work is original and has not been submitted earlier as a whole or in part for a degree/ diploma at this or any other Institution / University.

(Priyanka Biswas)

List of Publications arising from the thesis

Journal

1. “Temperature mediated morphological transition during drying of spray colloidal droplets”
   Priyanka Biswas, D. Sen, S. Mazumder, C.B. Basak and P. Doshi
   Langmuir, **2016**, *32*, 2464-2473.

2. “Porous Microcapsules Comprised Inter-locked Nano-particles by Evaporation-Induced Assembly: Evaluation of Dye Sorption”
   Priyanka Biswas, D. Sen, S. Mazumder and Jayshree Ramkumar
   Colloids Surf. A, **2017**, *520*, 279–288.

3. “Porous nano-structured micro-granules from silica milk bi-colloidal suspension: Synthesis and characterization”
   Priyanka Biswas, D. Sen, S. Mazumder, J. S. Melo, C. B. Basak and Kinshuk Dasgupta
   Colloids Surf. B, **2017**, *154*, 421-428. **[Journal cover page article]**

4. “Colloidal Interaction Induced Surface Modulation on Spray-dried Micro-granules”
   Priyanka Biswas, D. Sen, Jae-Min Ha and Sung-Min Choi
   J. Colloid Interface Sci., **2019**, *538*, 149-158

5. “Investigation of morphological variation of spray-dried nanostructured microgranules using SESANS”
   Priyanka Biswas, D. Sen and W. Bouwman
   Under preparation

6. “Comparability of scattering, thermal and gas adsorption in probing nano-porous micro-granules”
   Priyanka Biswas, D. Sen, Sarita, Sudip Sarkar, A. Biswas, Kinshuk Dasgupta
   Under preparation

Conferences

1. "Inter-particle Interaction Dependent Evaporation-Induced Assembly in Contact-Free Micro-colloidal Droplets"
   D. Sen, **Priyanka Biswas** and J.S. Melo
   AIP Conf. Proc., **2018**, *1942*, 040003.

2. "Controlling Sphere to Doughnut Transformation during Quick Drying of Colloidal Micrometric Droplets"
   Priyanka Biswas, D. Sen, S. Mazumder, and P. Doshi
   AIP Conf. Proc., **2017**, *1832*, 140009.

3. "Contact-free drying of Colloidal droplets: Effect of Interparticle Interactions"
   Priyanka Biswas and D. Sen
   IACIS Conference, Rotterdam, the Netherlands, **2018**. **[Oral Presentation]**

4. "Effect of Inter-particle Interactions in Drying Colloidal Droplets"
   Priyanka Biswas and D. Sen
   Mumbai-Pune Soft Matter Meet, BARC. Mumbai, India, **2017. [Oral Presentation]**

5. "Evaporative Assembly of Bi-colloids: An Effective Route in Realizing Porous Microgranules"
   Priyanka Biswas, D. Sen and J.S. Melo
   Conference on Neutron Scattering, BARC, Mumbai, India, **2016**.

6. "Dye Sorption Evaluation by Nano-structured Silica Micro-granule"
   Priyanka Biswas, D. Sen and J. Ramkumar
   Mumbai-Pune Soft Matter Meet, NCL, Pune, India, **2016**.

7. "Nano-structured Silica Micro-granule: Synthesis, Characterization and Pore-generation"
   Priyanka Biswas, D. Sen and J.S. Melo
   MCM Symposium, Goa University, Goa, India, **2016**. **[Best Poster Award]**

8. "Porous Nano-structured Silica Micro-granule: Synthesis and Characterization"
   Priyanka Biswas, D. Sen and J.S. Melo
   NANOS Conference, Geetam University, Vizag, India, **2015**. **[Oral Presentation]**

9. “Nano-structured Spray-dried Micro-granules: Synthesis and Characterization”
Priyanka Biswas and D. Sen
International Conference on Electron Microscopy, Mumbai, India, **2015**.

10. “Use of Small Angle Scattering to Investigate Nano-structured Spray-dried Silica Microgranules”
Priyanka Biswas and D. Sen
Conference on Neutron Scattering, HBCSE, Mumbai, India, **2015**.

11. “Spray Dried Nano-structured Microgranules: Synthesis, Mesoscopic Structure and Dye Uptake”
Priyanka Biswas, D. Sen and J. Ramkumar
DAE Solid State Physics Symposium, VIT, Chennai, India, **2014.**

12. “Sorption of Cationic Dye by Spray Dried Nanostructured Silica Micro-granules”
Priyanka Biswas, D. Sen and J. Ramkumar
DAE- BRNS 5th Interdisciplinary Symposium on Materials Chemistry, BARC, Mumbai, India, **2014.**

Workshops attended

1. 7th AONSA School on Neutron Scattering (**2015**), J-PARC, Tokai, Japan.

2. 36th Berlin School on Neutron Scattering (**2016**), HZB, Berlin, Germany.

(Priyanka Biswas)

For

Rohan (1999-2013)

ACKNOWLEDGEMENTS

Firstly I would start by thanking the person who perhaps has the biggest contribution to my scientific inquisitiveness. Words are simply not enough to describe how truly blessed I am to have had Dr. Debasis Sen as my advisor. He is a true mentor, who not only guided me but also inspired me since the first day of my research career. I consider myself truly accomplished to have inculcated a tiny fraction of the perseverance, patience and the eye for perfection that he has.

I express my heartfelt thanks to Late Dr. S. Mazumder, because of whom I got an opportunity to work at the MSANS instrument at Dhruva reactor, Trombay and SAXS. I thank Dr. R Mukhopadhyay, former head of SSPD and Dr. S. L. Chaplot, former Physics Group Director for giving me a chance to be a part of SSPD, BARC. I am grateful to my doctoral committee members, former SSPD head Dr. S. Basu, Dr. P. A. Hassan, Dr. T. Mahata and Dr. A. K. Pandey for their constructive criticisms, suggestions and help throughout my tenure. Earnest thanks to my collaborators, Dr. J. S. Melo, Dr. J. Ramkumar, Dr. P. Doshi, Dr. C. B. Basak, Dr. K. Dasgupta, Dr. S.-M. Choi and Dr. W. Bouwman who gave me a chance to explore and learn about various other experimental techniques. I especially thank Dr. S. M. Yusuf, Head, SSPD and Dr. V. K. Aswal, Head, MSAS section for their valuable help and guidance. I express my gratitude to Dr. Jitendra Bahadur and Dr. Sugam Kumar for their support and help.

I am extremely grateful to my parents who have been supportive of my career choices and have encouraged me through the thick and thin; my extended family in Calcutta, especially my *Didun* (maternal grandmother) who is always enthusiastically curious about my work!

The five years in Mumbai would have been very difficult without the company of the wonderful friends here. Firstly, I thank my training school batch-mates. I will always cherish the fond memories with Saheli, Raj, Sushant, Debashish, Swayam, Swapan and Indresh during the training period. I thank my other PhD-mates, Baltej, Purushottam, Dipayan, Sumit, Rakhee, Samatha and others with whom I could share the ups and downs of research life. Thanks to my juniors, Harish, Pulkit, Sourabh, Madhu, Meera who made my life here enjoyable.

I specially thank Debes and Avik *da* for catering to all my incessant queries and requests, academic or otherwise, patiently; Debashish *da*, for our varied discussions during tea breaks and (timely) lunches.

Thank you Neetika *di*, Pallavi and Ganesh, you made my hostel life so enjoyable and delicious! I also thank Farida aunty for the homemade lunch boxes she brought for me.

However much I hate to admit but thank you Niranjan for being so brutally honest.

I have to thank Indresh (yet again) for helping me survive PhD life. I am truly blessed to have a friend like you.

The list of acknowledgement wouldn’t be complete without thanking my teachers at different stages of my academic life. I would specially mention Arun Sir (Arun Mukherjee), who seeded the love for Physics in me.

And last but not the least, I cannot really put into words the immense love and unwavering support I received from Dr. Sunder Sahayanathan and family throughout these five years in Mumbai. It is almost serendipitous to have met you, Rosey and Alvin who have become my second family now. I would also like to express my gratitude to Kunda aunty, Nijil and Jubina. People like you give meaning to human relationships and bonding. Thank you all for everything!

CONTENTS

Homi Bhabha National Institute

SYNOPSIS OF Ph. D. THESIS

1. **Name of the Student:** Priyanka Biswas
2. **Name of the Constituent Institution:** Bhabha Atomic Research Centre, Mumbai
3. **Enrolment No. :** PHYS01201404010
4. **Title of the Thesis:** Nano-structured micro-granules: Synthesis and Characterization
5. **Board of Studies:** Physical Sciences

SYNOPSIS

The mesoscopic length scale (1-100 nm) in condensed matter is of immense scientific interest because materials at this length scale exhibit certain distinctive properties that are absent in the atomic (~ 1Å) or macroscopic (≥ 1μm) scales. Over the last few decades, this has been an active area in research as far as the development of novel materials and associated technologies are concerned. Further, considerable efforts have been made to synthesize hierarchical structures starting from nanoparticles through a bottom-up approach. Micrometer sized nano-structured granules are one such multi-functional structures that can be designed from basic nanometric entities.[1-3] These granules retain the inherent properties of nanoparticles, such as high surface to volume ratio, functionality, etc., but being larger in size than nanoparticles, they are less susceptible to drift currents and thermal fluctuations. Hence they provide more flexibility for application-oriented morphological tuning. From the industrial point of view, granulation of nanoparticles reduces the probability to be inhaled, which is a serious cause of nanotoxicity in factories. Apart from technological demand, scientifically too, such granules are a subject of rigorous research in recent years. Latest advancements in this field include tailor-made nano-structured granules for specific applications like sorption,[4] filtration,[5-6] etc.

This thesis illustrates the synthesis and characterization of micrometric granules composed of correlated nanoparticles. These granules were realized through spray-drying,[7] which is a well-established industrial process used to generate powder granules from atomized liquid droplets. It is used extensively in food industries for the production of milk powder, spices and other food items.[8] In recent years, this technique has been implemented in the laboratory, and over time it has proven to be indispensable for the production of nano-structured micro-granules starting from colloidal dispersion.[9-10] The dynamical transformation of the colloidal to the granular phase involves significant physicochemical modifications. During the stay of the droplets in a drying chamber, the solvent evaporates rapidly initiating self-assembly among the colloidal particles. Attractive capillary forces emerge among the nanoparticles due to the continually thinning bridges of solvent between them. Such assembly is termed as Evaporation Induced Self-Assembly (EISA).[1-2]

The assembly process, and subsequently the morphology of the formed granules are governed by several physicochemical factors. Inherent properties of the dispersion, such as colloidal particle size,[11] surface charge,[12] viscosity,[12] etc. are crucial in determining the stability of the colloid. Extrinsic factors, such as drying rate, droplet size,[9] etc. explicitly control the shape and size of the assembled granules. Due to the dependence of the morphology on a number of competitive factors, tailoring of the structure to achieve a desired utility becomes challenging. This thesis investigates the various aspects of drying of spray colloidal droplets leading to the formation of nano-structured micro-granules with tunable morphological attributes. The role of colloidal interaction in realizing porous and surface-modulated granules has also been investigated.

These granules have a multi-level structure spanning from nanometer to micrometer length scales. Hence their characterizations indeed require a combination of complementary techniques. In the present case, small-angle scattering (SAS) and electron microscopy were used extensively along with other characterization techniques.

The characteristic structural features of the granules enable investigation of several utility-based applications. Owing to their inherent pore structure, the granules can function as sorbents for various contaminants. In this regard, sorption studies of water-soluble dyes by these granules have also been carried out.

A brief description of each of the six chapters of the thesis is provided below.

Chapter 1 provides an introductory idea and background of the work, emphasizing the primary motivation of the thesis. A historical account of the advent of nanoscience and the nanometric length scale is briefly described. The widespread usefulness and uniqueness of nanoparticles, owing to their basic properties, are discussed. Self-assembly is one of the crucial properties of nanoparticles which make synthesis of higher-order structures possible through a bottom-up approach. An overview of self-assembly has been presented in this chapter. The general formalism and distinctive features of self-assembly are discussed with special emphasis on evaporative assembly in colloidal systems.

Solvent drying of a colloidal dispersion is an efficient approach by which self-assembly can be induced among the particles owing to the initiation of attractive interactions. In this regard, an account of the evaporation induced assembly process in realizing nano-structured micro-granules is presented.

The layout of the whole thesis is given at the end of this chapter.

Chapter 2 describes the synthesis technique of spray drying and the basic experimental tools used for characterizing the granules. A short historical background of the spray-drying process and its gradual development over the years is provided at the starting of this chapter, followed by a detailed step-by-step demonstration of the process. The spray-drying process consists of three primary steps[7]: (i) atomization of colloidal dispersion into tiny droplets (~10 μm), (ii) rapid, contact-free drying of these droplets forming the granules and lastly (iii) the separation of the granules from the air stream using cyclone separator.

Atomization generates tiny droplets from the colloidal dispersion feed, allowing rapid solvent evaporation due to an increase in exposed surface area. The working principle of a compressed-air nozzle type atomizer,[13] as used in the present case, is discussed. The atomized droplets are exposed to a preset inlet temperature in the drying chamber of the spray dryer. This ensures contact-free drying of the droplets, inducing self-assembly among the colloidal particles. Finally, the separation and collection of the formed granules are achieved at the cyclone separator which utilizes the principle of centrifugal separation of the heavier granules and the outflow of the moisture-laden air. In parallel with the instrumental description, the physical metamorphosis of a droplet to a granule, starting from atomization to the completion of drying has also been explained chronologically.

The second section of this chapter elaborates the two basic complementary characterization tools that were used to probe structural aspects of the synthesized granules, namely, Scanning Electron Microscopy (SEM) and Small-angle Scattering (SAS). SEM is a direct method that provides an image, evidencing the overall morphology of the granules. The working principle and instrument components of SEM with special mention of FESEM (Field-Emission Scanning Electron Microscope) are discussed. Complementary to SEM, SAS[2,6,11-12,14-16] provides statistically-averaged information about the mesoscopic structure and correlation between the nanoparticles. The scattering intensity is obtained with the variation of wave vector transfer in the reciprocal space. Quantitative real space information is extracted by mathematical model fitting. The theoretical formulation of SAS and the method of extracting useful information from scattering profiles are discussed. For the present thesis, both X-rays (SAXS) and neutron (SANS) were used for SAS measurements.

Chapter 3 describes the effect of spray-drying temperature on the granular morphology. It is demonstrated that the granular morphology gradually changed from sphere to toroid with increasing drying temperature.[17,18] A significant alteration of the granule size-distribution was observed. An account of the morphological change has been established on the basis of temperature-induced nanoparticle motion in the drying droplet. Aqueous colloidal suspension comprised of TM-40 silica (LUDOX®) was used as the feed to the spray-dryer. Granules were synthesized at four different drying temperatures (110°C, 130°C, 160°C and 180°C) keeping all other physicochemical parameters unaltered. Granules formed at lower temperatures were spherical whereas higher drying temperatures yielded toroidal granules. Larger polydispersity was observed for granules synthesized at higher temperatures, resembling the initial droplet size distribution. On the other hand, at lower drying temperatures, granules mimic a theoretically-generated distribution corresponding to isotropic drying scenario. This distinction was explained with the help of the strength of drying and thermophoresis.[19]

In the present case, the drying rate is faster than the nanoparticle diffusion rate leading to shell formation at the air-water interface. However, the thickening of the formed shell is a gradual process which is dependent on the nanoparticle accumulation at the droplet periphery by thermophoresis. The concentration ratio of the nanoparticles at the boundary of the droplet to its core was estimated by Soret coefficient.[20] Due to the temperature gradient between the exterior and the droplet centre; particles undergo a thermophilic motion towards the air-water interface where the temperature is higher than the core. When drying temperature is relatively lower, shell thickening process is prolonged. On the other hand, at higher drying temperatures, thickening is arrested, resulting in thinner shells which are prone to buckling. The tendency of buckling after shell formation is due to the gradual build-up of Darcy pressure across the porous shell.

To summarize, at low drying temperatures, granules are spherical, having a smaller average size, less polydispersity, and thicker shells. On the other hand, at higher drying temperatures, granules are larger, more polydisperse, thin-shelled, making them more prone to buckling, thus exhibiting toroidal shapes. Characterization by SAS revealed that nanoparticles have a sticky hard sphere type[21] of correlation, with a volume fraction of ~0.7 irrespective of granular shape. The shape transformation of the granules was simulated with the help of Surface Evolver[22] for varying drying rates.

The synthesized granules exhibit potential as dye sorbents owing to the hollow core and the voids in between correlated nanoparticles.[23] The specific surface area of the granules was found to be ~90 m^2/g. The sorption characteristics for the granules were carried out for Methylene Blue (MB), a water-soluble cationic dye found in industrial effluents. The morphological dependence of dye sorption abilities for these granules was demonstrated with the help of UV-Vis spectrophotometry. Nearly 94% sorption was recorded for the hollow and toroidal granules whereas ~82% sorption was found for nearly-compacted spherical granules in 24 hours of exposure.

It was demonstrated that the sorption efficiency depends on the molecular composition and structure of the dye as well. Rhodamine-B, another cationic dye, recorded negligible sorption as compared to that for MB owing to its chemical structure. Thus, this section reports a possible application of nano-structured micro-granules as dye sorbents.

In **chapter 4**, the effect of a soft template on the drying of colloidal droplet was investigated.[24] The purpose of this work was two-fold: (i) to demonstrate the effect of surface charge and template concentration of the colloidal components on the granular morphology, and (ii) to realize porous granules by calcination of the soft template. Nano-silica was chosen as the primary colloidal component with milk as the additional soft template. Two types of silica with +ve (M/s. VISA corporation, Mumbai) and –ve ζ–potential (Ludox® HS-40) were considered along with three concentration values of milk (–ve ζ–potential). The choice of milk as the soft template was made keeping in mind that milk in its natural form contains several soft components.[25-26] Shear during the atomization process partially breaks the large-sized globules and agglomerates into smaller forms. Moreover, re-agglomeration of a fraction of these broken units during EISA can lead to larger agglomerates as well. It is demonstrated that depending on the initial milk concentration in the droplet, both meso (2-50 nm) and macro (>50 nm) pores could be templated simultaneously. The effect of surface charge of silica was studied keeping the concentration ratio of silica and milk fixed. The effect of concentration was studied for the –ve ζ of silica and milk. Five bi-colloidal solutions namely, HS-40 silica (2wt %) with 1/2 /3 wt% of milk, +ve and –ve VISA silica (2wt %) with 2 wt% milk each were prepared for the purpose.

Granules comprised of HS-40 silica and milk were primarily doughnut-shaped whereas those formed from +ve silica and milk were spherical. In the first case, assembly in a droplet occurs between individual units of the components owing to their similar polarities. At the chosen drying temperature, shell formation occurs which subsequently lead to buckling to form doughnut-shaped granules. For the second case of opposite polarity of silica and milk, the components flocculate in the liquid phase itself and hinder the shell formation. Thus, the granules obtained in this case remain spherical.

In order to generate pores, the granules were calcined in air at 450^{o}C for 7 hours. The milk moieties were removed and a porous silica skeleton remained. SAS indicated a clear difference of the intensity profiles, before and after calcination. Pore structure was characterized using BET (Brunauer–Emmett–Teller) technique of gas adsorption and SAS. The specific surface area was found to be as high as 137m^2/g as compared to 90m^2/g for purely silica granules. It was observed that higher concentration of milk yielded a fewer number of large-sized pores and vice-versa. Hence, this chapter demonstrates that micro-granules with tunable hierarchical pore structures can be realized by spray drying of a colloidal solution with soft template, followed by calcination of the template.

Chapter 5 illustrates the effect of anisotropic colloidal interactions on the surface topology of the spray-dried granules. In a one-component stable colloidal system with spherical particles, the interparticle interactions are isotropic. As a result, the formed granules have a smooth surface. Addition of a second component, which is anisotropic with respect to charge and shape, alters the isotropic nature of the interparticle interactions in the system and plays a crucial role in EISA as well. It is demonstrated that such granules have unique wrinkle-like modulations on their surface. These modulations can be tuned by controlling the concentration and surface charge of the components.

A mixture of negatively charged dispersible carbon nanotube (CNT) and spherical nano-silica (NS) was used as the spray-drying suspension. Three aqueous colloidal dispersions, comprising of (i) –ve NS (2wt %) with CNT (0.1wt %), (ii) –ve NS (2wt %) with CNT (0.05wt %), and (iii) +ve NS (2wt %) with CNT (0.05wt %) were spray-dried under identical experimental conditions. Granules obtained from cases (i) and (ii) showed prominent surface modulations, whereas those from (iii) had a smooth surface. The reason for this alteration is described on the basis of the assembly mechanism in each case.

For similar polarity of the components ((i) and (ii)), sequential assembly commences according to the ascension of barrier heights of the interaction potentials. In this case, CNT bundles are formed at the air-water interface. Significant alteration in the Raman active radial breathing mode (RBM) of CNT denotes that CNTs experience unequal constriction due to irregular bundling. Assembly of NS on these irregular bundles render wrinkled surface topology of the granules. These irregular domains enclose gaps and channels in between. Thus the specific surface areas of these granules are considerably high (~130m^2/g). Investigation of sorption efficiency of Methylene Blue (MB) dye for the granules revealed 99% sorption in 2 hours, which is significantly higher as compared to that for pure silica granules (82% in 2 hours). On the other hand, in case of opposite polarity of NS and CNT (iii), the attractive interaction dominates leading to the coating of NS (+ve) on the CNTs (-ve). Spray-drying induces assembly between these NS-coated CNTs and the excess NS in the system. This reduces the probability of CNT bundle formation and hence the granules possess relatively smooth surface. However, specific surface area and the dye sorption capability deteriorate drastically (8% in 2 hours) in this case due to the absence of inter bundle channels/gaps.

Chapter 6 is the concluding chapter of the thesis. The whole work is summarized and a future outlook is given. Through this work, the versatility of the one-step process of spray drying technique in realizing micrometric nano-structured granules has been established. Further, the role of various physicochemical parameters in tuning the assembly, and consequently the morphology and the internal structure of the granules was illustrated. The experience gathered during the work opens up new scope in the synthesis of novel hierarchical nano-structured materials using spray drying and their characterization using complementary tools. This arena attracts a lot of scientific curiosity owing to the necessity of understanding of the dynamical phenomenon of droplet drying through various simulation techniques such as, Monte Carlo or Molecular Dynamics. Investigation of various technological applications of these granules, such as catalysis, filtration etc. utilizing their structure-function correlation remains to be investigated in future.

The bibliographic list of references is given after this chapter.

REFERENCES

1. C. J. Brinker, *et al.* , *Adv. Mater.* 1999, **11**, 579-585.
2. J. Bahadur, D. Sen, S. Mazumder, B. Paul, A. Khan and G. Ghosh, *J. Colloid Interface Sci.*, 2010, **351**, 357-364.
3. D. Grosso, F. Cagnol, G. Soler-Illia, E. L. Crepaldi, H. Amenitsch, A. Brunet-Bruneau, A. Bourgeois and C. Sanchez, *Adv. Funct. Mater.*, 2004, **14**, 309-322.
4. A. Mishra, J. S. Melo, D. Sen and S. F. D'Souza, *J. Colloid Interface Sci.*, 2014, **414**, 33-40.
5. J. S. Melo, D. Sen, S. Mazumder and S. F. D'Souza, *Soft Matter*, 2013, **9**, 805-810.
6. A. Das, D. Sen, S. Mazumder, A. K. Ghosh, C. B. Basak and K. Dasgupta, *RSC Adv.*, 2015, **5**, 85052-85060.
7. K.Masters, *Spray Drying Handbook*, 5th edition edn., Longman Scientific & Technical: Harlow, Essex, U.K., 1991.
8. A. Gharsallaoui, G. Roudaut, O. Chambin, A. Voilley and R. Saurel, *Food Res. Int.*, 2007, **40**, 1107–1121.
9. F. Iskandar, L. Gradon and K. Okuyama, *J. Colloid Interface Sci.*, 2003, **265**, 296-303.
10. E. Lintingre, F. Lequeux, L. Talini and N. Tsapis, *Soft Matter*, 2016, **12**, 7435-7444.
11. D. Sen, J. Bahadur, S. Mazumder and S. Bhattacharya, *Soft Matter*, 2012, **8**, 10036-10044.
12. D. Sen, J. Bahadur, S. Mazumder, G. Verma, P. A. Hassan, S. Bhattacharya, K. Vijai and P. Doshi, *Soft Matter*, 2012, **8**, 1955-1963.
13. R. B. Keey and Q. T. Pham, *Chem. Eng.*, 1976, **311**, 516-521.
14. A. Guinier, G.Fournet, B. C. Walker and L.K.Yudowith, *Small angle scattering of X-rays*, Wiley, New York, 1955.
15. D. Sen, J. Bahadur, S. Mazumder and S. Bhattacharya, *Soft Matter*, 2012, **8**, 10036-10044.
16. O. Glatter and O. Kratky, *Small Angle X-ray Scattering*, New York: Academic Press, New York, 1982.
17. P. Biswas, D. Sen, S. Mazumder, C. B. Basak and P. Doshi, *Langmuir*, 2016, **32**, 2464-2473.
18. P. Biswas, D. Sen, S. Mazumder and P. Doshi, *AIP Conf. Proc.*, 2017, **1832**, 140009.

19. R. Piazza and A. Parola, *J. Phys.: Condens. Matter*, 2008, **20**, 153102.
20. K. Hirota and O. Kimura, *Bull. Chem. Soc. Jpn*, 1943, **18**, 111-116.
21. R. J. Baxter, *J. Chem. Phys.*, 1968, **49**, 2770 2774.
22. C. Quilliet, C. Zoldesi, C.Riera, A.V. Blaaderen and A. Imho, *Eur. Phys. J. E*, 2008, **27**, 13-20.
23. P. Biswas, D. Sen, S. Mazumder and J. Ramkumar, *Colloids Surf. A*, 2017, **520**, 279-288.
24. P. Biswas, D. Sen, S. Mazumder, J. S. Melo, C. B. Basak and K. Dasgupta, *Colloids Surf. B*, 2017, **154**, 421–428.
25. G. Bylund, *Dairy processing handbook*, Tetra Pak Processing Systems AB, Sweden, 2003.
26. M. Glantz, A. Håkansson, H. Lindmark Månsson, M. Paulsson and L. Nilsson, *Langmuir*, 2010, **26**, 12585-12591.

LIST OF FIGURES

LIST OF TABLES

Chapter 1: Introduction to Nanoparticles, Self-assembly and Colloidal systems

1.1 A glance into the nanometric length scale

The nanometric length scale or the nanoscale refers to the unit of length measurement for structures having dimensions of the order of 10^{-9} m or 1 nanometer (nm).[1] Nanoscale has amassed enough attention of the scientific community over the last few decades owing to the exhibition of certain unique characteristics which are absent in any other length scales. Study of nanometric sized particles (or nanoparticles) and development of novel materials based on their unique properties forms the foundation of the well-known branches of science called nanoscience and nanotechnology. Technically, nanoscale falls on the lower bound of the mesoscopic length scale which lies intermediate to atomic scale (microscopic ~ 10^{-10} m) and that of bulk materials (macroscopic ~ $\geq 10^{-6}$ m and above).[2] Fig. 1.1 depicts the nanoscale in comparison to atomic and macroscopic length scales. Particles in this length scale consist of typically 10-10,000 atoms[3] and their uniqueness lies in the fact that their properties are also intermediate between atoms or molecules and bulk materials. For example, extensive study on gold (Au) nanoparticles reveal that two gold atoms[4] have the same property, as it is for Au in bulk, whereas, two Au nanoparticles can have different properties based on their size and shape. Characteristic features like melting temperature, colour, electrical conductivity, etc. vary with shape and size of nanoparticles. Contrary to the inertness of bulk, Au nanoparticles are highly reactive and show catalytic activity for surface oxidation[5] and epoxidation.[6] Also, metal to semiconductor transition is observed for these particles as their size decreases.[7] Thus, the variation of sizes can bring about interesting deviation from bulk properties of nanoparticles, which has invoked vast scientific curiosity over the past few decades.

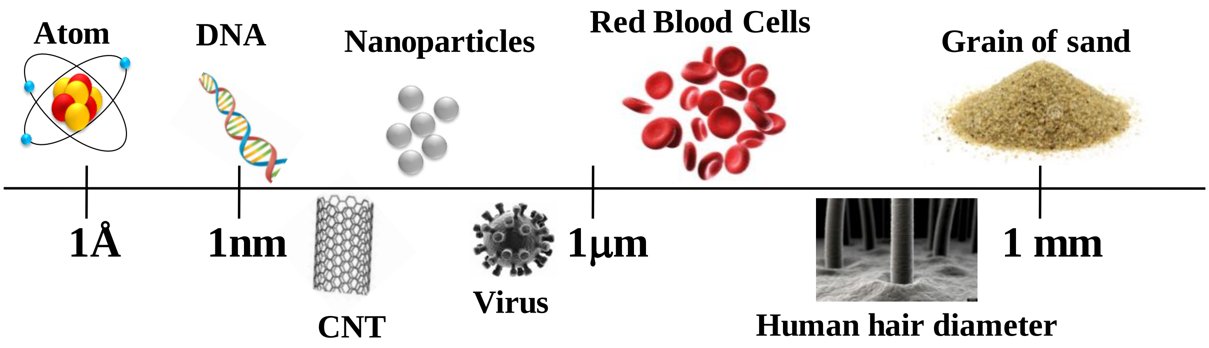

Fig. 1.1 The position of nanoscale with respect to atomic and macroscopic length scales.

The first observations and structural measurements of nanometric sized colloidal particles had been made during the first decade of the 20th century by Richard Adolf Zsigmondy, winner of the 1925 Nobel Prize in Chemistry.[8] He made a detailed study of gold sols[9] with sizes ~ 10 nm using an ultra-microscope[10] which was capable of visualizing particles using the principle of light scattering. Zsigmondy was also the first to use the term "nanometer" explicitly for characterizing particle size. Nanoscience and technology gained importance much later in the late 1900s when the invention of scanning tunnelling microscope in 1981[11] followed by the discovery of fullerenes in 1985[12] kick-started the interest in this field. Further, in 1986, publication of the book “Engines of Creation: The Coming Era of Nanotechnology” by K. Eric Drexler popularized the spectrum of opportunities that research in the field of nanotechnology can provide,[13] followed by the start of application-based research towards the early 2000s. Now nanotechnology has truly emerged as a multidisciplinary wing of research.

The conceptual origin of nanotechnology is credited to Richard Feynman, Norio Taniguchi and K. Eric Drexler. Nobel Prize winner Feynman,[14] delivered the famous lecture at Caltech (1959) titled, "There's Plenty of Room at the Bottom”, which is considered to have initiated the curiosity in this length scale.[15] He stated, "*The principles of physics, as far as I can see, do not speak against the possibility of manoeuvring things atom by atom*" Thus, in principle, it should be possible to manipulate *atom by atom* to make nanoscale machines that can perform specified functions. Japanese scientist, Taniguchi (1974) is credited to coin the term "*nanotechnology*".[16] Later, an American engineer, Drexler (1980), explored such deterministic handling of *atom by atom* in depth.[17] Over the years various prestigious awards and accolades have been presented for groundbreaking work and advancements in the field of nanotechnology[18-20] owing to significant experimental advances in the field of designing novel material utilizing nanoscale properties in various aspects of colloidal science, surface chemistry, material science, energy, communications, medicines, etc.

The first step in understanding nanoparticles is to comprehend certain phenomena unique to this length scale which have interesting implications in altering their physical, chemical, optical, electrical, magnetic, etc. property as opposed to bulk material.

I. **Quantum Confinement:** This property is responsible for the deviation of electronic, optical and magnetic properties at the nanometric scale from bulk materials.[21-25] Specifically, the phenomenon results from electrons and holes being *confined* into a dimension that approaches exciton Bohr radius.[21-25] In other words, the spatial spread of the electronic wave function is of the order of the nanoparticle size. Therefore, the electrons *feel confined* to the geometric boundaries of the nanoparticle. With the change of particle size, these electrons adjust their energies and give rise to interesting changes in the band gap and optical behaviour. This phenomenon is called the quantum-size effect. Another consequence of the confinement effect is that the energy bands become discrete (like atomic energy levels), in contrast to the presence of conduction and valence bands in bulk materials. In the bulk matter, the bands are formed by merging of a bunch of adjacent energy levels of a large number of atoms and molecules. As the particle size reaches the nanoscale, where every particle is made up only a small number of atoms or molecules, the number of overlapping of orbitals or energy level decreases and the width of the bands get narrower. This cause an increase in energy gap between the valence band and the conduction band for nanoparticles when compared to the corresponding bulk matter. Consequently, there is a blue shift of the luminescence and absorbance energy gap.[26-27] (Fig. 1.2(a)).

II. **Surface Atom Effect:** The dimension of nanoparticles is so close to that of the atoms that a large fraction of atoms lie at the surface. For example for a spherical nanoparticle of radius 1 nm (assuming atoms to be of dimension ~ 0.1 nm), ~90% of the atoms are at the surface, whereas for a particle of 10 nm radius, that fraction is merely ~10%.[28] Thus, at the nanometric length scale, the surface to volume ratio (which depends inversely on the particle radius) is higher than that in micrometric scales (Fig. 1.2(b)). Hence for a particle of radius 10 nm, the specific surface ratio is 10^3 orders larger than that for a particle of 10 μm. Atoms at the surface are more active because they are loosely bound than bulk atoms. They have more uncompleted bond sites and dangling bonds. Thus, this '*imperfect'* surface of nanoparticles provide more active sites and additional electronic states, hence are more reactive. Surface catalytic properties for metals and oxide nanoparticles are as a result of the surface atom effect.[29] The high surface energy of the nanoparticles also leads to easier surface functionalization.

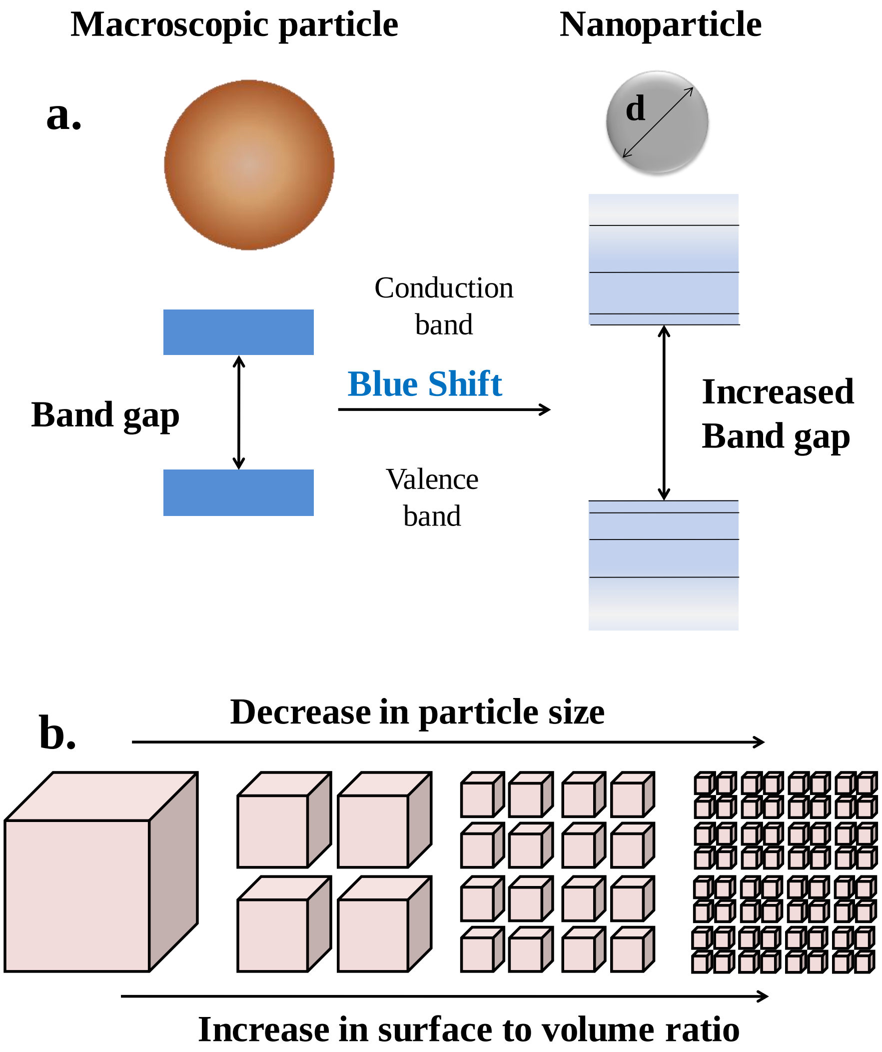

Fig. 1.2 Schematic representation of (a) increase in band gap with decrease in particle size, and (b) increase of surface to volume ratio with decreasing particle size.

III. **Self-assembly**: Self-assembly is a phenomenon where the components of a system assemble themselves to form a larger functional unit. In the nanometric length scale, for example in colloidal systems, self-assembly can be directional or random, governed by various thermodynamical factors.[3] It should be mentioned here that assembly in this length scale can be spontaneous or can also be sensitive to external stimuli such as electric and magnetic fields, gravity, flow, temperature variation, etc. The spatial arrangements of the self-assembled structures can be potentially used to build increasingly complex structures leading to a wide variety of materials that can be used for different purposes. A generalised approach to self-assembly is elaborated in the next section.

1.2 Overview of Self-Assembly

Self-assembly is a process in which, components (either separate or linked) spontaneously form ordered structures.[30] Initially, the focus on self-assembly, as a strategy for synthesis has been confined largely to molecules. Later, with the intertwining of chemistry with biology and materials science, self-assembly started to be conceptualized for nanometric and micrometric length scales as well. Basically, self-assembly is known to be important in three length scales, namely: molecular, nanoscale (colloids, nanowires, nanospheres, etc.), and macroscopic (objects with dimensions from microns to meters) A similar set of rules govern the self-assembly process in each of these ranges. Interest in the extension of self-assembly beyond molecular lengths scale have evolved due to extensive research in designing novel materials with potential for application in microelectronics,[31-32] photonics,[33-34] near-field optics,[35] and of course nanoscience.[36-38]

On the basis of sustenance by energy involvement, self-assembly can be classified into two main categories, namely, spontaneous and directed. Assembly of molecules into clusters or random assembly of nanoparticles into large colloidal aggregates that occur spontaneously falls in the category of spontaneous self-assembly. Once assembled, no external agent required to sustain the self-assembled entity. Directed assembly requires energy and usually driven by external field (electric, magnetic, heat, etc.) and the final product is long-lived even though it may not be the most thermodynamically favoured one.[39] Details of directed self-assembly are presented in section 1.2.3

1.2.1 Distinctive features

The assembly from individual components to well-defined structures is a result of interaction between the building blocks. This approach is commonly known as “bottom-up” since the building blocks assemble to a complex structure (schematically shown in Fig. 1.3). The assembled entity has a higher order than the isolated components. In mesoscopic systems, such as colloids, the interactions which drive assembly are basically non-covalent weak interactions (e.g. van der Waal’s, capillary forces, hydrogen bond, electrostatic forces, etc.).[39] Quantitatively it is almost 1/10th of the strength of chemical bonds. Thus, self-assembly in such a length scale can be comprehended by studying the underlying interaction forces. Further, fine-tuning these forces alter the assembly process and consequently lead to structures of desired characteristics. For example, virus capsids can be used to limit the size of the crystals growing inside them,[40] and colloidal crystals of desired features can be generated by allowing the particles to deposit on a patterned substrate.[41]

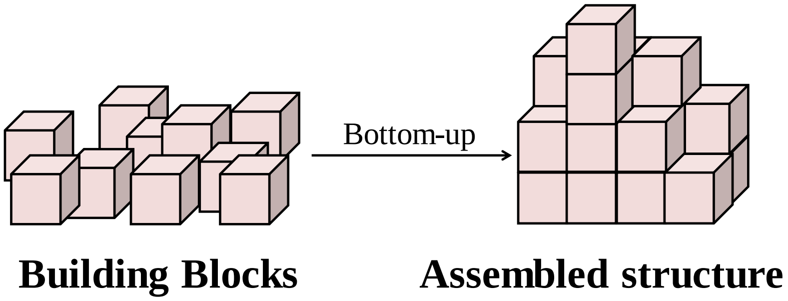

Fig. 1.3 Schematic representation of bottom-up approach of synthesizing materials.

1.2.2 General Formalism

In the previous section, it was mentioned various interaction forces play crucial role in controlling the assembly process. The general scheme of all self-assembly process is similar (although not identical) in the length scale varying from atomic to colloidal. It should also be mentioned here that self-assembly is also not always a single process; it can occur in double-, triple-, or multi-steps. For example, the formation of micelle from surfactant units is a single-step process.[42] Whereas, similar surfactant units, under the influence of some alteration in solution condition (such as, increase in local surfactant concentration, pH change, increased concentration of counter-ion) form primary micelles which again starts to interact and self-assembly commences under the influence of inter-micellar interaction forces. Hence the surfactant molecules are the primary building units; whereas micelle is the primary self-aggregate, further inter-micellar assembly forms secondary self-aggregate. Amphiphilic polymers such as block co-polymers follow a similar scheme of self-assembly and form polymer mesophases.[43]

Thus, the general scheme of any self-assembly, be it single-step or hierarchical, is essentially governed by the interaction forces between the units. The common forces which exist in systems prone to self-assembly are attractive van der Waal forces, electrostatic double-layer repulsion, hydration repulsion, depletion forces, hydrophobicity, etc.[3, 39] When the major opposing forces are comparable in magnitude and competitive with the variation of distance between the particles, such a system is said to be kinetically stable. The energy barrier height prevents the particles to assemble. In general, the total potential U_{tot} as a function of inter-particle distance (d) can be written as the net sum of the total attractive U_{att} and repulsion potentials U_{rep}

$$U_{tot}\left(d\right)=\sum_{i} f_i\left|U^{i}_{att}\left(d\right)+U^{i}_{rep}\left(d\right)\right| \qquad (1.1)$$

where i=1 represent primary aggregate, i=2 secondary aggregate and so on. f_i is the fractional contribution of the i-kind of assembly to the total potential, hence $\sum_{i} f = 1$.

Three special cases can be mentioned in this regard:[3]

(i) When $U_{total}(d) \sim 0$, the assembly is thermodynamically driven. The building units of each assembly steps are at equilibrium with the formed self-aggregates. The aggregates have finite sizes and well-defined shapes. Examples in this category include surfactant or polymer micelles, vesicles, proteins and microemulsions.

(ii) When $U_{total}(d) < 0$, self-assembly is kinetically driven and it usually continues till the most of the building units are exhausted. Indefinite and irregularly shaped aggregates which are formed in this case. For example, coagulated colloids, bilayers, gels, liquid crystals, macroemulsions.

(iii) When $U_{total}(d) > 0$, no self-assembly occurs.

So far, no external forces have been considered and the self-assembly has been spontaneous. However under the influence of an external field, as in the case of directed assembly, the equation has to be modified by an additional term, U_{ext} so the expression becomes

$$U_{tot}\left(d\right) = \sum_i f_i \left|U^i_{att}\left(d\right) + U^i_{rep}\left(d\right)\right| + U_{ext} \tag{1.2}$$

U_{ext} may or may not be a function of interparticle distance, depending on the nature of the applied field. The following sub-section discusses directed assembly in detail.

1.2.3 Directed self-assembly

Assembly that is induced externally on a system, which does not intrinsically assemble is known as directed self-assembly. Here, the chemical properties of a spontaneously self-assembled system, as described above are mimicked, but under the influence of various external factors, such as electric/magnetic fields, gravity, viscosity force flows, temperature gradient, etc. These forces are often dominant over the interparticle interactive forces.

External fields (magnetic and electric) are the most common directors of self-assembly.[44] The polarizability of the nanoparticles due to their functional groups causes them to be susceptible to the force fields.[45] As a result of which, the particles assemble overcoming their interparticle interactive forces. Another important route by which assembly can be induced is by viscous flow fields. These fields direct self-assembly of particles in solution into ordered crystals. However, often such kind of assembly is not permanent, rather the assembled particles tend to disassemble when the flow is stopped or removed, as is also the case for electric and magnetic fields.[44-45]

Evaporative assembly

Like the phenomenon of assembly through electric/magnetic field, assembly, as induced by evaporation of the solvent is also common. This type of assembly is also known as the Evaporation-Induced Self-Assembly (EISA) and is generally related to assembly in colloidal systems.[46-56] The disappearance of solvent from the dispersion leads to the ordering of the solute particles, due to various reasons such as capillarity, surface-pinning effect, etc. A schematic of general EISA is shown in Fig. 1.4. The dispersion is first cast on a substrate or sprayed and evaporation of the solvent takes place at the interface between air and the film. Coffee stains, as commonly observed in case of evaporation of leftover coffee drop are an example of EISA.[57] Drying of colloids, either contact-free or on a surface reveal characteristic patterning and packing of the nanoparticles. Initial research in this kind of assembly is credited to Lu *et al.* [58-59] Later, EISA was used in the laboratory to design meso-structured silica thin films.[60-61] In recent years, a number of meso-structured materials have been prepared by EISA, including porous material,[62-63] nano-structured granule,[64-66] etc. as a result of either Marangoni or coffee-ring effect etc.[67] EISA has proven to be a more effective method for colloidal self-assembly than force fields because here the assembly is optimized, permanent and allows efficient tailoring, and up-scalability. Investigations of EISA in contact-free colloidal droplets form the backbone of this thesis and will be discussed in details further. For this purpose, a concise comprehension of colloidal systems is given in the following section.

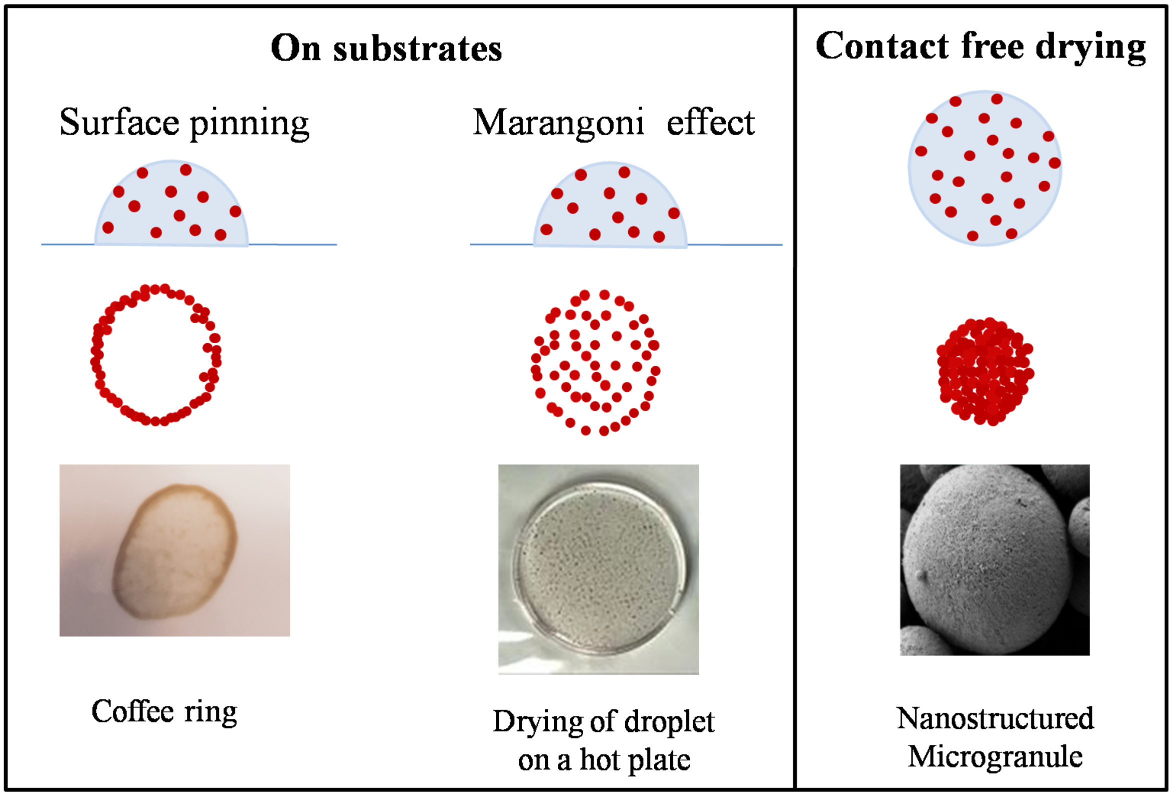

Fig. 1.4 Different outcomes of evaporative assembly.

1.3 Colloidal systems

We encounter colloidal systems in everyday items such as food, paint, inks, coatings, aerosol, etc. In the laboratory, they serve as important models for many biological systems and for the study of fundamental problems in condensed matter science, such as crystallization, gelation, glass transitions, etc. Colloids are defined as a mixture in which dispersed phase of insoluble particles are suspended throughout another continuous phase.[68] Any combination of the states of matter satisfying the above criteria qualifies as colloidal dispersion except gaseous and gaseous (because of their miscible nature). The phase behaviour of colloidal dispersions is of considerable industrial importance but it is also of great fundamental interest. The size of colloidal particles varies from 1 nm to 1 µm.[69] Colloidal particles interact with each other over distances significantly less than the size of the particles. Colloids are prone to assemble both in solutions as well as at interfaces depending on the external conditions.[70] As a result, there is a force balance being maintained in a stable colloidal system, whereas under some external perturbation, the balance is disturbed leading to coagulation. One of the critical issues of nanotechnology is controlling the thermodynamically driven self-assembly of the colloidal particles.

1.3.1 Stability

The study of colloidal stability is based on the DLVO theory, by the names of Derjaguin, Landau, Verwey and Overbeek.[71-72] The theory describes the force between charged surfaces interacting through a liquid medium: it combines the effects of the electrostatic repulsion due to electrical double-layers and the van der Waals attraction.[73] There are various interactions as well, which are of non-DLVO origins, such as steric, hydration, depletion forces, etc.[39] However, the DLVO theory provides a smoother mathematical approach to examine the dependence of colloid stability on the various parameters that determine the interaction energies between particles.

The van der Waals' force[74] can be visualised as a resulting interaction between two dipoles giving rise to an instantaneous attractive force between two atoms. It should be noted that the time average of its dipole moment is zero, but at any instant, there exists a finite dipole moment given by the instantaneous positions of the electrons about the nuclear protons. This instantaneous dipole generates an electric field that polarizes any nearby neutral atom, inducing a dipole moment in it. For identical spheres of radius 'R', Hamaker constant[75] 'A_H' (typical value of Hamaker constant for constant for condensed phases, whether solid or liquid is of the order of ~ 10^{-20} J) and situated at 'd' separation, the interaction potential (W_{VW}) is given by,[39]

$$W_{VW} = -\frac{A_H R}{12d} \tag{1.3}$$

Electrostatic double-layer repulsion develops near charged surfaces in aqueous solutions. It is called so because the charged surface (charges may originate from tightly adsorbed ions, dissociated surface groups, or substituted ions) forms the first layer. The second layer is a diffuse layer, which neutralizes the surface charge (co-ions) by oppositely charged region of counter-ions. The double-layer repulsion interaction (W_{DL}) between two similarly charges spheres of radius R is given by,[39, 76]

$$W_{DL} = \frac{R}{2} e^{-\kappa d} \Psi \tag{1.4}$$

where the force is given by $\pi R W_{DL}$, the interaction constant is, $\Psi = 64\pi\varepsilon_0\varepsilon\left(\frac{k_B T}{e}\right)^2 \tanh^2 \frac{e\zeta}{4k_B T}$

where ε_0 is the permittivity of free space ($8.85 \times 10^{-12}\ \mathrm{C^2N^{-1}m^{-2}}$), ε is the dielectric constant of the solvent at room temperature T=298 K, k_B is the Boltzmann constant ($1.38 \times 10^{-23}\ \mathrm{JK^{-1}}$). Electronic charge '$e$' ($1.6 \times 10^{-19}$ C), ζ is the electric double-layer potential or ζ-potential. The double-layer interaction is irrespective of particle geometries and always decays exponentially with distance with a characteristic decay length equal to the Debye length (κ^{-1}). This is quite different from the van der Waals' interaction where the decay is a power law having very different exponents for different geometries. The attractive van der Waals' force will cause the colloidal particles to adhere together. If the particles repel each other strongly, the dispersion will resist coagulation and the colloidal system should be stable. The net interaction energy between two colloidal particles (W_{total}), as a function of interparticle distance (d), is the resultant of the attractive van der Waals' and repulsive electrostatic double-layer interaction energies given by,

$$W_{total}(d) = W_{VW}(d) + W_{DL}(d) \tag{1.5}$$

Schematic representation of the attractive and repulsive forces in a stable colloidal system along with the net DLVO potential interaction is given in Fig. 1.5. The interactions between two colloidal particles with electrical double-layers can be visualized as two blocks connected by a spring. At large distances of separation, the spring is stretched and applies a net force pulling the blocks together (attractive van der Waals' interactions). At close approach, the spring is compressed producing a net repulsive force pushing the blocks apart (electrostatic repulsion). At some intermediate distance, the forces will be in equilibrium. The height of the energy barrier of the interaction potential curve is governed mainly by the electrical double-layer term. Hence the concentration and valence of electrolyte in the system play a key role in determining when the system will cease to be stable. For instance, increase in the electrolyte concentration reduces the repulsive electrostatic interaction, reducing the energy barrier and facilitating effective particle flocculation. The stability threshold is determined by a condition when the particles are at a critical distance corresponding to the peak of the barrier height where the first derivative vanishes, i.e., $\frac{dW_{total}}{dd} = 0$. Beyond this point the system undergoes coagulation.

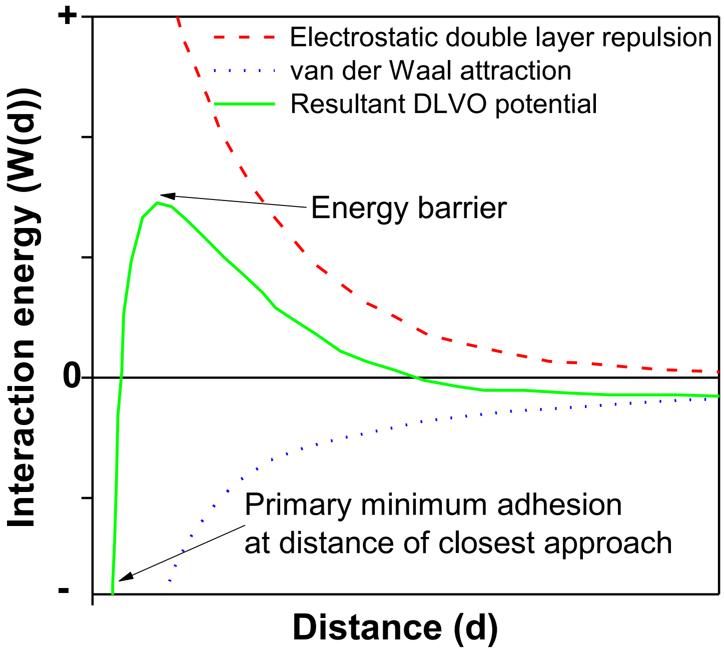

Fig. 1.5 Graphical representation of colloidal interactions as a function of interparticle distance. Range and magnitude are in relative scales.

1.3.2 Self-assembly in colloidal system

As discussed above, colloidal stability depends on the interplay between the attractive and repulsive interactions between the particles. When no external forces are involved, the colloidal self-assembly is non-directional. Colloidal particle size is in the range of nm-µm, which makes it difficult to achieve a well defined self-assembled system. Rather the product of such an uncontrolled assembly process results in the formation of large-sized agglomerates with fractal-like correlation. Fig. 1.6 compares the situations where controlled assembly leads to the formation of an ordered granular structure with uncontrolled fractal-like agglomeration. These structures are not of much importance from the technological application point of view since they are irregular in shape, unstable and cannot be functionalised. Instead, controlled growth of correlated structure would increase their usefulness. Some external agents such as the addition of foreign components to create interfaces or controlling environmental factors such as temperature or pressure, etc. helps in accelerating and defining the assembly process.[77-79]

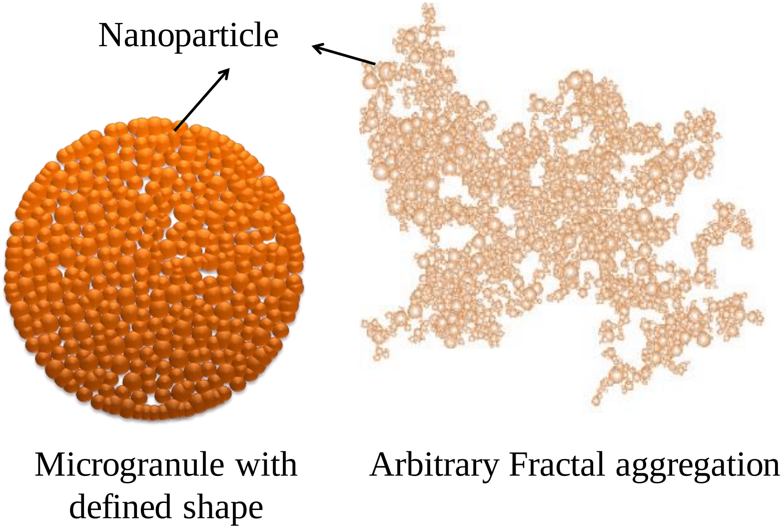

Fig. 1.6 Comparison of controlled and uncontrolled colloidal assembly.

Morphology of the self-assembled unit plays an important role in determining its utility. The size and packing fraction of the colloidal particles[80-84] determine the overall shape and size of the assembled unit as well as its ability to bind to ligand molecules.[85-86] In order to achieve an optimum efficacy, tailoring of the structure is required. EISA provides an efficient bottom-up approach in this regard for the synthesis of various materials based on applicability.[46-55, 63, 87-96]

1.3.3 Evaporation-induced self-assembly (EISA) in colloidal droplets

Owing to the increased surface area available for droplets when compared to an equivalent amount of bulk liquid, evaporation in the former will be much more rapid. Utilizing this advantage, the well-known industrial technique known as spray drying has been developed.[65, 89-90, 93, 95-106] By this method, various substances like, milk,[107] spices,[108] medicines,[109-110] etc. can be dehydrated to powder (granular) form which increases their shelf life. Details of the process will be described later in this thesis. It essentially works on the principle of rapid evaporation of solvent from contact-free colloidal droplets. Such transition from liquid to powder granule stage which is triggered by evaporation is known as evaporation induced self-assembly.

During rapid evaporation, the gradual disappearance of the continuous phase commences and a complex interplay of the forces between the colloidal particles ensues as a result of them coming in contact with the liquid-gas interface. Capillary forces dominate the interaction and the particles experience a strong cohesive force. In case of spherical colloidal particles, the capillary force between two particles is,[111]

$$F\left(d\right)=\frac{2\pi R\gamma\cos\alpha}{1+{}^{d}\!/_{2h}} \tag{1.6}$$

where 'γ' is surface tension of the liquid (water), 'd' and 'h' represents the shortest distance between the spheres of radius R and extent of wetting from the point of shortest distance, respectively. 'α' represents the contact angle. For nanometric dimension of particles in water, R is the order of 10^{-9} m and γ is ~4.8 x 10^{-2} Nm^{-1}. Hence capillary force is of the order of 10^{-11} N, which is equivalent to 10^{-20} J or ~10^{3} k_BT of energy. The solid-liquid interface is critical for determining the degree and direction of this force. The surface properties of colloidal particle play a major role during the capillary action. For example, for an aqueous colloidal dispersion, if the particles are hydrophilic, the contact angle between the water and particles is more, hence, during evaporation, the particles try to move to a region, so as to increase contact with water. On the other hand, the situation will be reversed for hydrophobic particles, i.e., the particle will move away from the water interface.

Capillary forces can be categorized as immersion, floatation and bridged types[3] as depicted in Fig. 1.7. For immersion and floatation type, the direction of the capillary force is lateral with respect to the liquid-particle contact line. For bridged type, its direction is normal to the contact line. When colloidal particles are hydrophilic, the aqueous phase can be a bridged phase. In the present case of drying of a colloidal droplet, water bridges are formed in between the particles, which results in bridge capillarity. Consequently, the particles are drawn close to each other. The diminishing thickness of the water bridge continues to bring the particles closer, resulting ultimately in their interlocking. The interlocking of particles throughout the dimension of the droplet will result in a finite-sized granule with nanometric sized micro-structure which is known as a nano-structured micro-granule.[64-66]

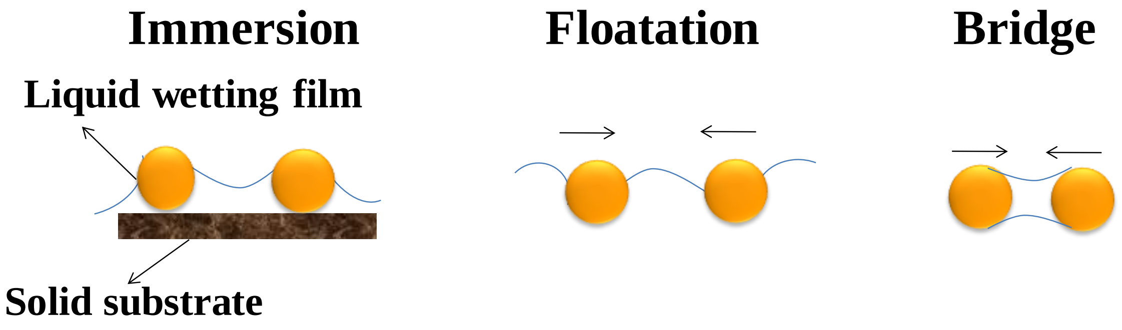

Fig. 1.7 Schematic representation of the types of capillary interactions.

1.3.4 Nano-structured micro-granule

From the industrial point of view, designing nano-structured micro-granules from nano-suspension are advantageous over dry powders of nanoparticles because the latter is lighter and consequently are difficult to handle. Nanotoxicity is a major concern in industries in particular since workers may inhale toxic nanoparticles, which deposits in lungs causing cancer or circulate in the blood causing fatality.[112-113] For easier handling and reduction of safety concerns, a frequently adopted solution consists in granulating nanoparticles, thereby increasing its mass and size, so that they are less likely to be affected by Brownian motion and thermal fluctuations.

In industries, granulation is usually achieved by spray drying.[107-109] Although compact spheres may form during the spray-drying process, many other granule morphologies have been reported, such as doughnut-like or hollow, etc.[114-115] The granule morphology is indeed crucial for some applications. For instance, it controls the porosity of ceramics and their mechanical properties. For pharmaceutical applications, morphology requirements may differ according to the route of administration of the powder. If the powder is intended to be placed in a capsule for oral administration, spherical dense micro-granules are required[116] whereas, for inhalation, crumpled paper morphologies or hollow spheres are convenient for deeper lung deposition.[117] Optimization of the powder for its final application, therefore, requires the full determination and control of the relevant parameters that will allow one to finely tune granule morphology. Details of the spray drying technique and the dependence of the granular characteristics on the drying parameters are given in later chapters.

The synthesis, characterization and processing of nano-structured micro-granules are part of an emerging and rapidly growing field of nanotechnology. R&D in this field emphasizes scientific discoveries in the generation of materials with controlled microstructural characteristics, research on their processing into bulk materials with engineered properties and technological functions, and introduction of new device-concepts and manufacturing methods.

1.4 Objective of the thesis

During last several years, considerable efforts have been made to develop multilevel composite nano-structured materials using various bottom-up approaches. Techniques such as chemical vapour deposition, physical vapour deposition, inert gas condensation, precipitation techniques, etc. are commonly used for this purpose. The complexities involved in each of these methods necessitate the implementation of rapid, one-step, energy efficient and economical process for the synthesis of nano-structured micro-granules. Moreover, these granules possess a structure which spans multiple length scales, therefore complementary characterization techniques have to be employed.

Recent studies have demonstrated the use of the spray-drying technique as an easy, one-step method of realizing nano-structured micro-granules through evaporation induced self-assembly (EISA) of contact-free colloidal droplets. This technique allows sufficient flexibility and control over the process parameters which extrinsically affect the EISA. Moreover, colloidal properties also play a crucial role in EISA and governing the granular morphology.[53, 92-95] Due to the dependence on numerous interdependent parameters, methodical understanding the droplet to granule transition during EISA is a challenge. These granules are also technologically beneficial in applications such as filtration,[100] bioremediation,[118] etc. Thus, in order to harness the full potentiality of these granules, a stepwise approach is essential starting from the synthesis process. Apropos to the requirements, the main motivation of this thesis work has been listed below,

(i) Realization of nano-structured micro-granules through contact-free drying of colloidal droplets using the one-step, energy-efficient process of spray-drying.

(ii) Mesoscopic structural investigation using complementary characterization techniques of small-angle scattering and electron microscopy.

(iii) Understanding the underlying mechanism of EISA in contact-free colloidal droplets under pertinent physicochemical conditions.

(iv) To establish a fundamental structure-function correlation of the granules aimed at specific technological applications.

1.5 Layout of the thesis

The present doctoral thesis has been structured into six chapters. An overall introduction and establishment of the context of the work have been already discussed in **Chapter 1**.

Chapter 2 elaborates the experimental techniques that have been employed for synthesis and characterization of the nano-structured micro-granules. This chapter has been divided into two parts. The first part illustrates the synthesis process of spray-drying in detail. The second part of this chapter discusses the two basic characterization techniques, namely, electron microscopy and small-angle scattering (SAS) while succinctly describing the complementarities of the two.

Chapter 3 describes the role of drying temperature on the granular morphology of a one-component colloidal dispersion. It consists of two parts. The first part deals with the explanation of origin such morphological diversity and the structural characterization of the granules by techniques such as SAS, microscopy and porosity characterization by gas adsorption. The second part investigates a potential application of these porous granules as sorbents for cationic dye.

The intrinsic role played by the interparticle interactions in the colloidal dispersion has been discussed in the next two chapters. **Chapter 4** investigates the effect of addition of soft template to a colloidal suspension. A facile way to obtain granules with tuneable porosity has also been demonstrated. **Chapter 5** discusses how anisotropy in the colloidal interparticle interactions results in granules with prominent surface wrinkling.

Chapter 6 is the concluding chapter of the thesis where the results have been summarized and future outlook of the work have been suggested.

Chapter 2.1: Synthesis of Micro-granules by Spray Drying

2.1.1 Background

Spray drying is a well-established technique that has been used in industries for over a century. Earliest descriptions date from 1860 with the first patented design recorded in 1872.[118] Masters (1991)[99] defined spray drying as "*the transformation of feed from a fluid state into a dried particulate form by spraying the feed into a hot drying medium.*" Almost all other methods of drying, including ovens, freeze dryers, rotary evaporators, produce particles of irregular size and shape which require further processing (e.g. grinding and filtering).[119] Spray drying, on the other hand, offers a very flexible control over powder particle properties such as density, size, shape, dispersibility, flow characteristics, moisture content, etc.[120-122] Spray drying can be used in a wide range of applications where the production of a free-flowing powder is required. This method of swift dehydration has become most successful in pharmaceuticals, bone and tooth amalgams, beverages and flavours, colourings and plant extracts, milk and egg products, plastics, polymers and resins, soaps and detergents, textiles and many more.[107-110] It gained importance during World War II when there was a sudden surge in the requirement of dehydrated food because the transport weight of food and other materials had to be drastically reduced. However, milk drying was the first major commercial application of the technology. The fluid feeds in spray-drying can be solutions, suspensions, emulsions, slurries, pastes or melts. The drying process allows lenient adjustments to encompass a broad range of experimental conditions, including the drying of heat-sensitive materials such as vaccines and complex proteins.[121, 123] The reproducibility of spray drying enables it to be upgraded to nearly any scale of production-from a few grams of solids in laboratory spray drier, all the way up to very large instruments that can continuously produce more than 10 metric tons of powder per hour!

Over the years, spray drying has gained importance in the field of nanotechnology, particularly in nano-medicine[124] where it is used to produce a good yield of particles/granules with narrow size distribution. It is a cheaper alternative to lyophilisation or freeze drying of nanoparticle suspensions. In the last few decades, this technique has proved to be crucial in the synthesis of nano-structured materials.[48, 64-66, 125] Detailed discussions of the technique, mechanism of formation of granule and buckling of shells are given in this chapter.

2.1.2 Technique

Droplet to granule transition is explained on the basis of the competitive forces that act at various stages of drying. A constant feed rate is maintained so as to have a narrow size distribution of droplets. Atomization increases the surface area available for drying. With the gradual disappearance of water, capillary forces emerge as the water acts as a bridge between the particles, bringing them closer (Fig. 1.7). The final outcome of such a process is a granule composed of jammed nanoparticles. For an isolated single evaporative water droplet at temperature *T*, the shrinkage in the size of the droplet, due to diffusion limited evaporation is given by,[126]

$$R_d\left(0\right)^2 - R_d\left(t\right)^2 = \frac{2D_v m_v}{\rho R_{gas} T}\left(p_s - p_\infty\right)\tau_d \qquad (2.1)$$

where $R_d(0)$ is the radius at time t=0 and R_d(t) is the radius at time t, p_s and p_∞ are the saturation vapour pressure on the surface of the drop (which depends on temperature) and at large distance, respectively. τ_d is the drying time, D_v is the diffusion coefficient of vapour, m_v is its molecular mass, ρ is the mass density of solvent and R_{gas} is the universal gas constant. Here, it should be noted that drying time, in reality, will be much higher because of the presence of surrounding droplets in the drying chamber. Factors like temperature, pressure,[87] concentration,[93] presence of additive,[127] etc. affect the mechanism of granule formation. More details shall be discussed in the later chapters of this thesis.

Transition from fluid to a dry powder by atomization in a hot air stream generally consists of four fundamental steps as elaborated in this section: (i) atomization of the liquid feed, (ii) drying of spray by drying gas, (iii) formation of dry powder granules and (iv) separation and recovery of the dry product. Fig. 2.1 depicts a schematic representation of the spray drying technique. The spray dryer that was used for the synthesis of granules in the laboratory was LU 228 from Labulitma® given on the right in Fig. 2.1.

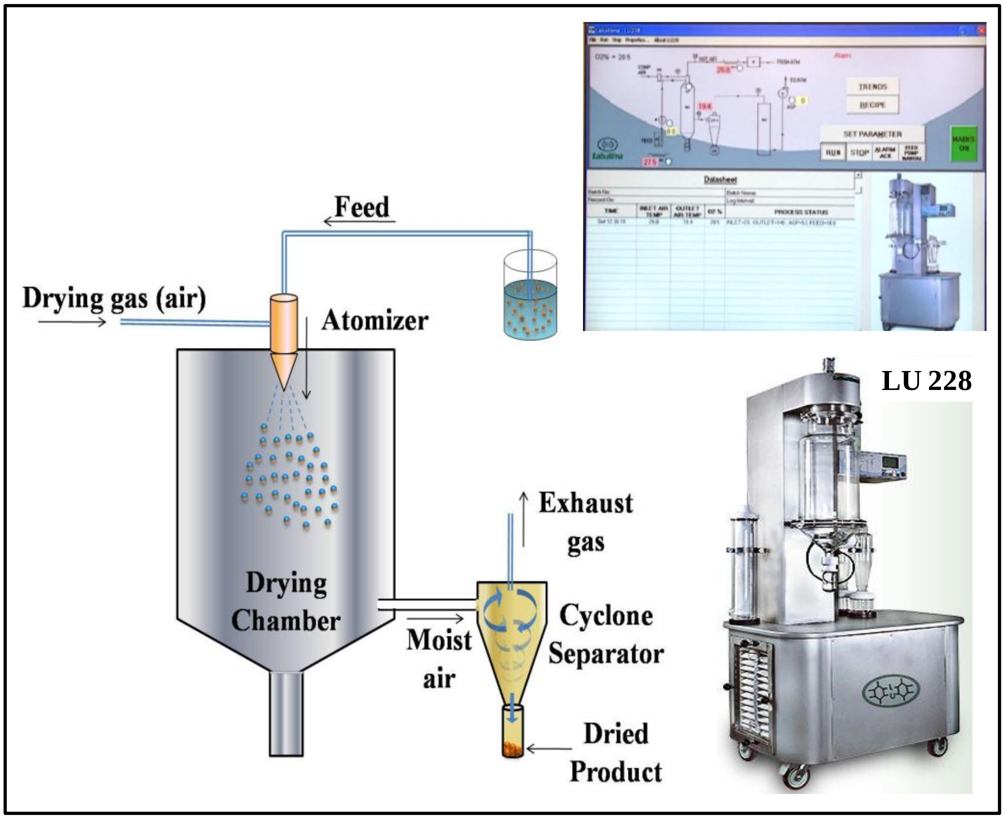

Fig. 2.1 Schematic representation of spray dryer and photograph of the laboratory spray dryer used with the instrument control software.

Laboratory spray-dryer LU 228 operates at an inlet temperature range from ambient to ~280°C with an accuracy of ± 1° C. Compressed air nozzle is used in a co-current setup. The steps involved in spray drying will be explained below, corresponding to the LU 228 instrument.

2.1.2.1 Atomization of liquid feed

This is the first and the most crucial step of the spray drying process[128] because it governs the uniformity in the droplet sizes and consequently the granule sizes. The fluid is fed into the drying chamber by a peristaltic pump through the atomizer which generates tiny droplets (micrometric size). Atomization is necessary to ensure rapid drying of the droplets. For comparison, consider 2mL volume of water, after atomization yields ~40 x 10^8 droplets of 5μm radius which corresponds to a surface area of 1.2 m^2. Thus, rapid evaporation of the solvent occurs.

The working principle of the atomizers is governed by the liquid disintegration phenomenon, first explained by Joseph Plateau in 1873.[129] In short, a liquid jet of constant radius (initially) falling vertically under gravity was considered. As the length of the liquid stream increases and reaches a critical value, the jet loses its cylindrical shape and disintegrates into a stream of droplets due to the decrease in surface tension.[130] The analytical explanation of this physical observation was given by Lord Rayleigh in 1878 by the "Liquid jet theory".[131-132] In this theory, a laminar jet was considered to be flowing out of a circular orifice (Fig. 2.2). The growth of small disturbances leads to the ultimate breakup of the stream in the critical condition when the fastest growing disturbance attains a wavelength (λ_d) of 4.51d_{cyl}, where 'd_{cyl}' is the initial jet diameter.[130] After breaking up, the liquid cylinder of length 4.51d_{cyl} disintegrates into a stream of spherical drops (diameter d_{sph}). Equating their volumes, $4.51 d_{cyl}\pi\left(\frac{d_{cyl}}{2}\right)^2=\frac{4}{3}\pi\left(\frac{d_{sph}}{2}\right)^3$ we get $d_{sph}=1.84 d_{cyl}$. Effects of surface tension and inertial forces were considered in Rayleigh's treatment, whereas the viscosity, effects of the hot and compressed gas was neglected. Weber (1931) later improved the analysis by incorporating air friction which shortens λ_d to $4.44 d_{cyl}$ at zero relative velocity.[133] When relative velocity increases to 15 ms^{-1}, $\lambda_d = 2.8 d_{cyl}$ and $d_{sph} = 1.6 d_{cyl}$. Thus, the critical wavelength for the jet breakup is reduced for an increase in relative speed, which results in smaller droplets. Ohnesorge in 1936 further included all the factors including viscosity, density, surface tension and jet size and obtained the relation defining the dimensionless Ohnesorge number (Oh) which is the ratio of Weber number (We) to Reynolds number (Re),[134]

$$Oh=\frac{\sqrt{We}}{Re}=\frac{\mu}{\sqrt{\rho\sigma L}}=\frac{viscous\ forces}{\sqrt{inertia\times surface\,tension}} \tag{2.2}$$

where μ, ρ and σ are the viscosity, density and surface tension of the feed droplet, respectively; L is volume per unit area of the feed droplet. Thus, the breaking up of the liquid into droplets occur as a result of conflicting forces supplied by the turbulence in the emerging liquid jet along with the air friction whereas viscosity and surface tension forces resist the change. Later, when the droplet is airborne, shear stresses start to realign which leads to further fission of the droplet.

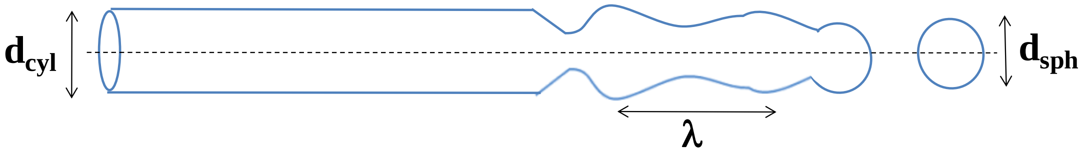

Fig. 2.2 Droplet formation from a cylindrical stream.

Although all the atomizing techniques provide an efficient atomization, the droplet size distribution varies majorly. The most commonly used atomizers are pressure nozzle, rotary,[135] two-fluid,[136] ultrasonic,[137-138] electrohydrodynamic,[139] etc. Each of these types has different principles of operation. The particular case of LU 228, which has a compressed air pressure nozzle type of atomizer, has been described here.

Pressure Nozzle Atomizer

The first known spray dryers used nozzle atomizers. As suggested by the name, the basic working principle is the discharge of liquid under pressure through an orifice.[140] The energy required to overcome the pressure drop is supplied by the feed pump which is then converted to kinetic energy as the feed emerges from the nozzle at high speed breaking up into a spray of droplets. The narrowest granule size distribution is possible with this technique. The average granule size produced, for a given feed, is a function of the feed rate, viscosity and the atomization pressure. This is, in fact, the most energy efficient of all the atomization techniques. Spraying pressure (operating range: 250–10,000 PSI) is tunable according to desired granule size and also depending on feed characteristics. Droplet sizes hold an inverse relationship with the atomization pressure value,[99], $\frac{D_2}{D_1} = \left(\frac{P_2}{P_1}\right)^{-0.3}$ where D_1 and D_2 are initial and final droplet sizes on changing the atomization pressure from P_1 to P_2. However, at high feed rates, the droplet size is less homogeneous when compared to rotary atomizers. Also, these nozzles require routine changing of the nozzle internal pieces due to plugging of the orifice, depending upon the utilization of the dryer.

2.1.2.2 Drying of spray droplets

After atomization of the feed into tiny droplets, they come in contact with the drying gas. Rapid evaporation of the solvent commences at this stage. The crucial factor here is to ensure uniform exposure of the droplets to the drying air. Efficient contact can be established by subjecting the droplets to hot air through co-current (in the same direction) or counter-current (in the opposite direction) flows.[141] Co-current type of flow, unlike counter-current is preferable for the drying of heat-sensitive materials as the final product is in contact with the coolest air. LU 228 instruments have a co-current type of gas flow. Fig. 2.3 illustrates the two types of flow.

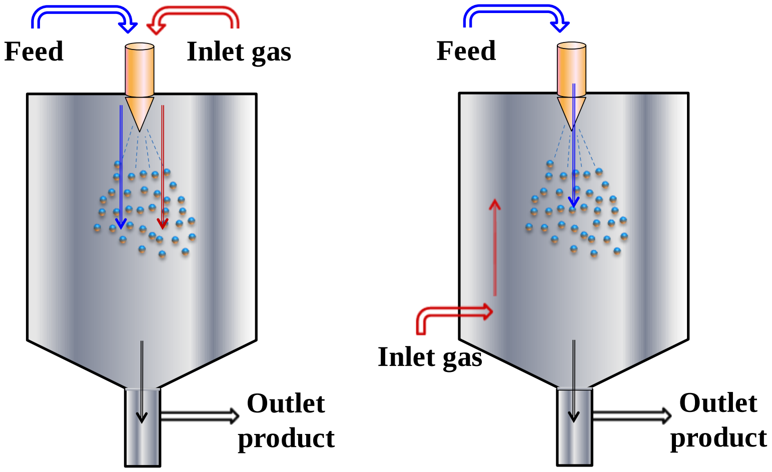

Fig. 2.3 Schematic representation of co-current (left) and counter-current (right) spray-drying configurations.

In addition, there are intermediate configurations with mixed flow between co-current and counter-currents. A uniform airflow and an appropriately designed drying chamber are required for proper functioning at this stage. Uniform air flow is obtained from an air disperser, which creates pressure drop for airflow in all directions of the spray drying chamber. The air disperser is normally placed adjacent to the atomizer.

2.1.2.3 Formation of dry granules

Formation of dried product by evaporation of moisture and the morphology definition of the final dried product takes place at this stage. The drying kinetics predicts the heat and mass transfer in the droplet during evaporation. Considering evaporation from a single droplet subjected to convective drying in a spray dryer, the whole process can be divided into two stages, namely, the constant rate period and the falling rate period. First, when droplet comes in contact with hot air, the temperature of the droplet increases from its initial temperature to the drying temperature. During this period, solvent removal occurs at a constant rate from the surface of the droplet. At this stage, the temperature is steady at wet-bulb temperature and the drying gas is saturated with vapour from the liquid.[142] Shrinkage of the droplet continues due to gradual isotropic loss of liquid. Evaporation rate is proportional to the surface area of the droplet.[143] In the second step or the falling rate period, the evaporation is no longer at a constant rate. Rather, the rate decreases due to the influence of vapour pressure which has build-up due to the other droplets in the drying chamber. The moisture content inside the chamber is high; hence the rate of evaporation is slower at this stage. Here shell or crust formation and buckling of shells are very likely. After shell formation, the evaporation of solvent takes place through the shell.[144] At this stage, the granule reaches the coolest part of the dryer, approaching the outlet temperature. The granule temperature continues to decrease and finally obtained granules are at a lower temperature than the inlet temperature.[145]

2.1.2.4 Separation and recovery

The operation configurations in spray-drying can be open-loop or closed-loop.[146] The former uses air as drying gas that is not re-circulated, while the latter utilizes an inert gas (e.g., nitrogen) that is recycled in the drying chamber throughout the entire process. The open-loop configuration is usually preferred in most of the cases since it is more cost-effective and stable. Closed-loop mode is used to prevent the mixing of explosive gases and for the manipulation of substances that are sensitive to oxygen. Thus, an efficient filtering system should be present so that the air that is expelled out (open-loop) or re-circulated (closed-loop) is free from particulate matter. To ensure this separation, a two-step system is employed to separate the final product from the drying medium. The vacuum system with a cyclone separator completes the process of powder collection.[146]

Cyclone separator

A cyclone separator is an attachment with the main components of the spray dryer that utilizes centrifugal force to separate the solid components from a carrier gas (usually air). It consists of an upper cylindrical part (barrel), and a lower conical part (cone). After exiting from the spray dryer, air loaded with solid powder granules enters tangentially at the top of the barrel and travels downward into the cone, forming an outer vortex. A centrifugal force acts on the solid components due to the increasing air velocity in the outer vortex, thereby separating them from the air stream. When the air stream reaches the bottom of the cone, an inner vortex is created, reversing its direction and exiting out at the top as clean air. The particulates fall into the collection chamber attached to the bottom of the cyclone.[147] The granular diameter cut-off (d_g) for a given cyclone configuration is, $d_g = \sqrt{\dfrac{9W\mu_a}{\pi\left(\rho_p - \rho_a\right)N_t V_i}}$ where W is the inlet width (m), μ_a is the viscosity of air (1.85 x 10^{-5} kgm^{-1}.s), ρ_p and ρ_a is the density of the granules and of air respectively (in kg/m^3), V_i is the inlet velocity (in m/s), and N_t is the number of turns, taken to be 5.[148]

An additional powder collection system, comprising dry collectors (such as a second cyclone separator, bag filter, electrostatic precipitator, etc.) are sometimes present, followed by wet scrubbers thereby increasing the efficiency of a filtering out particulate matter.[118]

2.1.3 Morphology of the granules

The properties of the finally obtained product depend on various factors such as (i) process parameters, (ii) properties of the liquid feed and (iii) equipment design. For example, a high flow rate of the liquid feed, high feed viscosity,[118] large nozzle diameter, high concentration favour the formation of larger granules. Conversely, low surface tension, high atomization pressure[99] and small nozzle diameter render smaller granules. Regarding the morphology of the granules, faster solvent evaporation rate usually leads to granules that are more deformed (buckled), due to shorter time for the droplets shrinkage. The control of size and morphology during the spray-drying process can be done smoothly. It is to be mentioned here the hydrodynamic effects on the droplet during atomization has been overlooked since the droplet size is significantly small (~10 μm). Apart from the equipment parameters, physicochemical properties of the colloidal suspensions also have been found to play a major role in the formation of a granule. An overview of the factors determining the ultimate morphology is given in this section.

2.1.3.1 Quantification of drying: Péclet number

The quantitative measure of the strength of drying is expressed by the dimensionless Péclet number P_e, that compares the drying and diffusion characteristic times. The diffusive motion of the nanoparticles tends to homogenise their distribution but the loss of fluid from the droplet alters this motion. P_e is defined as the ratio of the evaporation rate and the diffusion rate. In temporal terms, it is the ratio of mixing time, τ_{mix} (time taken by a particle to reach the centre of the drying drop from the periphery) of the nanoparticles in the droplet to its drying time τ_d given by,[149, 103, 150]

$$P_e = \frac{evaporation\,rate}{diffusion\,rate} = \frac{\tau_{mix}}{\tau_d} = \left(\frac{R_d^2}{D_{np}}\right) / \tau_d = \left(\frac{R_d^2}{\tau_d} . \frac{6\pi\eta R}{k_B T}\right) \qquad (2.3)$$

where R_d is the droplet radius and D_{np} is the diffusion coefficient of the nanoparticles in the droplet, $k_B T$ is the thermal energy, 'R' the nanoparticle radius and η the solvent viscosity. During evaporation, as the solvent continues to disappear and the nanoparticle concentration exceeds the saturation. A typical calculation of the drying time starting from the formation of the droplet to the granular stage is carried out below.

For a droplet of radius R_d having a solute concentration ϕ_d forming a granule of radius R_g, with volume fraction ϕ_g, following conservation of mass, the balance equation can be written as, $\phi_g R_g^3 = \phi_d R_d^3$. Such a relation holds true in the scenario of isotropic drying.[103] An estimate of the drying time for aqueous colloidal droplet dispersion is made from Eq. 2.1. At the time of atomization, $R_d(0)$ is given by the total droplet radius, assumed to be 10 μm. As a result of continuous shrinking, $R_d(0)$ reaches $R_d(t)$ which is typically 1/5th of $R_d(0)$, in case of isotropic drying. D_v for water vapour at 100°C (T=373K) is 3.5 x 10^{-5} m^2s^{-1}, m_v for water is 18 $g.mol^{-1}$, ρ is 1000 $kg.m^{-3}$, p_s at 100°C is 658 Torr, R_{gas} is 8.314 $J.mol^{-1}K$. p_∞ is the vapour pressure at an (ideally) infinite distance is taken to be zero. τ_d in such a case is calculated to be in the order of milliseconds (2 ms). Ideally, with the gradual build up of vapour in the drying chamber, p_∞ cannot be neglected. In such a case, τ_d can reach up to fraction of a second, depending on the aspirator rate. For the laboratory spray dryer LU 228, the drying chamber has a diameter of 20 cm and length 60 cm, typical aspiration rate of operation is 50 m^3 hr^{-1}. The aspirator rate per minute is much larger than the influx feed pump rate (typically 2-10 mL min^{-1}), hence it can be safely assumed that p_∞ is zero.

Often τ_d is quicker than the mixing time τ_{mix}, which is the case for P_e>1. In this case, the nanoparticles at the surface of the droplet do not find enough to diffuse to the centre, instead, they get jammed at the surface. Hence a thin shell or crust is formed. Further solvent removal occurs via the thin shell. Granules thus formed are hollow. On the other hand when $\tau_{mix} < \tau_d$ (P_e<1), shell formation is hindered as the drying is slower so particle movement is a diffusion-controlled process; such a scenario is known as isotropic drying.[151] This condition can also be triggered by slowing down of the evaporation rate or the drying time when there is a significant build-up of vapour in the drying chamber. Depending on the rate of evaporation, water can be trapped inside this hollow core. This causes an imbalance of osmotic pressure across the shell, which may ultimately buckle to facilitate further evaporation of the trapped water.[152] Literature shows the tuning of different parameters to control the buckling, such nanoparticle polydispersity,[92] charge,[94] concentration,[93] presence of polymers,[153] electrolyte,[102] etc. by varying experimental conditions such as atomization pressure for spray drying,[87] viscosity of the colloidal solution,[54] etc. Fig. 2.4 depicts the two scenarios schematically.

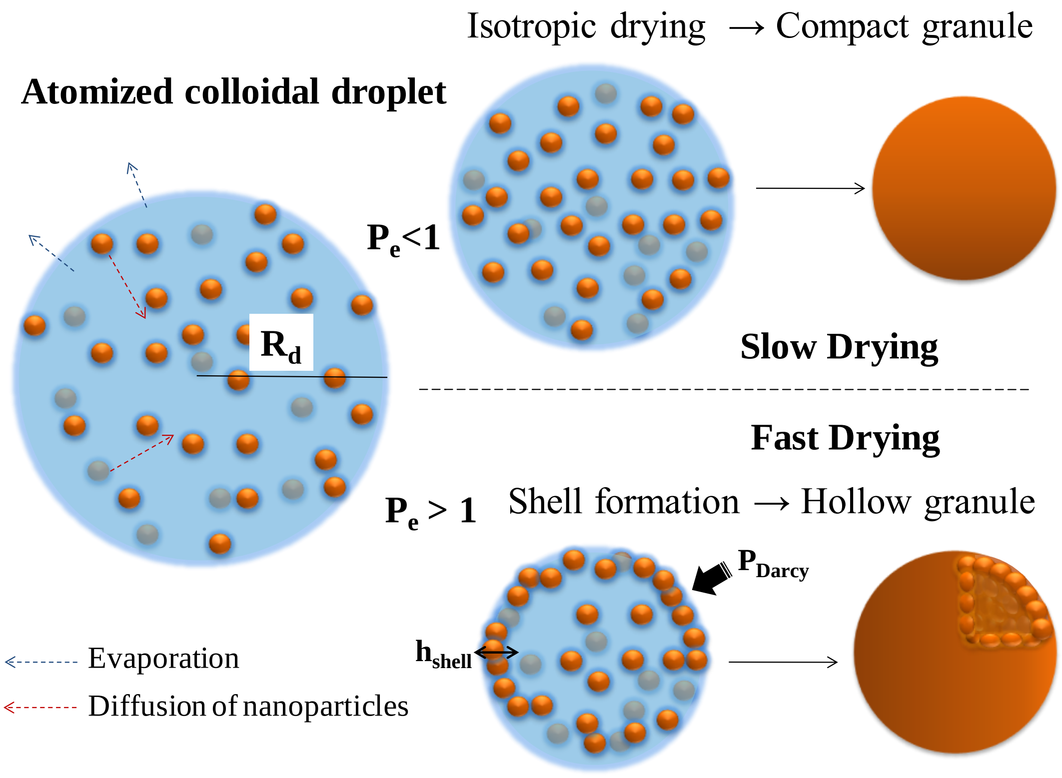

Fig. 2.4 Two types of drying scenarios.

An atomized colloidal droplet is shown to behave differently depending on the drying rate. An intermediate stage of the drying droplet is shown where in case of isotropic drying, the nanoparticles are fairly homogeneous throughout, whereas, for fast drying, a layer of nanoparticles is seen to accumulate at the boundary, which forms a thin shell. In the third stage, the cross-section of the granule is shown, the first case yields compact granule and for the second case, a hollow granule is formed. For a single isolated droplet of diameter 1 μm with 10 nm diameter particles suspended in water, and for a drying time of 1 millisecond at 100°C, P_e is close to 10. Thus, the diffusion process is slower by two orders of magnitude than the drying time and the effect of nanoparticle diffusion is therefore negligible in such cases. Precisely, the droplet size above which diffusion can be neglected is given by $(k_B T \tau_d / 6\pi\eta a)^{1/2}$ or ~ 0.1 μm which is much smaller than the droplet size in most spray driers. However, due to the presence of other droplets in the drying chamber, the rate of evaporation is slower; hence the value of P_e can fall below 1 depending on other experimental conditions. Thus, the shape of the final grain is therefore not solely determined by the Péclet number. The mechanical property of the shell formed also plays an important role in the morphology determination of the final grain. To account for those properties, it is necessary to consider the stress sustained by this shell, which is the subject of the next section.

2.1.3.2 Formation of shell and its subsequent buckling

As mentioned earlier, capillary forces arise during evaporation as the disappearing water form menisci between the nanoparticles which are responsible for cracks developed in drying droplets of suspensions of soft nanoparticles[154] and also for buckling of the shell during drying.[46, 54, 87, 95, 151, 153, 155] Needless to say that, in order to buckle, the shell must first become solid. The process for the same is being elaborated below,

I. **Formation of elastic shell:** Tsapis *et al.*[151] have shown that the liquid to solid transition of the shell results from the viscous stress induced by the permeation of solvent through the shell. This flow-induced stress results in a uniaxial compression on the accumulated nanoparticles. The flow is analogous to the one through a porous medium; it results in a pressure difference across the shell that is related to flow velocity (v) using the classical Darcy's law for porous media,[155] written as,

$$P_{Darcy} = \frac{\eta v}{K} h_{shell} \tag{2.4}$$

where η is the solvent viscosity, h_{shell} the shell thickness and K its permeability. This pressure difference is counterbalanced by the "particle pressure", or the interaction forces acting between the nanoparticles. P_{Darcy} and shell thickness h_{shell} is depicted in the fast drying scenario of the droplet in the schematic Fig. 2.4.

As mentioned earlier (Eq. 1.5), for charge stabilized nanoparticles, the Derjaguin Landau Verwey Overbeek (DLVO) potential describes the interaction in short range, which is a combination of van der Waals attractive part (W_{VW}) and the electrostatic double-layer repulsion (W_{DL}). The resulting potential exhibits (W_{total}) an energy barrier (Fig. 1.5) that can be overcome under the action of the Darcy pressure resulting from solvent's flow. In a scenario when the energy barrier is ultimately surmounted, the nanoparticles that are accumulated at the droplet's surface form a solid shell. The shell eventually buckles, as the solvent trapped inside escapes by evaporation.

The permeability (K) of the shell is related to the nanoparticle radius (R) by the Carman–Kozeny relation,[151]

$$K \cong \frac{R^2 \left(1-\phi_{np}\right)^3}{45\phi_{np}^2} \tag{2.5}$$

where ϕ_{np} is the nanoparticle packing fraction in the shell. Assuming that the relative velocity (v) between the porous shell and solvent is $v \approx R_d / \tau_d$ where R_d is the droplet radius, Eq. 2.4 becomes,

$$P_{Darcy} = \frac{45\phi_{np}^2}{\left(1-\phi_{np}\right)^3} \cdot \frac{\eta R_d h_{shell}}{R^2 \tau_d} \tag{2.6}$$

Therefore, Darcy pressure increases linearly with the shell thickness. Fig. 2.5 shows the variation of P_{Darcy} with shell thickness. As the droplet dries, the thickness h_{shell} can be assumed to vary from a nanoparticle diameter $2R$ (one-layer of nanoparticles at the shell) to the total droplet radius R_d (compact granules) Consider nanoparticles in an aqueous droplet (η =8.9x10^{-4} Pa.s) of radius (R_d = 1000R, considering random jamming packing volume fraction (0.64) at the shell, the Darcy pressure build-up as a function of normalized shell thickness is plotted in Fig. 2.5 for normalized drying times of 1, 5 and 10 units. It is shown graphically that to attain a particular reference Darcy pressure value (P_{ref} marked by the dashed line); the corresponding h_{shell} is minimum (marked by point A) for the faster τ_d (1 unit) and maximum (marked by point C) for the slowest normalized τ_d (10 units). Thus, granules with thinner shells are formed at faster drying rates when compared to that formed at slower rates. Consequently, the former is more prone to buckling than the latter.

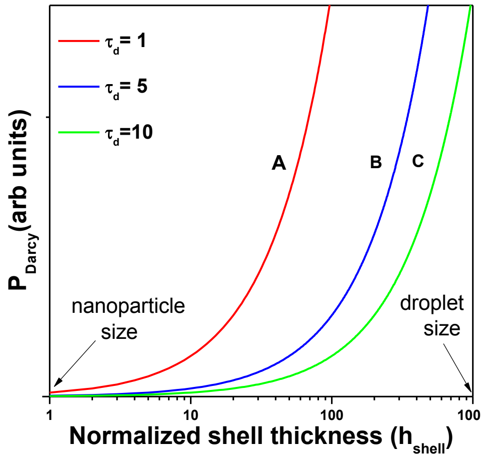

Fig. 2.5 Graphical representation of the variation of Darcy pressure with the shell thickness of granule at different drying times. τ_d and sizes are normalized, therefore unitless.

In summary, the flow of solvent through the shell formed by the accumulated nanoparticles results in a Darcy pressure that induces their aggregation. At small distances between nanoparticles (*d*), colloidal interactions (DLVO) may oppose the aggregation. The DLVO interaction energy, that accounts for a charge induced repulsion and a van der Waals attraction, is written as,

$$W_{total}\left(d\right)=32\pi\varepsilon\varepsilon_0\left(\frac{k_BT}{e}\right)^2\tanh^2\frac{e\zeta}{4k_BT}\mathrm{R}e^{-\kappa d}-\frac{A_HR}{12d} \tag{2.7}$$

For charge-stabilized nanoparticles, the potential reaches a maximum as *d* increases from zero and further goes to zero for large separation distances (Fig. 1.5). In order to account for the effect of the Darcy pressure, an effective potential *W*(*d*) can be written that includes a Darcy pressure term as,[155]

$$W\left(d\right)=32\pi\varepsilon\varepsilon_0\left(\frac{k_BT}{e}\right)^2\tanh^2\frac{e\zeta}{4k_BT}R\,e^{-\kappa d}-\frac{A_HR}{12d}+\pi R^2P_{Darcy}d \tag{2.8}$$

Thus, the Darcy term results in a decrease of the energy barrier for particle aggregation to occur. The larger the DLVO energy barrier, the larger the Darcy pressure must be to reach aggregation. Conclusively, it is the Darcy pressure that induces the aggregation of the nanoparticle and makes the shell elastic, which is necessary to induce buckling.

II. **Buckling of shell:** The buckling instability threshold is given by the Zoelly–Van de Neut condition[156] which relates the critical pressure P_{buck} above which the shell buckles and collapses, to the thickness and mechanical properties of the shell.

$$P_{buck} = 2E\left(\frac{h_{shell}}{R_{shell}}\right)^2 \sqrt{3(1-\nu^2)} \qquad (2.9)$$

where E is the Young modulus, ν is Poisson ratio and R_{shell} is the shell radius which in the upper limit corresponds to the droplet radius R_d. The maximum capillary pressure between the two nanoparticles is[115] $P_{cap} \approx \frac{4\gamma}{d}$ where γ is the air-liquid surface tension and d the interparticle distance. In case of an interparticle distance of $d \approx R/3$, where R is the nanoparticle radius, the capillary pressure (P_{cap}) reaches 100 MPa for 10 nm radii particles in water. Considering the modulus for rigid nanoparticles to be ~ 10^5 Pa,[157] for a shell thickness ranging from $h_{shell} \approx 5R$ to $h \approx R_d/5$, considering a typical ν to be 0.33 (drying network of silica nanoparticles)[158] the critical buckling pressure ranges at most from ~10 to 10^4 Pa. However, P_{buck} remains significantly smaller than the maximal value of the capillary pressure P_{cap} during the whole drying process.

Therefore, the fate of the nanoparticles in a drying scenario is inevitably a jammed granule, be it compact or through shell formation. Darcy pressure resulting from solvent's flow during drying is large enough to overcome DLVO energy barriers even for strong nanoparticle repulsions thereby inducing assembly. In the scenario of shell formation, when the critical buckling pressure is overcome by the capillary pressure, buckled granules are obtained.

Chapter 2.2: Characterization techniques

2.2.1 Introduction

The characterization of nano-structured micro-granules requires access to length scales ranging from that of the constituent nanoparticles to micrometer-sized granule. In this regard, complete structural analysis involves the implementation of complementary techniques, namely scattering and microscopy (or imaging).

Technically speaking, the first step of both the process is the same, which is, interaction of the respective incident radiation with the object under observation. In a scattering experiment, the variation of scattering intensity with scattering angle is recorded and consequently analysed using suitable mathematical models to extract real-space information. Scientifically speaking, the obtained scattered signal is in the reciprocal-space, which is the Fourier transform of real-space density distribution. Scattering, being an indirect method, records this Fourier transformed data, from which real-space data has to be extracted using mathematical models.[159] On the other hand, microscopy, a direct method, reconstructs the object morphology as an image with the help of a lens system (such as optical lenses for optical microscopy). Microscopy re-transforms the data in reciprocal-space to real-space through the lens system and yields an image in the real-space. Fig. 2.6 schematically shows the comparison of the main principle of these two methods. It should be mentioned here that in both the cases, contrast between the object and the medium is mandatory in order to be perceived the probing radiation.

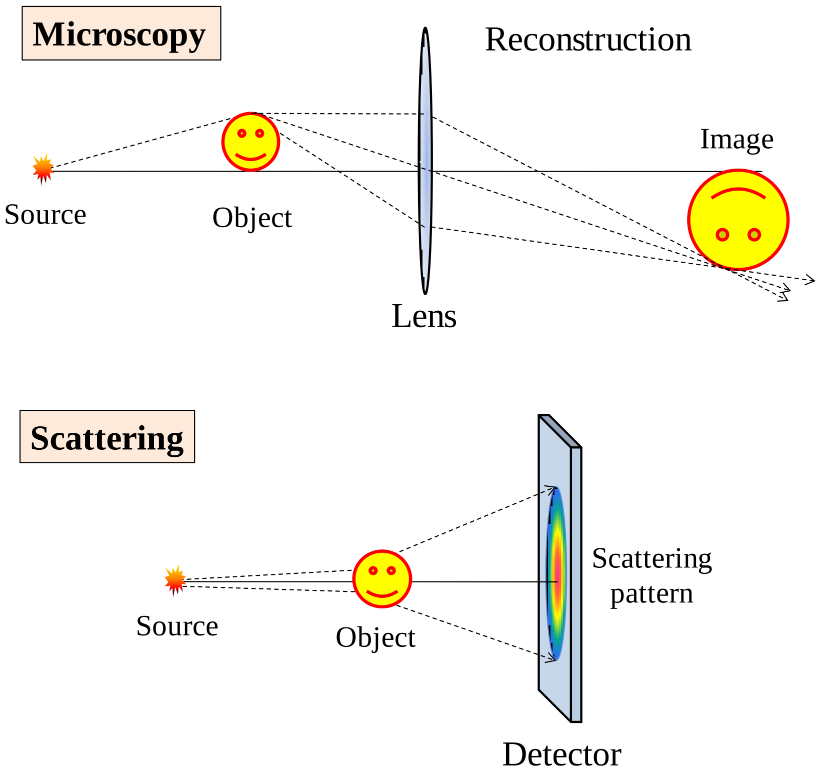

Fig. 2.6 Microscopy and scattering techniques compared.

Both these techniques complement each other to provide information of the object. For example, a crucial advantage of scattering is that it yields statistically averaged information about the area of the sample under the probing radiation. In contrary, local information is perceived by microscopes, which present the sample characteristics superficially. Microscopy, unlike scattering, often requires specially prepared sample, such as staining for optical microscopy,[160] gold-coating on non-conducting surfaces for scanning electron microscope,[161] etc. Obtaining in-situ measurements is easier for the case of microscopy.[162] Contrast variation during scattering experiments provides an immense advantage of structural determination of multi-component samples.[163-165] Therefore, implementation of both these techniques ensures completeness in characterization of nano-structured micro-granules.

Electron microscopy is the most commonly used imaging techniques in micrometric scale.[165] Scanning Electron Microscopy (SEM) and Transmission Electron Microscopy (TEM) are the two types of electron microscopy techniques that work on the two different operation principles. As the name suggests, SEM scans the sample surface with electrons to provide the topological information about the sample. On the other hand, TEM works on the principle of transmission of electron through the sample. Unlike SEM, TEM requires thin sample sizes. Therefore, characterizations of nano-structured micro-granules, whose sizes reach up to few microns, can be challenging using TEM. SEM being a surface scanning technique proves to be very efficient in the present case. Microscopy provides a visual image.

Scattering techniques, on the other hand, is suited for quantification of the sizes and correlation in nano-structured granules. Some common scattering techniques are static and dynamic light scattering (SLS and DLS respectively),[166] small-angle scattering using X-ray (SAXS) or neutron (SANS) as probes, etc. DLS study the diffusive motion of granules which is related to their hydrodynamic and not their actual sizes. Light, having negligible penetration depth, makes SLS technique unsuited for characterization of solid, opaque samples. In the present case, the granules are opaque and in powdered form. Also, owing to the characteristic hierarchical length scales present in the granules, small-angle scattering (SAS) technique is most suitable. It provides quantitative information about the structure (size, shape, number density) as well as the interparticle interactions (volume fraction, interaction potentials).[167] In this thesis, SAS experiments were performed using both X-ray and neutrons as probes. This chapter gives a detailed demonstration of the both of these major techniques that were used for characterization of the granules.

Along with the two above-mentioned techniques, there are further experimental tools, such as gas adsorption technique based on Brunauer–Emmett–Teller (BET) theory, Energy Dispersive X-ray (EDAX), spectroscopy techniques, such as Fourier Transfer Infrared (FTIR), UV-Visible, Raman and also computational tool (Surface Evolver) which were used for specific investigations and will be explained in later chapters.

2.2.2 Scanning Electron Microscopy (SEM)

As the name suggests, SEM scans over a surface with a focused electron beam to create an image. The interaction of the incident electrons in the beam with the sample produces signals that are used to obtain information about the surface topography. A two-dimensional scanning of the surface is carried out by the electron probe and subsequent acquisition of the image from the detected secondary electrons takes place. The number of secondary electrons that can be detected depends on specimen topology. There are a few advantages of SEM over optical microscopy and transmission technique such as TEM. Firstly, unlike TEM (thickness <100 nm), here, the sample can be of bulkier. Secondly, minimal sample preparation is required in this case. The magnification ranges from 20X to ~ 30,000X with a spatial resolution of ~10 nm which is more than that of an optical microscope (~1 μm). Non-conducting samples can also be characterized by a special type of SEM known as Field Emission SEM, where even better resolution is obtained (up to ~1 nm).[168]

In the present thesis, FESEM has been used significantly for characterization of the nano-structured micro-granules. The basic working of SEM and FESEM is the same, except for the type of electron gun used. SEM uses a thermionic emission (TE) gun, whereas, FESEM uses field emission (FE) gun. Below, the basic principle of SEM and description of the instrument is discussed with special mention of FESEM as well.

2.2.2.1 Principle

This technique requires electrons to be accelerated at a high voltage such that efficient probing of the sample is achieved by impingement. The accelerating voltage ranges from a few kV up to 30 kV. At such high voltages, the wavelength of the electron (λ), considering relativistic effects is given by,

$$\lambda = \frac{h}{\sqrt{2m_0eE_0\left(1+{eE_0}/{2m_0c^2}\right)}} \tag{2.10}$$

where 'h' is Planck's constant, E_0 is the applied voltage, 'e' and 'm_0' is the electronic charge (-1.6 x 10^{-19} C) and rest mass (9.1 x 10^{-31} kg) respectively. For the maximum accelerating voltage of 30 kV, the wavelength is ~0.2 nm. When electrons impinge on the sample, they get scattered, gradually losing their energy, finally getting absorbed The extent of electron penetration (R_e) depends on the beam voltage (E_0), the atomic number (Z) and atomic weight (A) of the elements in the sample, and its atomic density (ρ), given by[169],

$$R_e = \frac{0\cdot 0276A}{Z^{0.89}\rho}E_0^{1.67} \tag{2.11}$$

Various simultaneous phenomena (generation of secondary and Auger electrons, back-scattering, cathodoluminescence, etc.) occur after electron incidence, which generate signals. SEM utilizes these signals to characterize the surface or just beneath the surface. Fig. 2.7 shows the various signals that are obtained from sample when an electron beam is incident.

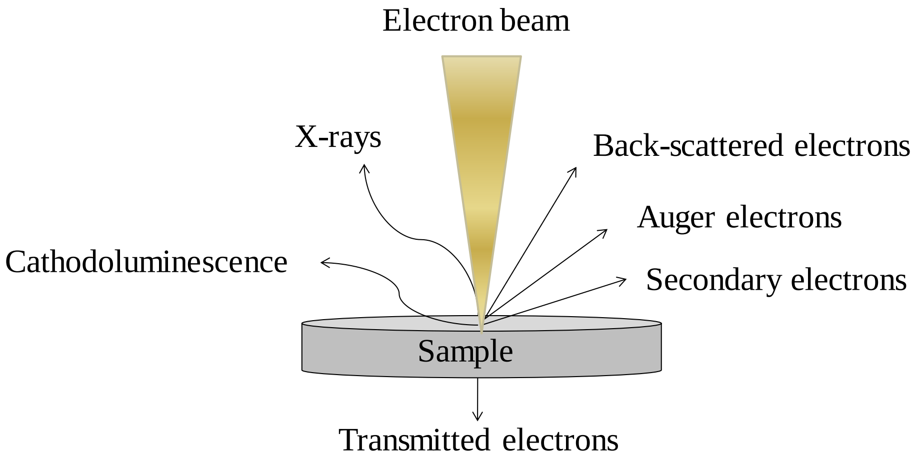

Fig. 2.7 Emission of radiation and particles from the sample illuminated by the electron beam.

I. **Secondary Electrons:** These electrons are produced from the valence shell electrons of the constituent sample atoms. These are low energy electrons, hence, the ones generated deep below the sample surface gets absorbed. Only the ones generated on the surface are emitted and contribute to the detected signal. Secondary electron yield also depend on the tilt angle of the sample surface. The yield is more for an electron beam that incident obliquely than for the one entering perpendicular to the surface. The difference in incident angle of the electron beams is perceived as a difference in brightness on the SEM image. Thus, the modulations on the surface can be recognised by these secondary electrons.

II. **Back-scattered Electrons:** These electrons are actually the incident electrons which are reflected back from the sample. They possess higher energy and contain information from the deeper regions of the sample (compared to the surface) and are sensitive to sample composition. As these electrons are scattered after interacting with the electrons in the sample, thus as Z is larger, the number of back-scattered electrons are also larger. The formed image will have a bright area for locations having high Z elements. In this way SEM also provide the contrasts in chemical composition for multiphase samples, orientations of crystals etc.

III. **Auger Electrons:** The incident electrons can also cause ionization of the atoms in the focussed area. The subsequent relaxation of these atoms release Auger electrons, which is characteristic of the elements present in the area under scan.

IV. **X-rays:** Cases I and II are surface phenomena, whereas III and IV take place in the whole interaction volume in the focussed area of the beam. The incident electrons can also generate characteristic X-rays which can be detected by Energy Dispersive X-ray Spectrometer (EDS) or Wavelength Dispersive X-ray Spectrometer (WDS).[170] The elemental composition can be obtained from the characteristic peaks. A suitable accelerating voltage of the incident electrons should be used to ensure efficient X-ray generation.

V. **Cathodoluminescence:** The bombardment of incident electrons on a sample surface may result in the emission of electromagnetic radiation which can be in the visible (400-700 nm), ultraviolet (UV; <400 nm) or infrared (IR; >700 nm) regions of the electromagnetic spectrum. This general phenomenon is known as luminescence. Depending on the incident radiation and the kinetics of the emission process, luminescence can be categorised as fluorescence (luminescent radiation occurs in $< 10^{-8}$ seconds after the incoming radiation ceases) and phosphorescence (luminescent radiation continues to emit for $>10^{-8}$ seconds and longer after the incoming radiation ceases). In general, cathodoluminescence is the emission of photons of characteristic wavelengths from a material that is under high-energy electron bombardment such as in SEM.[170] The nature of cathodoluminescence in a sample depends on the chemical composition, lattice structure, impurities, strain or damage on the structure of the material.

Along with the above mentioned kinds of detection signals, there are also transmitted and absorbed electrons. The quality of the SEM images primarily depends on the accelerating voltage of the incident electrons. The penetration depth changes when the accelerating voltage is varied. For high accelerating voltages, information from the inside of the surface (interaction volume below the surface) gives an unwanted background which decreases the contrast of the sample surface. Thus, in order to observe a clear image, the accelerating voltage should be optimised.

2.2.2.2 Description of instrument

The basic requirements of a SEM setup are an electron source along with an optical system to produce a scanning probe, a sample stage, a secondary electron detector, an image display unit and an operation control unit. Fig. 2.8 depicts the schematic of the parts of an electron microscope. The electron optical system consists of an electron gun, condenser lens, objective lens to constitute the electron probe, a scanning coil to direct the scanning process. This part of the SEM along with the sample stage is kept at high vacuum (10^{-3}-10^{-4} Pa) to avoid stray interactions of electrons with the air molecules. For this function, diffusion or a turbo-molecular pump is used in general. For FESEM, ultra-high vacuuming (10^{-8} Pa) is required which is achieved by sputter-ion pump.

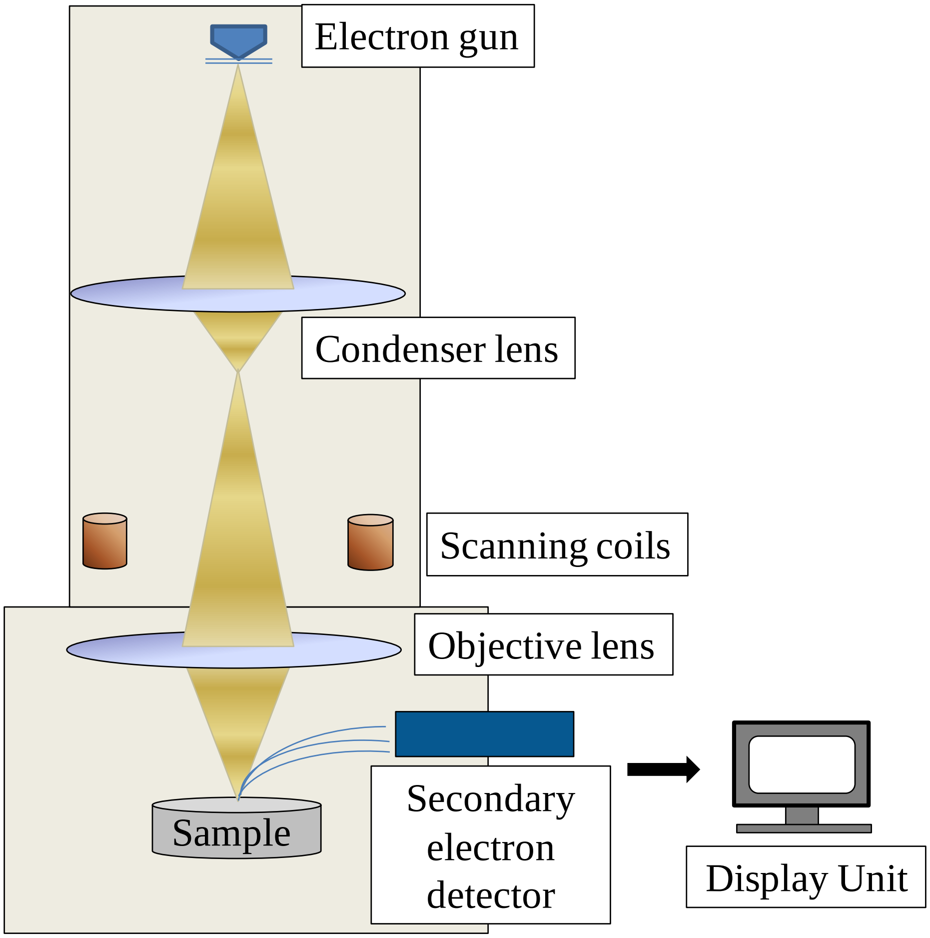

Fig. 2.8 Basic components of SEM.

Signals generated from the specimen are collected by an electron detector, converted to photons via a scintillator, amplified in a photomultiplier, and converted to electrical signals that eventually form the image on the viewing screen. Brief descriptions of the individual parts are given below.

I. **Electron gun:** It produces the electron beam. Usually, it is a thermionic emission gun which generates electrons by thermionic emission from tungsten wire at 2800 K. These thermoelectrons are gathered at the anode by applying a positive bias on the anode. A perforation in the anode serves as an outlet for the electron beam. A third cathode known as the Wehnelt electrode,[170] having a negative bias, is placed between the cathode and anode which focuses the beam and adjust the current in the electron beam. Focusing is achieved at the "crossover" where the beam diameter is 15-20 μm. Other electron guns such as LaB_6 single crystal,[171] Schottky-emission (SE)[172] and field-emission (FE) guns[174] are also used, where the resolution is much better. Fig. 2.9 shows the constructions of thermionic emission and FE gun.

FESEM or Field Emission SEM has a higher resolution (~1.5 nm at 30kV) than conventional SEM. Also, thermionic sources have lesser brightness and are prone to cathode material evaporation and thermal drift during operation. FE gun being a cold cathode field emitter does not heat the filament. The electron emission occurs from the emitter which is a sharp and pointed tungsten wire fitted with a tungsten single crystal. When a positive bias is applied to a metal plate or the extracting electrode situated below the emitter, electrons are emitted from the emitter by tunneling. A second electrode, known as the accelerating electrode is placed below the extracting electrode, which is maintained at a fixed voltage so that the energy of the electrons in the beam is uniform. The tip of the emitter should be extremely clean for the commencement of tunnelling. Hence FESEM requires ultra-high vacuum. The electron beam here has a smaller radius (5-10 nm) than that from a thermionic source (10-20 μm), hence the electron density is more in the former. Energy coherency is extremely crucial to minimize chromatic aberration and increase the resolution. For FE gun sources, electrons have a negligible energy variation; hence coherency of the beam is better. Schematic of FE gun is given in Fig. 2.9.

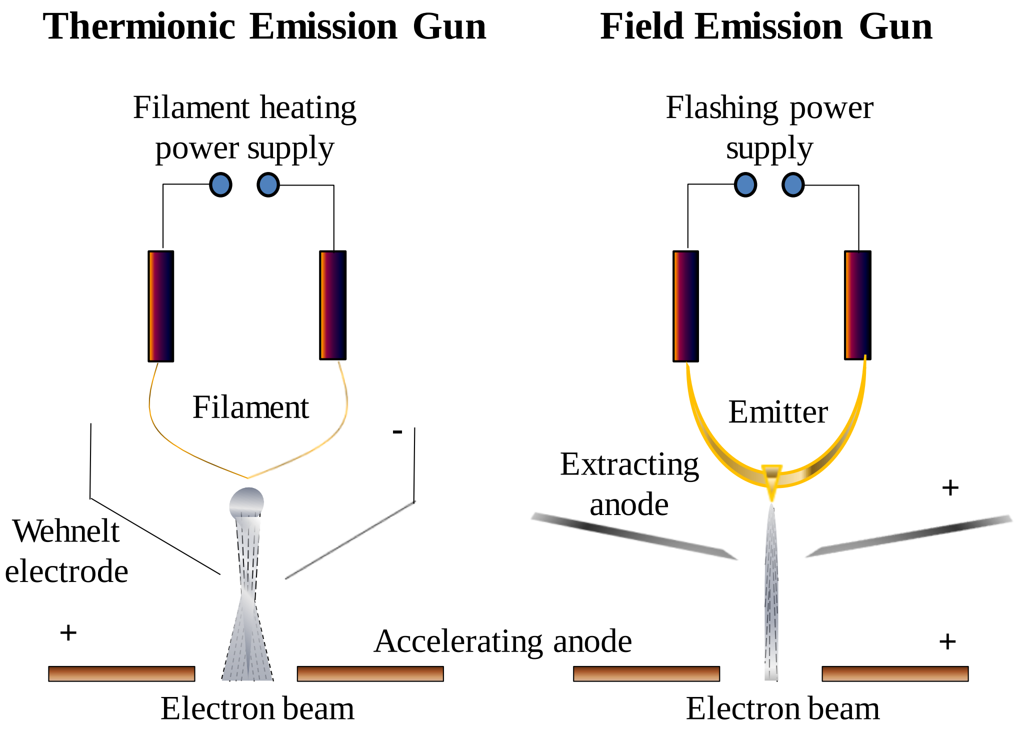

Fig. 2.9 Comparison of the basic components of Thermionic and Field Emission guns.

II. **Lens system:** A magnetic lens system is used in SEM as they are the most suited to produce lens action on charged electrons. It is achieved by passing direct current through a coil producing a rotationally symmetric magnetic field which pushes or collimate the electron beam towards the centre of the coil. The focal length of such a lens is adjusted by tuning the magnetic field lines density by changing the coil current. The lenses are placed below the electron gun in order to achieve efficient adjustment of the beam diameter. The two-stage lens system comprises of the condenser lens at the top and the objective lens at the bottom

III. **Sample stage:** During imaging, the sample is often required to be movable. Hence the sample stage is accordingly designed to provide movement along X-Y-Z direction along with rotation and tilt. X and Y provide the selection of field of view whereas Z provides change in image resolutions and depth of view. The required movement of the sample stage is computer controlled.

IV. **Secondary electron detector:** This detects the secondary electrons that are emitted by the sample. A fluorescent substance is coated on the tip of the detector that receives the electrons acting as the scintillator. A positive bias of 10kV is applied to it. The electrons hit this scintillator producing photons which are then directed to a photomultiplier tube (PMT) through a light guide. Photons get converted into electrons which are amplified as the electric signal.

The amplified signals from the secondary electron detector are transferred to the display unit which is a cathode ray tube (CRT) or a liquid-crystal display (LCD). An image is formed on the monitor screen, which is saved in a digital format.

2.2.3 Small-Angle Scattering (SAS)

SAS is a powerful non-destructive characterization technique, used for investigation of materials' structures, in the mesoscopic length scale[163-164, 167]. The structural features are perceived as inhomogeneities occurring in an otherwise homogeneous medium owing to their inherent density fluctuations. For example, nanoparticles, pores in a porous material, macromolecules in a solvent, precipitates in alloys, etc. The versatility of SAS is owing to the accessible length scale (1-1000 nm) which falls in the domain of nanoscience and technology. André Guinier (1938) is credited with the initiation of formalism of SAS using X-ray as probe[164]. Krishnamurti first utilized SAXS technique for characterization of amorphous systems[175]. Other major contributors to the field include Peter Debye[176], Otto Kratky[163], Günther Porod[177], etc. Recent years has seen momentous developments in SAS technique and its application in fields ranging from classical metallurgy to soft matter, engineering to bioscience and many more.

It is basically a diffraction technique where elastic scattering phenomena is studied at small scattering angles ($0.1\text{-}10^{o}$) close to direct beam which distinguishes it from Bragg diffraction from atomic planes as observed at large angles. SAS delivers the structural data averaged over macroscopic sample volumes overlooking atomic scale irregularities. In contrast to microscopy techniques, such as Transmission Electron Microscopy (TEM) or Field Emission Scanning Electron Microscopy (FESEM), SAS is non-destructive and require minimal sample preparation. The probing radiation in SAS is generally neutrons, X-rays or light.[163] The basic principle and theoretical background is same for all the probes. However, the variation lies in the interaction between the probe and the sample. There are sample-specific advantages of a particular probe with respect to another, according to which a suitable technique is chosen. SAS provides statistically-averaged quantitative information about the structure and correlation of a system whereas imaging technique such as SEM, (as described in section 2.2.2) furnishes the pictorial representation. Thus, both the techniques are complementary to each other for wholesome characterization of the granules. The theoretical foundation of SAS is provided in the following sub-section.

2.2.3.1 Theoretical Background

SAS technique requires a monochromatic beam of radiation to be incident on the sample. The intensity of the scattered radiation is measured as a function of the scattering angle, which is then analysed to provide information about the mesoscopic structures present in sample. Fig. 2.10 shows schematic of a typical scattering experiment. The wave vector of incident and scattered radiation is denoted by $\vec{k}_i$ and $\vec{k}_s$, respectively. The difference between the two wave vectors is due to the scattering event. As SAS considers only elastic scattering events, the magnitude of the wave vectors are considered to be equal, $|k_i|=|k_s|$, although there is a change in the direction of scattered radiation with respect to the incident direction. Hence, analyzing the scattering pattern will provide information about the required sample properties. The magnitude of the wave vectors is given as $k_i = k_s = \frac{2\pi}{\lambda}$ where λ is the wavelength of the radiation. Phase difference between the incident and the scattered wave is $\left(\vec{k_s} - \vec{k_i}\right) \cdot \vec{\Delta r}$ where $\vec{q} = \vec{k_s} - \vec{k_i}$ is defined as the wave vector transfer. Magnitude of $\vec{q}$ is $|q| = 2k\sin\theta$ where 2θ is the scattering angle. Therefore, $q = \frac{4\pi\sin\theta}{\lambda}$. At the lower limit, $2\theta = 0^{\circ}$, $q_{min} = 0$. At the other extreme, maximum scattering is $2\theta = 180^{\circ}$, $q_{max} = \frac{4\pi}{\lambda}$. Neither of the extremes is achievable due to interference of the incident beam.

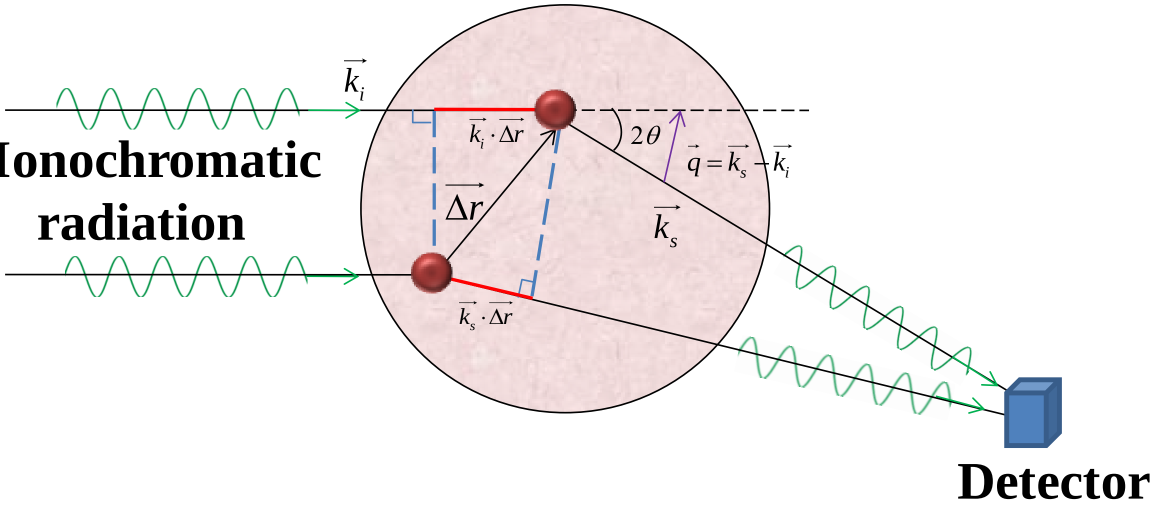

Fig. 2.10 A typical scattering experiment where scattering from two random scatterers in the object has been depicted.

It is to be mentioned here that $\vec{q}$ is the Fourier transform of the real length scale $\vec{r}$. Hence to probe a larger length scale, q should be close to q_{min} or at small angles. In general, SAS falls in the regime where $2\theta < 10^{\circ}$. Hence by SAS, structures having dimensions beyond the atomic length scale (mesoscopic) can be probed compared to scattering techniques at wide angles (WAS) which provide information on the atomic length scales.

2.2.3.2 Basic formalism

As mentioned earlier, SAS is inherently identical irrespective of the probing radiation. However, it should be noted that neutrons interact with atomic nuclei[179-181] and X-rays (SAXS)[163-164, 167] interact with electrons to emit secondary waves, which interfere with each other producing detectable signals. The strength of a scattering interaction is quantified in terms of scattering length. For an incident plane wave of the form $e^{i\vec{k}_i.\vec{r}}$, interacting with a scatterer at the origin (r=0), the scattered wave is given by $-\frac{b(\theta)}{r}e^{ik_i.r}$. $b(\theta)$ has the dimension of length and is known as the scattering length. For X-rays, $b(\theta)$ is dependent on the atomic number of an element and θ, whereas, for neutrons, the interaction is θ-independent and element specific.

The scattering cross-section describing the flux scattered in the solid angle $d\Omega$ is denoted by $\frac{d\sigma}{d\Omega}$ and is called as microscopic differential scattering cross section. The total scattering cross section $\frac{d\sigma}{d\Omega}$ integrated over all solid angles is given by $\sigma = 4\pi b^2$. For an assembly of scatterers, $\frac{d\sigma}{d\Omega}$, averaged over all orientations,

$$\frac{d\sigma}{d\Omega}(q) = \left\langle \left| \sum_i b_i e^{-i\vec{q}.\vec{r}_i} \right|^2 \right\rangle \tag{2.12}$$

where $\vec{r}_i$ is the position of the i^{th} scatterer in the sample. For X-ray b_i is the atomic scattering factor of the i^{th} atom for X-rays given by $\frac{Ze^2}{m_0c^2}$ where Z is the atomic number and $\frac{e^2}{m_0c^2}$ is the classical electron radius. Similarly, for neutron it is the bound atom scattering length dependent on the neutron-nucleus interaction strength. Since SAS probes large-scale inhomogeneities, therefore, the individual scattering length b_i is replaced by locally averaged scattering length density $\rho\left(\vec{r}_i\right)$. Hence Eq. 2.12 becomes,

$$\frac{d\sigma}{d\Omega}(q)=\left\langle\left|\int \rho\left(\vec{r}\right)e^{-i\vec{q}.\vec{r}}d\vec{r}\right|^2\right\rangle \tag{2.13}$$

where $\rho\left(\vec{r}_i\right)$ is $\rho\left(\vec{r}_i\right)=\frac{1}{V\left(\vec{r}\right)}\sum_i b_i$ and the summation is over all scatterers in volume $V\left(\vec{r}_i\right)$.

Considering a solute (sample) having scattering density distribution ρ_S (total volume V_S), in a solvent (medium) with ρ_M (total volume V_M), Eq. 2.13 is written as,

$$\frac{d\sigma}{d\Omega}(q)=\left\langle\left|\rho_S\int_{V_S} e^{-i\vec{q}.\vec{r}}d\vec{r}+\rho_M\int_{V_M} e^{-i\vec{q}.\vec{r}}d\vec{r}\right|^2\right\rangle$$

Rearranging,

$$\frac{d\sigma}{d\Omega}(q)=\left\langle\left|\left(\rho_S-\rho_M\right)\int_{V_S} e^{-i\vec{q}.\vec{r}}d\vec{r}+\rho_M\left[\int_{V_M} e^{-i\vec{q}.\vec{r}}d\vec{r}+\int_{V_S} e^{-i\vec{q}.\vec{r}}d\vec{r}\right]\right|^2\right\rangle \tag{2.14}$$

The second term behaves like a delta function which exists at q close to zero and thus, can be neglected for all non-zero q values. Hence Eq. 2.14 becomes,

$$\frac{d\sigma}{d\Omega}(q)=\left(\rho_S-\rho_M\right)^2\left\langle\left|\int_{V_S} e^{-i\vec{q}.\vec{r}}d\vec{r}\right|^2\right\rangle$$

After normalisation with the sample volume, V_{sample}, the macroscopic differential cross section $\frac{d\Sigma}{d\Omega}(q)$ is obtained, i.e.,

$$\frac{d\Sigma}{d\Omega}(q)=\frac{1}{V_{sample}}\cdot\frac{d\sigma}{d\Omega}(q)=\frac{\left(\rho_S-\rho_M\right)^2}{V_{sample}}\left\langle\left|\int_{V_S} e^{-i\vec{q}.\vec{r}}d\vec{r}\right|^2\right\rangle \tag{2.15}$$

where $(\rho_S - \rho_M)^2$ is known as the contrast factor which governs the "distinctiveness" of an inhomogeneity by the probing radiation, i.e, if contrast is low, the inhomogeneity appears smeared. Eq. 2.15 can be written as,

$$\frac{d\Sigma}{d\Omega}(q) = \frac{(\rho_S - \rho_M)^2}{V_{sample}} V_p^2 \left\langle \left| \sum_k F_k(\vec{q}) e^{-i\vec{q}.\vec{r_k}} \right|^2 \right\rangle \tag{2.16}$$

where $\vec{r_k}$ is the position vector of the k^{th} inhomogeneity, V_p is its volume and

$F(\vec{q}) = \frac{1}{V_p} \int_{V_p} e^{-i\vec{q}.\vec{r}} d\vec{r}$ which is normalized such that $|F(0)|^2 = 1$. For a monodisperse system, having N_p number of identical particles, each having volume V_p, Eq. 2.16 is expressed as,

$$\begin{aligned}\frac{d\Sigma}{d\Omega}(q) &= \frac{N_p(\rho_S - \rho_M)^2 V_p^{\ 2}}{V_{sample}} \left\langle \left| F(\vec{q}) \right|^2 \right\rangle \cdot \frac{1}{N_p} \left\langle \left| \sum_k e^{-i\vec{q}.\vec{r_k}} \right|^2 \right\rangle \\ &= \frac{N_p(\rho_S - \rho_M)^2 V_p^{\ 2}}{V_{sample}} P(q) S(q)\end{aligned} \tag{2.17}$$

where $P(q)$ is the intra-particle structure factor by $P(q) = \left\langle \left| F(\vec{q}) \right|^2 \right\rangle$. It is also known as the form factor as it depends on the shape and size of a particle. $S(q)$ is inter-particle structure factor $S(q) = \frac{1}{N_p} \left\langle \left| \sum_k e^{-i\vec{q}.\vec{r_k}} \right|^2 \right\rangle = 1 + \frac{1}{N_p} \left\langle \sum_k \sum_{k'} e^{i\vec{q}.(\vec{r_k} - \vec{r_{k'}})} \right\rangle$ which depends on the correlation between particles in the sample. For a dilute suspension, $S(q)$, the particles are situated far enough to consider $S(q)$ to be 1. Incorporating fractional volume (ϕ) of the particles in the sample $\phi = \frac{N_p V_p}{V_{sample}}$, Eq. 2.17 becomes,

$$\frac{d\Sigma}{d\Omega}(q) = \phi(\rho_S - \rho_M)^2 V_p P(q) S(q) \tag{2.18}$$

Often scattering intensity is required for powder samples. In such cases, the intensity $I(q)$ is plotted as a function of q in arbitrary units instead of $\frac{d\Sigma}{d\Omega}(q)$. Putting $n=\frac{N_p}{V_{sample}}$ where '*n*' is the number density of particles $I(q)$ becomes,

$$I(q)=n(\rho_S-\rho_M)^2 V_p^2 P(q)S(q) \tag{2.19}$$

Typical functionality of $P(q)$, $S(q)$ and $\frac{d\Sigma}{d\Omega}(q)$ is given in Fig. 2.11. *P*(*q*) and *S*(*q*) for the specific cases will be discussed in the later chapters.

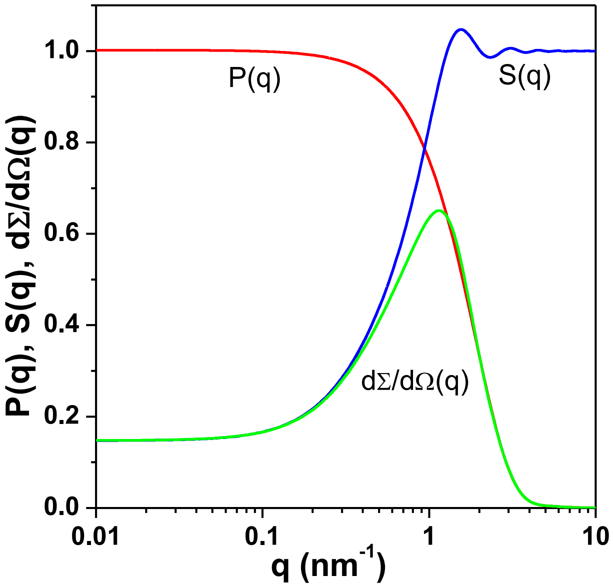

Fig. 2.11 Graphical representation of $P(q)$, $S(q)$ and $\frac{d\Sigma}{d\Omega}(q)$

So far, it was considered that the particles are monodisperse with respect to size and shape. However, in the reality, this is not the case. There exist a polydispersity, i.e, a size distribution (*D*(*R*)) needs to be considered. Under local monodisperse approximation,[182] which assumes that a particle of a certain size is always surrounded by particles of the same size, scattering is approximated as a collection of monodisperse subsystems, weighted by the size distribution. In such a case,

$$I(q)=\frac{n(\rho_S-\rho_M)^2\int_0^\infty V_p^2(R)P(q,R)S(q,R)D(R)\,dR}{\int_0^\infty D(R)\,dR} \tag{2.20}$$

D(*R*) can have various forms such as Gaussian, log-normal, Schultz, etc. Log-normal distribution has the form

$$D(R)=\frac{1}{R\sigma\sqrt{2\pi}}e^{\frac{-\left(\ln\frac{R}{\mu}\right)^2}{2\sigma^2}} \tag{2.21}$$

where μ and σ are the median radius and polydispersity index (varies between 0 and 1), respectively. The mean and median values are related as $R_{mean}=\mu e^{\frac{\sigma^2}{2}}$ and the standard deviation is given by $\sqrt{e^{2\mu+\sigma^2}\left(e^{\sigma^2}-1\right)}$.

The analysis of object morphology can be carried out coarsely by the inspection of the asymptotic behaviour of the SAS profiles. Given below are some simplified methods by which a rough idea about the system under observation can be obtained.

I. **Guinier Approximation:** An idea about the geometrical dimension of the object[164] under investigation can be made by only considering the limiting behaviour of the intensity plot close to $q\rightarrow 0$. By this approximation, any form factor function can be assumed to be a Gaussian function in the small-angle limit. However, this is applicable for very dilute systems where the structure factor *S*(*q*) is taken to be unity and $q<{}^{1}\!/\!_{R_g}$. Radius of gyration, R_g is defined as the root-mean-square (RMS) of the scattering length density weighted distances from the centre of mass to each scatterer in the object. For a monodisperse dilute system of spheres, the intensity at this limit can be written as,

$I(q)=I(0)e^{-\frac{R_g^2q^2}{3}}$ where $I(0)=(\Delta\rho)^2\ nV_p^2$ and $R_g=R\sqrt{3/5}$. Similarly for a polydisperse system, $I(q)=I(0)e^{-\frac{q^2}{5}\cdot\frac{\langle R^8\rangle}{\langle R^6\rangle}}$ where $\langle R^n\rangle$ is the nth moment of the radial distribution function. Thus, regardless of the shape of the object, it is possible to determine the mean size from the scattering data at $q\rightarrow 0$ limit.

II. **Porod Approximation:** The asymptotic behaviour of intensity at the limit of high q is described by this approximation.[177] For randomly oriented 3D solid objects with sharp interfaces, the intensity in high q region ($q >> \pi/R_g$) follows power-law decay of q^{-4}. Porod constant P is defined as $P=\lim_{q\to\infty}q^4I(q)$. The form factor $P(q)$ is given by $P(q)=2\pi\frac{S}{V_p^2}\cdot\frac{1}{q^4}$ where S and V_p are the total surface area and volume of the inhomogeneity. $I(q)$in such a case is,

$$I(q)=\frac{2\pi n(\Delta\rho)^2S}{q^4} \tag{2.22}$$

Hence the total surface area S of the inhomogeneity can be obtained from P. For a polydisperse system of spheres, $\lim_{q\to\infty}I(q)=6\pi(\Delta\rho)^2\phi\frac{\langle R^2\rangle}{\langle R^3\rangle}\frac{1}{q^4}$.

III. **Scattering invariant:** The volume integration of the entire scattering range is given by the scattering invariant Q,

$$Q=\int_0^\infty q^2I(q)dq \tag{2.23}$$

For a dilute solution, $Q=(\Delta\rho)^2\phi$ whereas for concentrated systems, $Q=(\Delta\rho)^2\phi(1-\phi)$ where ϕ is the volume fraction of the particle. Hence from the scattering plot, Q can be determined which provides the concentration of system. Thus, for the calculation of specific surface area S/V_p, scattering data in the absolute scale is not required as $\frac{S}{V_p}=\pi\phi(1-\phi)\lim_{q\to\infty}\frac{q^4I(q)}{Q}$.

2.2.3.3 Description of instrument

I. **Small-Angle X-ray Scattering (SAXS):** SAXS measurements were carried out using laboratory-based SAXS facility with a sample to detector distance of nearly 1 m. Fig. 2.12 describes the experimental setup schematically. The basic components of a SAXS instrument are a source, pin-hole collimation system comprising of the mirror and slits, sample in the sample chamber, beam stop and a detection system consisting of the detector tube and detector. X-rays from the source is collimated to ensure the small-angle regime, which then irradiates on the sample. The beam stop prevents the bright intensity of the direct beam to hit the detector so that the scattering from the sample can be obtained.

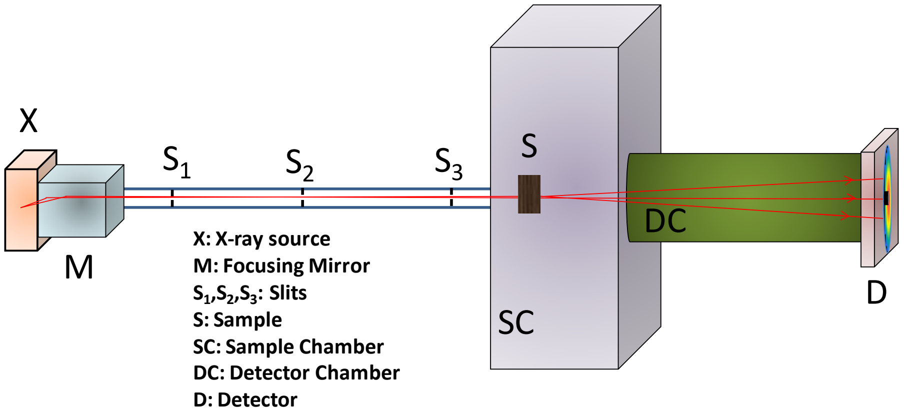

Fig. 2.12 Schematic representation of a laboratory-based SAXS instrument.

The X-ray source is a sealed tube as represented in Fig. 2.13. The electrons emitted from the filament impinge upon an anode or a target (made out of copper). A high voltage (30-45 kV) is applied between the anode and the filament. The components are placed in a vacuum housing. For a Cu anode, K_α (1.54 Å). The intensity of the tube (number of X-ray photons) is controlled by the operational voltage. The typical filament current is around 0.5-0.7 mA.

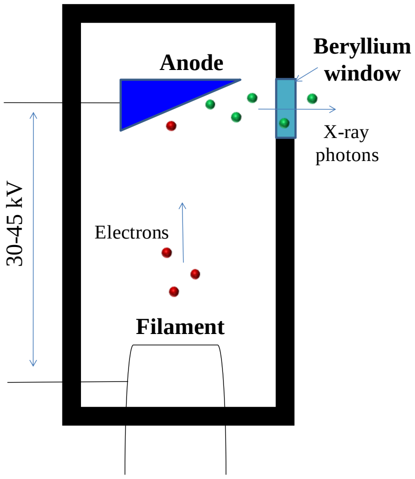

Fig. 2.13 Sealed X-ray tube.

After generation of the X-ray beam, the second step is collimation. It is achieved by a system of slits (line collimation) or pinholes (point collimation) through which the X-rays pass through. There are also multi-layer optical arrangements which minimize the instrumental broadening. The sample environment depends on the physical state of the samples. For examples, liquids are measured inside a thin-walled capillary, whereas, powder samples are placed in a sample holder with removable windows made of Kapton® foil. A 2D detector detects elastically scattered signal from the sample. The accessible wave vector transfer (q) range was ~0.1 to 3.0 nm^{-1}. Standard calibrants such as silver behenate is used to determine the sample to detector distance. Glassy carbon or water is used to calibrate the absolute intensity.

Data reduction and analysis

The measurement of scattering intensity is two-fold. First, the measurement must be done for the sample, followed by that of the matrix element (e.g. solvent). The scattering from the latter is to be subtracted from that of the sample. Once the scattered signal is collected at the 2D detector, a number of correction procedures are performed. The position of each pixel in the detector corresponds to a scattering angle 2θ or scattering vector q, by taking into account the wavelength, pixel size and sample-to-detector distance. If the image obtained at the detector is azimuthally isotropic, radial averaging of the 2D image is performed to obtain 1D scattering profile as shown below (Fig. 2.14).

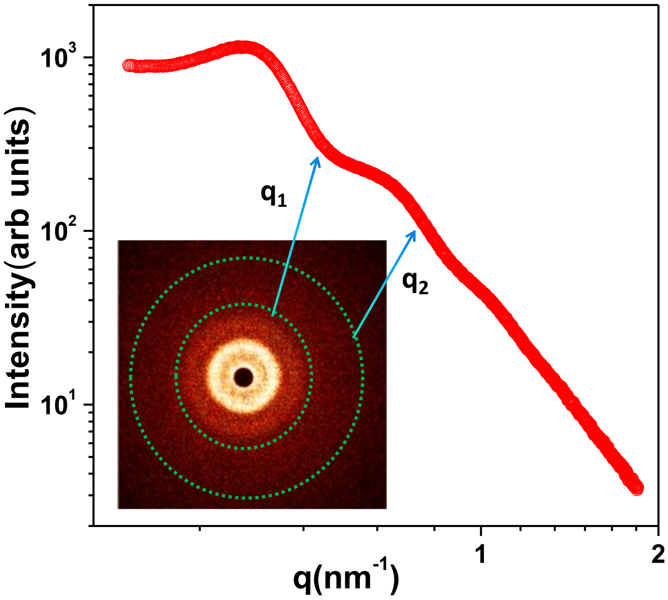

Fig. 2.14 One-to-one correspondence of the 2D scattering image with the obtained profile for spray-dried HS-40 nano-silica granules. The two green circles in the image represent two q values q_1 and q_2.

The x-ray transmission value of a sample is obtained from scattering from glassy carbon. Any measured signal contains background which originates from air, X-ray windows, empty cell, etc. This contribution is removed by subtracting the intensity of the empty container I_{cont} from that of the sample in the same container $I_{cont+sample}$ considering the transmission factors (t_{cont} and $t_{sample+cont}$) for each by,

$$I_{sample} = \frac{I_{sample+cont}}{t_{sample+cont}} - \frac{I_{sample+cont}}{t_{cont}} \qquad (2.24)$$

II. **Medium resolution Small-Angle Neutron Scattering (MSANS):** The SANS measurements in this thesis was carried out at the double-crystal (DC) based MSANS instrument at Dhruva reactor, Mumbai (Photograph in inset of Fig. 2.15). It has been mentioned earlier that the nano-structured micro-granules consist of hierarchical length scales, spanning several decades of q-value. In this regard, MSANS cover the low q region (0.003–0.173 nm^{-1}) which probes the larger length scale, beyond nanoparticlular sizes. The schematic of the instrument layout is shown in Fig. 2.15.

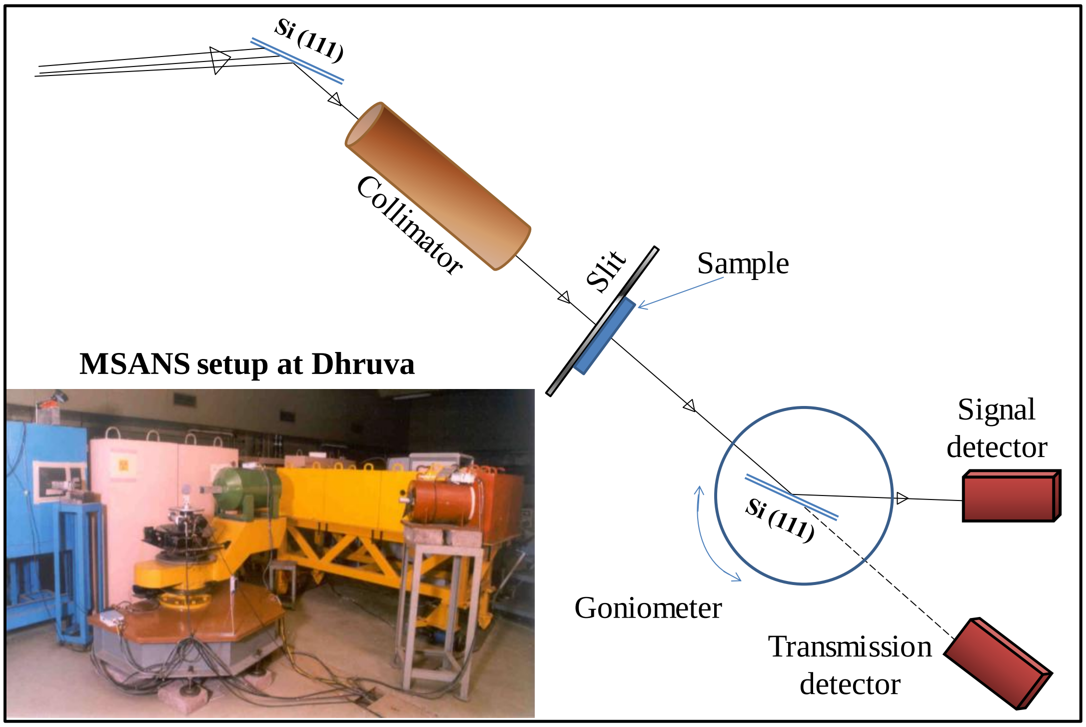

Fig. 2.15 Schematic representation of DC-based MSANS instrument. **INSET**: Photograph of MSANS instrument at GT lab, Dhruva reactor, Mumbai.

The DC type of setup varies from the pin-hole collimation setup in a sense that here, the sample is placed between the two crystals, the monochromator and the analyzer which are set at a non-dispersive geometry. Scattering profiles are recorded by rotating one crystal against other. Unlike, pinhole collimation instrument, at a DC setup, the collimation is performed in the reciprocal space and the resolution in wave-vector transfer q is independent of the beam cross-section. Due to the non-dispersive setting of the crystals, the width of the rocking curve is independent of the divergence of the incoming beam. The q-resolution exists in one dimension only and slit corrections have to be applied to the recorded data. Therefore 2D detectors are not required in this kind of setup. Moreover, the requirement for long collimation paths is bypassed in the DC setup making the instruments compact. However, the measurement time is long as data-taking (recording of scattering intensity) involves a step-by-step rotation of the analyser crystal. The detailed instrument description is given below.

The cross-sectional dimension of the neutron beam coming from the guide is 2.54 cm (horizontal) × 10.4 cm (vertical). Two silicon crystals (diameter 8.25 cm and thickness 0.6 cm) cut parallel to (111) planes are used as the monochromator and analyzer. Neutrons having wavelength λ=0.312 nm are obtained after monochromatization with $\Delta\lambda/\lambda$=1%. The monochromator crystal is set on a normal goniometer. The monochromatic neutrons then pass through a 1 m long cadmium collimator having dimensions 2 cm x 5 cm. The analyzer crystal is placed 100.5 cm away from the sample and is set on a goniometer with smallest control step size of 0.0012^o. The scattered neutrons are detected by a BF_3 proportional counter of 3.81 cm diameter placed 55 cm away from the centre of the analyzer crystal. There is a similar detector located behind the analyzer crystal for measuring the transmission through the sample. The minimum count-rate at this detector corresponds to the maximum count-rate of the main detector when the analyzer is in the Bragg position. Thus, the Bragg angle can be determined this way. The recorded scattering profiles were corrected for background and transmission after deconvolution from the instrument resolution, as described below.

Data reduction and analysis

The measured scattering profile $I_{meas}(q)$ of a sample consist of a transmitted part $I_t(q)$, and a scattered part $I_s(q)$ along with a background B arising due to scattering from air, slits, incoherent scattering from the sample, and crystals, etc. Therefore,

$$I_{meas}(q) = I_t(q) + I_s(q) + B \qquad (2.25)$$

Neglecting the smearing effect, Eq. 2.25 can be written as,

$$I_{meas}(q) = e^{-t\Sigma_{tot}}\, I_m(q)\left\{1 + t\Omega \frac{d\Sigma}{d\Omega}(q)\right\} + B \qquad (2.26)$$

where t is the sample thickness; Σ_{tot} is the linear attenuation coefficient in the sample, $I_m(q)$ is the measured rocking curve of the instrument, 'Ω' is the solid angle of the measurement, and $\frac{d\Sigma}{d\Omega}(q)$ is the slit-smeared differential scattering cross-section of the sample per unit volume per unit solid angle. At zero angle, the full intensity of the beam passes through the DC analyser, hence the measured transmission T_{meas} is given by $T_{meas} = \frac{I_{meas}(0)}{I_m(0)}$. However, the true transmission is, $T_{true} = e^{-t\Sigma_{tot}}$ and at q=0, the actual $\frac{d\Sigma}{d\Omega}(0) \neq 0$. Therefore, T_{meas} is greater than T_{true} . Rearranging Eq. 2.26 and substituting T_{true}, and Ω (in terms of $\Delta\theta_h$ $\Delta\theta_v$),

$$\frac{d\Sigma}{d\Omega}(q)=\frac{\dfrac{I_{meas}(q)-B}{T_{true}}-I_m(q)}{I_m(0)\Delta\theta_h\Delta\theta_v t}\approx\frac{\dfrac{I_{meas}(q)-B}{T_{meas}}-I_m(q)}{I_m(0)\Delta\theta_h\Delta\theta_v t}=\frac{I(q)}{I_m(0)\Delta\theta_h\Delta\theta_v t}$$

where $I(q)$ is the transmission and background corrected scattering profile. $\Delta\theta_h$ is the full width at the half maxima of the intensity profile at the blank measurement. The half-width (θ_D) of the plateau of Darwin reflectivity function[183] for the present MSANS instrument is estimated[184] to be 1.06237". In the present case, $\Delta\theta_h$ is 0.01 rad and $\Delta\theta_v$ is 1.5×10^{-4} rad.[184] $\Delta\theta_v$ is calculated from the ratio of detector aperture to sample-detector distance. Considering the smearing effect on scattering profile due to instrumental resolution, Eq. 2.25 can be rewritten as,

$$I_{meas}(q)=e^{-t\Sigma_{tot}}\left\{I_m(q)+\iint dq_v dq_h\, I_0(q_h)W_v(q_v)\,t\,\frac{d\Sigma}{d\Omega_d}\left(\sqrt{(q-q_h)^2+q_v^2}\right)\right\}+B$$

where q_h and q_v are the components of the q in the horizontal and vertical directions respectively; $I_0(q_v)$ and $W_v(q_v)$ are the theoretical rocking curve and the normalized resolution function of the instrument along the vertical direction in q-space. $\frac{d\Sigma}{d\Omega_d}(q)$ is the de-smeared differential scattering cross section of the sample per unit volume per unit solid angle. $I_0(q)$ is a sharply falling function which is approximated as a Delta function, hence the intensity profile after transmission and background correction is given by, $I(q)=C\int W_v(q_v).t.\frac{d\Sigma}{d\Omega_d}\left(\sqrt{q^2+q_v^2}\right)$. De-smearing of the profiles were carried out by the iterative method developed by Lake.[185] Fig. 2.16 compares the scattering profiles before and after the de-smearing operation.

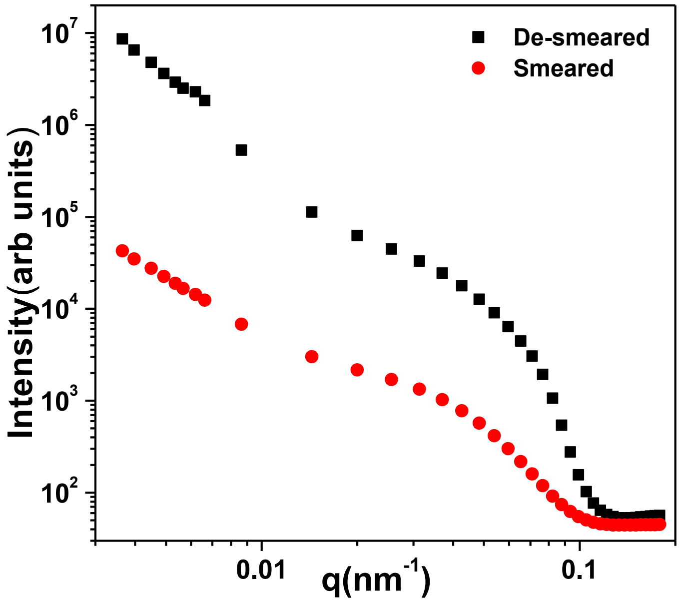

Fig. 2.16 Comparison of smeared and de-smeared profiles for spray-dried HS-40 nano-silica micro-granules.

Modelling of the experimental data is carried out using non-linear least square method primarily with the help of SASFIT software[186]. The obtained fitting parameters are then corroborated with the results of FESEM or other characterization techniques. Thus, wholesome structural information is incurred with the implementation of multiple techniques which are complementary in nature.

Chapter 3.1: Effect of drying temperature on the granular morphology

3.1.1 Preamble

The process of spray-drying facilitates a fair control of various morphological aspects of the formed granules through tuning of certain physicochemical parameters during drying of contact-free colloidal droplets.[46, 65] One such crucial factor is the drying rate. When drying commences, the liquid phase starts to evaporate from the droplets. The thinning bridges of liquid between the nanoparticles cause the emergence of attractive capillary forces, ultimately interlocking the particles into a granular structure.[125, 187] During drying, the droplet can be viscoelastic depending on the experimental time scale, i.e. energy can either be stored in elastic deformation or stress can be relieved through viscous flow.[151] Moreover, the drying process is rapid and non-equilibriated[153] and the characteristics of the end product depend on various physicochemical factors. When the packing of the particles is isotropic, compact spherical granules are obtained as described in part 2.1.3.1 of the previous chapter. However, in other instances, hollow granules are obtained as a result of interlocking at the droplet periphery. For a colloidal droplet exposed to a preset drying temperature, the assembly process commences owing to the motion of the nanoparticles. Such motion is triggered by the gradually developing temperature gradient between the periphery and the core of the droplet.

The present section illustrates the role of drying temperature in controlling the morphology of spray-dried granules.[188] It has been demonstrated that the morphology of the granules gradually shifts from spherical to toroidal with the increase in drying temperature. A rigorous investigation of the origin of temperature-dependent shape transformation has been illustrated in this section with the help complementary characterization techniques, affirmed by droplet drying theory and simulations as well.

3.1.2 Methodology

Aqueous dispersion of spherical nano-silica suspension (TM-40 LUDOX®, Sigma-Aldrich) was prepared in 2 wt% concentration in 100 mL. Spray drying of this suspension was carried out using laboratory spray dryer LU-228, LABULTIMA, India at four drying temperatures, 110^{o}C, 130^{o}C, 160^{o}C, 180^{o}C. The aspirator rate was kept fixed at 50m^{3}/hour. The feed rate of the aqueous dispersion was a constant 2 mL/min and the atomization rate of 2 kg/cm^{2}. The drying temperatures were maintained up to an accuracy of 1^{o}C. Corresponding to each of the drying temperatures, the granules were named as G-110, G-130, G-160 and G-180. The droplet size distribution was obtained using GRIMM 1.108 aerosol spectrometer.

Basic characterization of the granules was carried out using Carl Zeiss Auriga FESEM model. Dynamic light scattering (DLS) experiments were performed for an overall size estimation by HORIBA DLS spectrometer using diluted aqueous dispersion (1 wt%) of the granules using a laser of wavelength 532 nm. Consistency of the DLS results was checked by performing several scans on each sample. The granules were well dispersed throughout the period of DLS measurements.

Characterizations by small-angle scattering (SAS) were carried out by both X-rays (SAXS) and neutrons (MSANS) at the instruments described in the previous chapter.

3.1.3 Results and Discussions

Overall structure of the granules and the correlation among the nanoparticles in the granules has been discussed in this section. Morphological variation with dying temperature has been stepwise elaborated, starting from drying of the droplet. The chronological process has also been illustrated with the help of simulation by Surface Evolver.[189]

3.1.3.1 Granular size distributions from FESEM and DLS

Overall granular sizes and shapes were perceived from FESEM micrographs. Fig. 3.1 depicts the micrographs corresponding to the four drying temperatures. It is seen that granules synthesized at lower drying temperatures (G-110 and G-130) are spherical whereas those synthesized at higher temperatures (G-160 and G-180) have distorted spherical shapes, bordering on doughnut-like morphologies as the temperature of drying is increased. Specifically, G-110 granules are perfectly spherical, a slight dented exterior is seen for G-130, prominent invagination is perceived for G-160, whereas G-180 granules are distinctly toroids or doughnut-shaped. The emergence of toroidal shape for G-180 is due to the interpenetration of two diametrically opposite invagination zones eventually forming the central hole.[152] The zoomed views of the surfaces are shown as the insets of the micrographs. The extent of local ordering of the nanoparticles is more for the first two cases (G-110 and G-130) than the others.

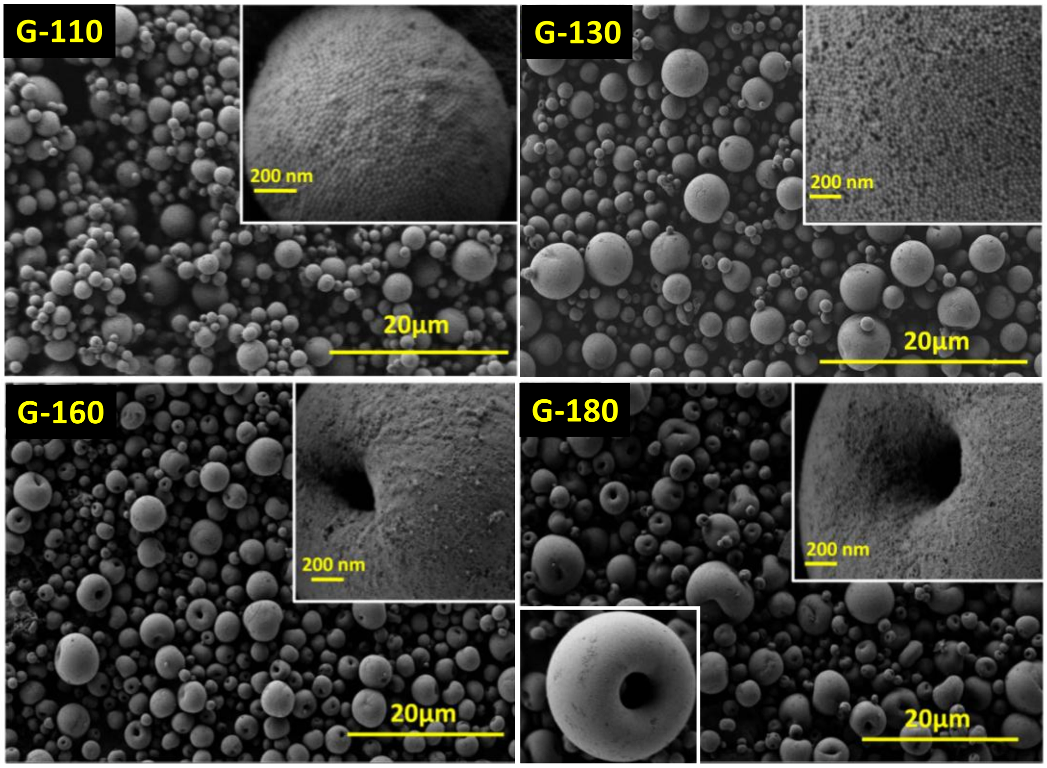

Fig. 3.1 FESEM micrographs of the powder granules at 5000X magnification. Insets show the zoomed view of a granule for each case, emphasizing on the surface features.

The granule volume distribution was estimated from the micrographs using ImageJ software (http://imagej.nih.gov/ij/download.html). Histograms for the same are plotted in Fig. 3.2(a). These distributions were compared with the volume distribution obtained from DLS, considering hydrodynamic sizes. It is seen that the polydispersity trends corroborate fairly well with that obtained from the image analysis of the FESEM micrographs. The normalized auto-correlation ($g^2(\tau)$) was plotted as a function of delay time (τ)[190] in Fig. 3.2(b). The volume distributions were estimated from auto-correlation function by fitting with log-normal type of distributions[191] of the form given in Eq. 2.21. G-160 and G-180 depict a larger size compared to G-130 and G-110. Thus, microscopy along with DLS provides the overall granular shapes, size distributions and polydispersities.

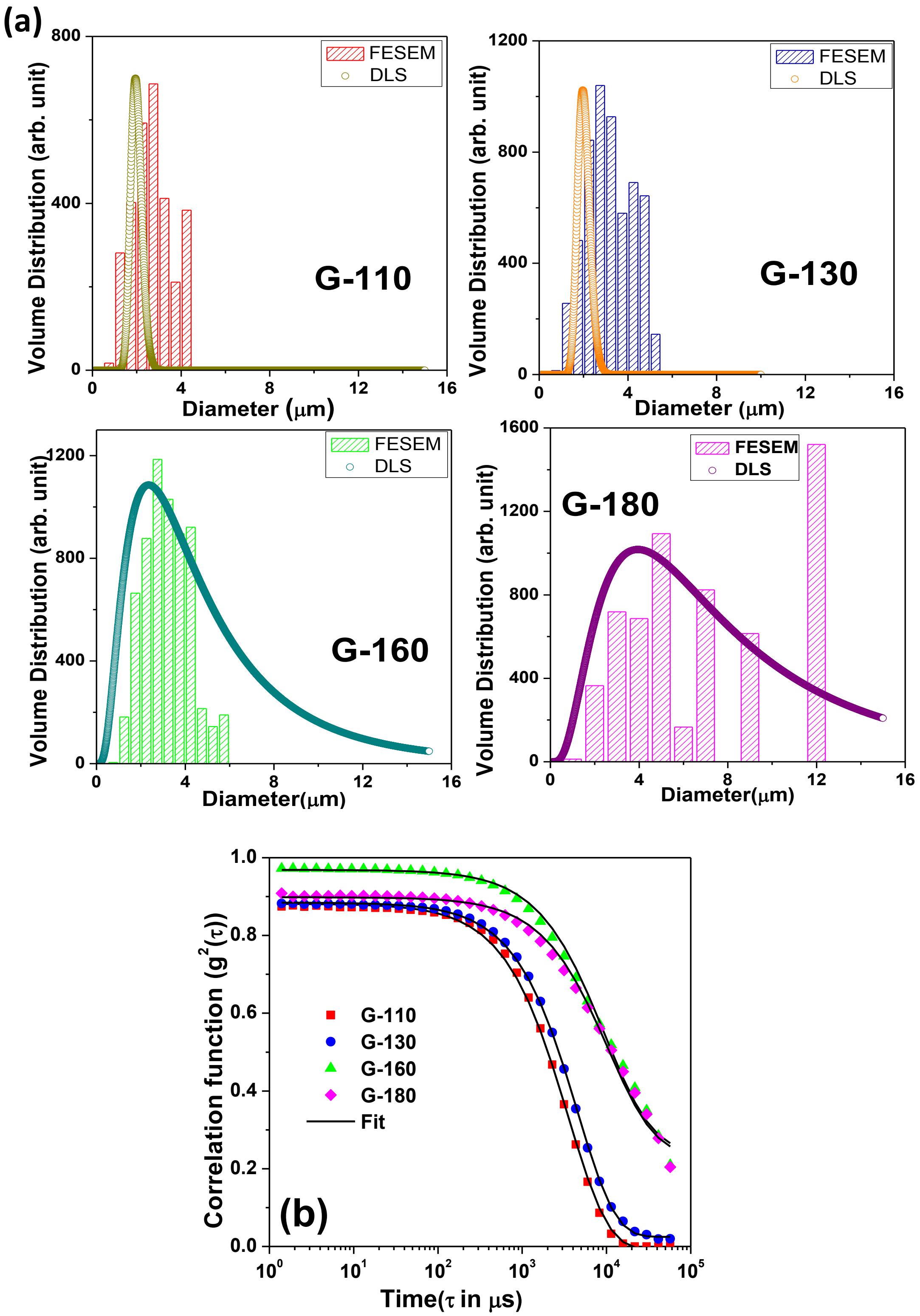

Fig. 3.2(a) Comparison of granular size distributions obtained from FESEM image analysis (histograms) and DLS. (b) Variation of $g_2(\tau)$ with correlation time (τ) for the granules dispersed in water. Error bars on the data points are nearly of the same size of the data symbols.

A theoretical estimate of the granular sizes was made by assuming isotropic drying of the droplets starting from the droplet size distribution, following the conservation of mass. Considering ϕ_d and ϕ_g to be the volume fraction of silica nanoparticles in the droplet and dried granules respectively, R_d and R_g to be the droplet and granule radii respectively, the conservation of mass yields,[103] $\phi_d R_d^3 = \phi_g R_g^3$. Thus, a size distribution corresponding to isotropic shrinkage can be generated from the initial droplet sizes (R_d). Fig. 3.3 compares the size distribution plots obtained from DLS with the theoretically generated plot obtained from the above equation. It is found that G-110 and G-130 have distributions close to that of the isotropically dried granules whereas distribution for G-160 and G-180 resembles the initial droplet. The reason for the granular sizes resembling the initial droplet sizes is due to the internal hollowness of the granules, as will be clear in the succeeding sections.

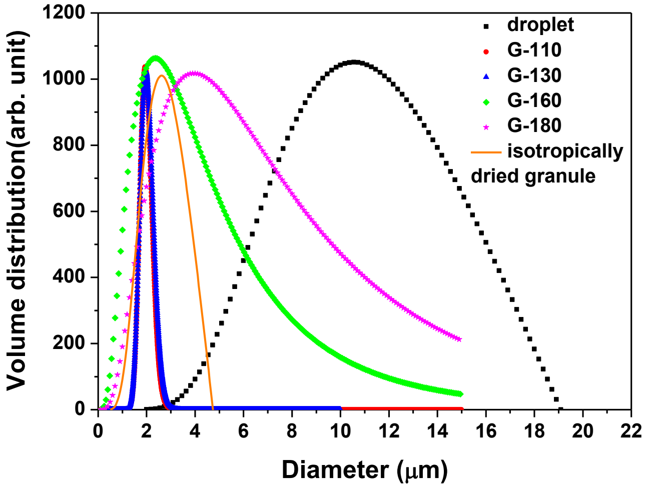

Fig. 3.3 Comparison of the granular size distributions obtained from DLS with the actual droplet size distribution and the theoretical distribution obtained by isotropic drying of the droplets.

3.1.3.2 Nanoparticle size distribution and correlation from SAS

As mentioned in the previous section, FESEM and DLS provide an estimate of the shape and polydispersity of the granules. SAS on the other hand quantifies the sizes and nanoparticle correlation in the granules. The knowledge about the type of interparticle correlation is important to account for the drastic granular size differences (for different drying temperatures) with respect to the same average droplet size. In the present case, for example, enlarged size can be either due to fractal-like aggregation[155] of the nanoparticles leading to non-consolidated branched structures or due to arrangement of particles at the droplet boundary forming a shell, ultimately resulting in a hollow granule.

As mentioned earlier, SAS was performed with both neutrons and X-ray as probes. Corresponding to the accessible length scales, the nanoparticle sizes and interparticle correlation were obtained from SAXS, whereas the larger granular structures were probed by SANS. Hence the total scattering contribution comprises of additive contributions from both of these length scales. The total scattering intensity $I_{total}(q)$ is given by,[164]

$$I_{total}(q) = I_g(q) + I_{np}(q) \tag{3.1}$$

where $I_g(q)$ is the contribution from the larger structures at lower q (from SANS) given by,

$I_g(q) = C_g \int_0^\infty P_g(q,r) D_g(r) V_g^2(r)\, dr$ whereas $I_{np}(q)$ is contributed by the correlated nanoparticles at the higher q (from SAXS) region given by,

$$I_{np}(q) = C_{np} \int_0^\infty P_{np}(q,r) D_{np}(r) V_{np}^2(r) S_{np}(q,r)\, dr$$

under local monodisperse approximation.[182] C_g and C_{np} are scale factors which depend on number density and scattering contrast of granules and nanoparticles, respectively, $v_x(r)$ is the corresponding volume of the scatterers in each case. $P_x(q,r)$ represents the form factor. For spherical nanoparticles,[164] $P_{np}(q,r) = 9\frac{\left[\sin(qr) - qr\cos(qr)\right]^2}{(qr)^6}$. $S_{np}(q,r)$ is the interparticle structure factor, which depends on the type of interaction among the silica nanoparticles. Size distribution function, $D_x(r)$ was chosen as a log-normal having the form given in Eq 2.21.

The fitting parameters, as obtained using non-linear square method are tabulated in Table 3.1. SAXS studies were carried out granules as well as for the dilute dispersions prior to spray drying. The scattering profile of the dilute dispersion is compared with those of the granules in Fig. 3.4. For dilute dispersion, the structure factor $S(q)$ can be assumed as unity. However, SAXS profiles for granules show a distinct correlation peak at $q\sim 0.25$ nm^{-1} which corresponds to an average interparticle distance of ~25 nm. The interparticle correlation was found to be of sticky hard sphere potential[192] with a fairly uniform stickiness coefficient as tabulated in Table 3.1.

Granules	**Volume fraction of nanoparticles (ϕ_g)**	**Radius of gyration (R_g in nm)**	**Specific surface area (S/V) (m^2/g)**
G-110	0.69±0.01	268±1	59±2
G-130	0.66±0.01	293±1	63±2
G-160	0.71±0.01	278±1	63±2
G-180	0.72±0.01	268±1	64±2

Table 3.1 Parameters obtained from model fitting of SAS profiles of granules.

The volume fraction was found to be ~0.7 denoting a fairly close-packed system. The polydispersity index of the nanoparticles is found to be ~0.13 with a median particle size of ~14 nm. From the inset of Fig. 3.4, it is seen that the position of the correlation peak (at $q\sim 0.25$ nm^{-1}) remains invariant denoting that the average inter-particle distance between the nanoparticles remained almost identical (~25 nm) for all types of granules, irrespective of the overall shape. However, the shapes of the profiles prior to the peak (in the range of 0.1 nm$^{-1} < q <$ 0.15 nm^{-1}) are distinguishable owing to the slight variations in the extent of local ordering (as also evident from zoomed FESEM micrographs on Fig. 3.1).

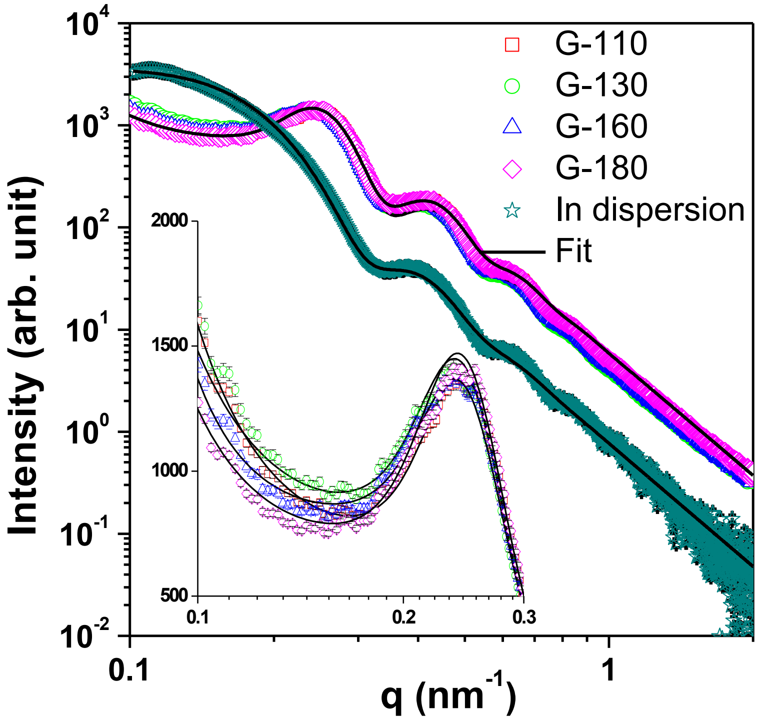

Fig. 3.4 SAXS profiles of the granules compared with that of initial colloid dispersion. **INSET**: Zoomed view of lower *q* region of the SAXS profiles. Error bars on SAXS data points are of the same size of the symbols.

MSANS profiles bear information about a larger length scale (*q* range of 0.003 to 0.2 nm^{-1}). Fig. 3.5(a) depicts the individual MSANS profiles for the granules whereas 3.5(c) depicts the consolidated SAS data over the whole accessible q-range, comprising of SAXS and MSANS. It should be noted here that MSANS profiles have been scaled after background correction to preserve the continuity of the SAXS profiles. The consolidated profiles were fitted with i) mass fractal,[193-194] ii) hard-sphere[182] and ii) sticky hard sphere models to determine the nature of interparticle correlation. A sticky hard sphere type of correlation perfectly mimics the scattering profile, unlike the fractal or hard-sphere models. Fig. 3.5 (b) compares the fit of the fractal (FM) and sticky hard sphere models (SHSM) to the complete SAS data for G-110, confirming the goodness of the latter over the former. Thus, the possibility of the granules synthesized at higher drying temperatures (G-160 and G-180), to be constituted of fractal-like aggregation was ruled out. Hence the largeness is attributed to their internal hollowness, as will be explained in the later sections.

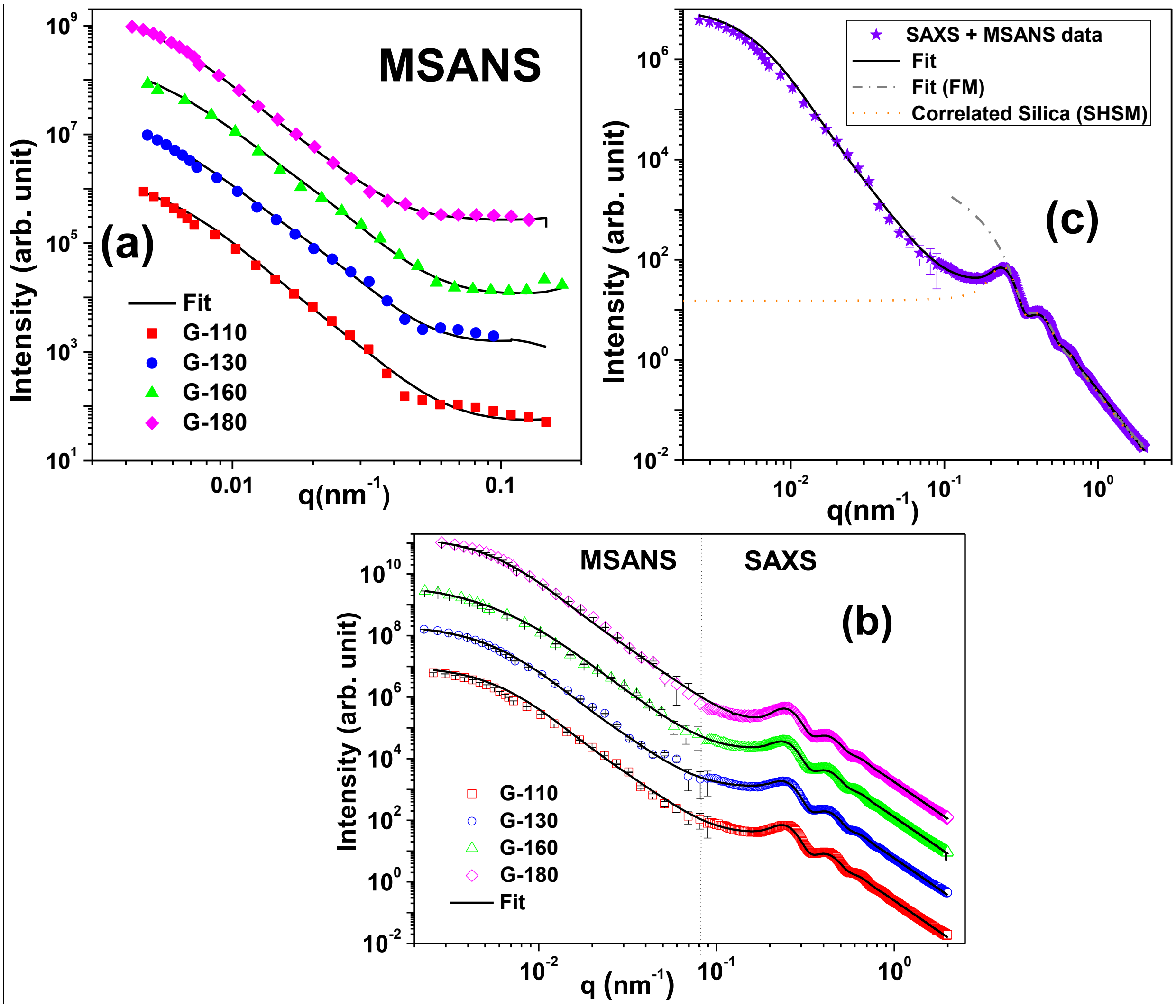

Fig. 3.5 (a) MSANS profiles, **(b)** Model fits to the combined SAS data. SHSM and FM represent sticky hard sphere potential and mass fractal types of models respectively. **(c)** Combined SAXS and MSANS profiles over the whole accessible q-range after proper scaling by normalizing MSANS data to SAXS data in the common *q* region. The profiles for each specimen are shifted vertically for clarity of presentation. Error bar on the SAXS data points is smaller than the size of the symbols.

An estimate of the radius of gyration (R_{gy})[163-164, 195] of the granules was made from scattering data at very low *q* or the Guinier region obtained from the MSANS profile where the intensity is given by,

$$I\left(q\right) = I_0 \exp^{-\frac{q^2 R_{gy}^2}{3}} \tag{3.2}$$

The slope of the plot (Fig. 3.6(a)) log [$I(q)$] vs. q^2 yields the effective radius of gyration of the granules (listed in Table 3.1). The specific surface area[164] of the granules (Table 3.1) was obtained by,

$$\frac{S}{V_P} = \frac{\phi_g(1-\phi_g)\pi}{d_{silica}} \cdot \frac{\lim\limits_{q\to\infty} I(q)q^4}{\int I(q)q^2dq} \tag{3.3}$$

where ϕ_g is the nanoparticle volume fraction in a micro-granule and can be estimated from SAXS analysis. The limiting value of $I(q)q^4$ is obtained from Porod plots given in Fig. 3.6(b). It is seen that there are two distinct Porod regions, corresponding to the two length scales in the granules, namely, overall granules and the individual nanoparticle.

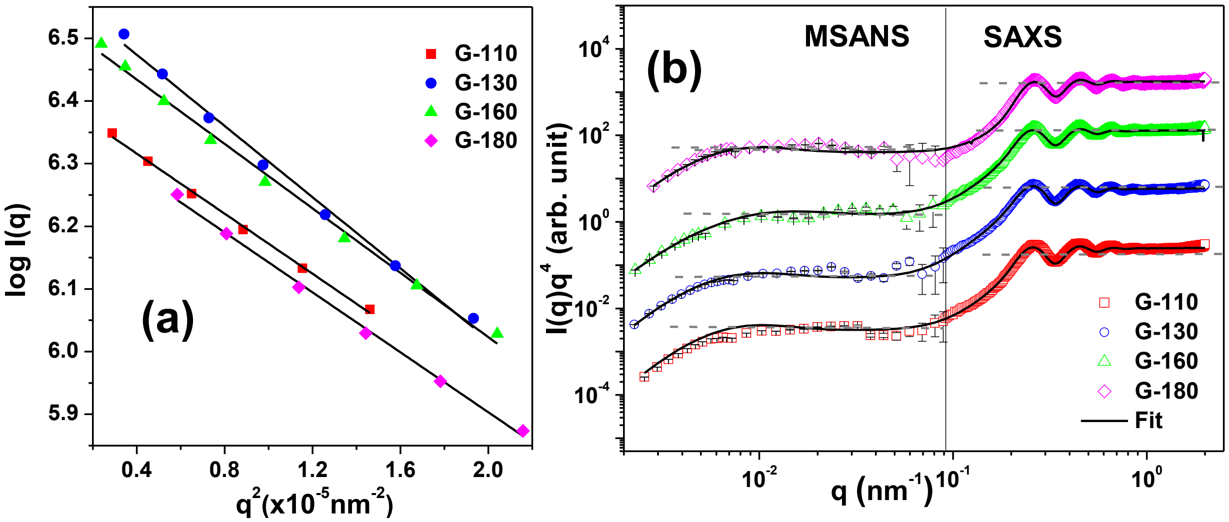

Fig. 3.6 (a) Guinier plots (log(I) vs. q2) from MSANS data. The radius of gyration is calculated from the slope of these profiles. **(b)** Porod plots of the combined MSANS-SAXS data. Gray dotted lines depict the two distinct Porod regions for each of the profiles.

The obtained R_g values are typically 300 nm from MSANS data. However, it is discernable from FESEM micrographs that the granules are micrometric in size. In order to quantify the overall size and shell thickness/hollowness, a relatively newer technique known as spin-echo SANS or SESANS have been utilized (details are given in the following section). Thus, a combination of imaging and scattering techniques should be implemented complementarily for the complete structural characterization of the granules.

3.1.3.3 Hollowness from Spin-Echo Small-angle Neutron Scattering (SESANS)

In the previous section, it has been described that SAS (both SAXS and MSANS) jointly provided information of the nanoparticle sizes, the interparticle spacing and the type of correlation. This section discusses the investigation of the whole granular sizes and quantification of the granular hollowness, using the spin-echo small-angle neutron scattering (SESANS) technique.[196-199] It is to be recalled that in SAS, one obtains data in the range of few tens of nanometres up to several hundred nanometres as a function of the momentum transfer (q) which is related to the scattering angle.[167] In SESANS the depolarization of a polarized neutron beam is measured as a function of the 'spin-echo length' which is a real space parameter.[200] It has more flexibility than SAS as it allows high-resolution investigations even of the order of 10μm, bypassing the need of extensive collimation.[201]

Fig. 3.7 gives an idea of the length scale brackets probed by the techniques used in the structural characterization of the nano-structured micro-granules in this thesis. SAXS covers a range from 3 to 60 nm whereas MSANS covers a range from 40 nm to 2 μm. Microscopy covers the larger length scale (>10 μm). SESANS, on the other hand, spans from few nanometres up to 20 μm, efficiently bridging the gap between SAS and microscopy.

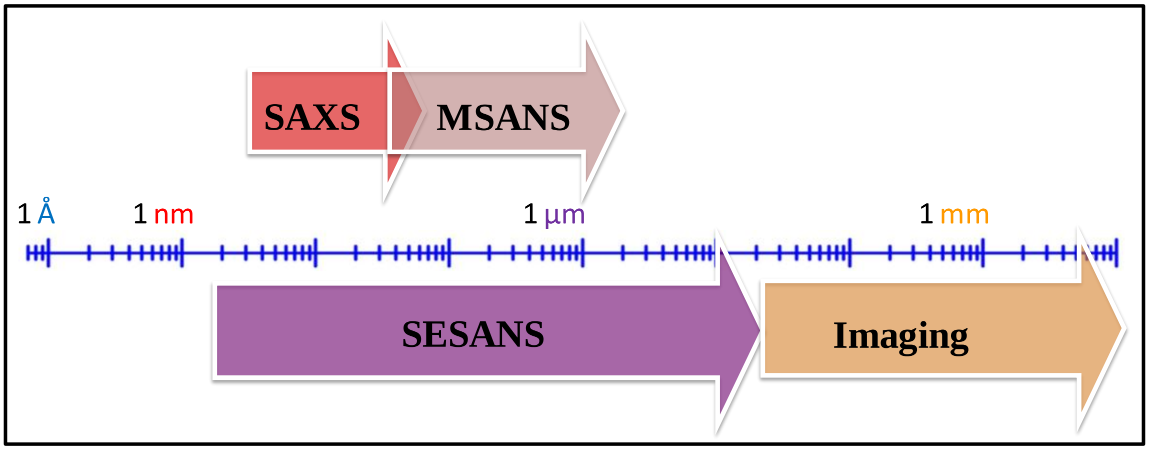

Fig. 3.7 Schematic representation of the different characterization techniques used for accessing the typical length scales of nano-structured micro-granules.

As the name suggests, SESANS uses the principle of spin-echo to measure scattering events. Neutron is a spin-half particle, thus it undergoes Larmor precessional motion in magnetic fields.[202] SESANS technique utilizes this property to measure energy transfers during scattering. In general, SESANS approach relates the polarization $P(z)$ of the neutron beam to the projection $G(z)$ of the auto-correlation function ($\gamma(r)$) of the density distribution ($\rho(r)$) in the sample.[203-204] $P(z)$ is measured as a function of the real-space distance over which correlations are measured in the sample or the spin-echo length (z). Applications of this technique for the study of colloids have been reported by Krouglov *et al.*[205] and Bouwman *et al.*[206]

In the present case, experiments were carried out at the SESANS instrument at the reactor at TU Delft, Netherlands. This setup uses a monochromatic beam and enables the study of structures in the range 5 nm–20 μm.[203] The basic principle is sketched in Fig. 3.8.

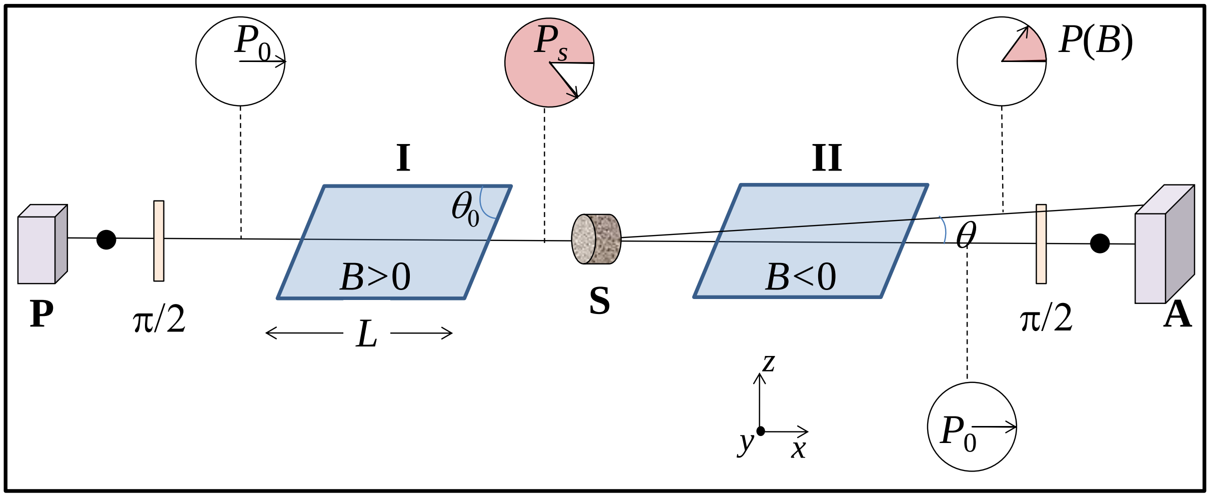

Fig. 3.8 Schematic representation of the SESANS principle. Polarized neutron beam from source (P) on the left side is incident on the first π/2 rotator. Its polarization is rotated over by π/2 to the (x, z) precession plane. Then the polarization precesses in the regions I and II in opposite directions due to the opposite field (*B*) directions. After another rotation by π/2, the neutrons reach the analyzer A and are detected. The precession angle in regions I (φ_I) and II (φ_{II}) are strongly dependent on the incident angle of the neutron. In the absence of a scatterer S, φ_I and φ_{II} cancel each other, whereas, scattering over any angle disturbs the echo, which can be measured and analyzed in terms of depolarization of the neutrons.

The spin-echo setup consists of two precession devices with equal and oppositely oriented magnetic fields (*B*) that effectively cancel the precession angles (φ) of the neutron spins, when there is no sample at the path of the incident neutron direction. The precession devices are mounted between two π/2 rotators to rotate the polarization direction back to the precession plane from the initial polarizing direction. Now when a sample is placed between the two devices, scattering occurs and the net precession angle is non-zero.[201] The rotations along different paths are indicated at the top of Fig. 3.8. The precession angle φ_I ,in device I is found from the geometry to be, $\varphi_I = c\lambda BL \dfrac{\sin\theta_0}{\sin(\theta_0+\theta)} \cong c\lambda BL(1+\theta\cot\theta_0)$ where *c* is the Larmor precession constant (4.63 x 10^{14} $T^{-1}m^{-2}$), *B* is the magnetic field over length *L*, λ is the wavelength, θ_0 is the angle between the inclined precession faces and the *x*-axis, θ is the transmission angle with *x*-axis. The difference in the neutron spin precession after crossing two devices (placed on either side of the sample) with opposite precessions is $\varphi_I - \varphi_{II} = \varphi \simeq c\lambda BL\theta_s \left\langle \cot\left(\theta_0\right) \right\rangle_\alpha \equiv Zq_z$ where cot(θ_0) is averaged over the divergence α of the neutron beam in the *z*-direction, θ_s is the scattering angle. This difference is defined as the product of the wave vector transfer q_z of the neutron and the spin-echo length *Z*. Spin-echo length is an instrumental quantity that describes the distance at which *Z* correlations in the sample are probed. *Z* is given by $Z = c\lambda^2 BL \frac{\left\langle \cot\left(\theta_0\right) \right\rangle_\alpha}{2\pi}$ and $q_z = \frac{2\pi\theta_s}{\lambda}$. The incident neutron beam has polarization P_0 in the *z*-direction, $P_z(Z)$ is the *z*-component of the polarization vector of the scattered neutron, given by $\frac{P_z(Z)}{P_0} = \cos(\varphi) = \cos(Zq_z)$. For scattering over the total solid angle covered by the detector, weighted averaging over all scattering angles yields the normalized polarization $P(Z) = \frac{P_z(Z)}{P_0} = \frac{\int I(q_z)\cos(Zq_z)\,d\Omega}{\int I(q_z)\,d\Omega}$ where $I(q_z)$ is the intensity of scattered neutrons with wave vector component q_z. The polarization *P*(*Z*) is related to *G*(*Z*), the projection of the auto-correlation function of the density distribution in the sample by, $P(Z) = e^{-s_t\{1-G(Z)\}}$ where s_t is the total sample thickness.

The obtained polarization profiles, *P*(*Z*) vs *Z* for the granules are given in Fig. 3.9(a). A shift of the profiles towards larger spin-echo lengths are observed for hollow granules (G-160, G-180) denoting their larger sizes.[207] The generated *G*(*Z*)-*G*(0) plots are given in Fig. 3.9(b). The plots are fitted with *G*(*Z*) corresponding to spherical shells,[207] considering a tri-log-normal type (Eq. 2.21) of granular size distribution. The corresponding fitting parameters are given in Table 3.2. The granular sizes and polydispersities were found to increase with the increase in their drying temperatures, corroborating with the finds from DLS (Fig. 3.3). The volume size distributions are plotted in Fig. 3.9(c). The hollowness increases owing to the corresponding decrease in shell thicknesses of the granules (Table 3.2). The reason for such behaviour is because of its assembly process, which is elaborated in the next section.

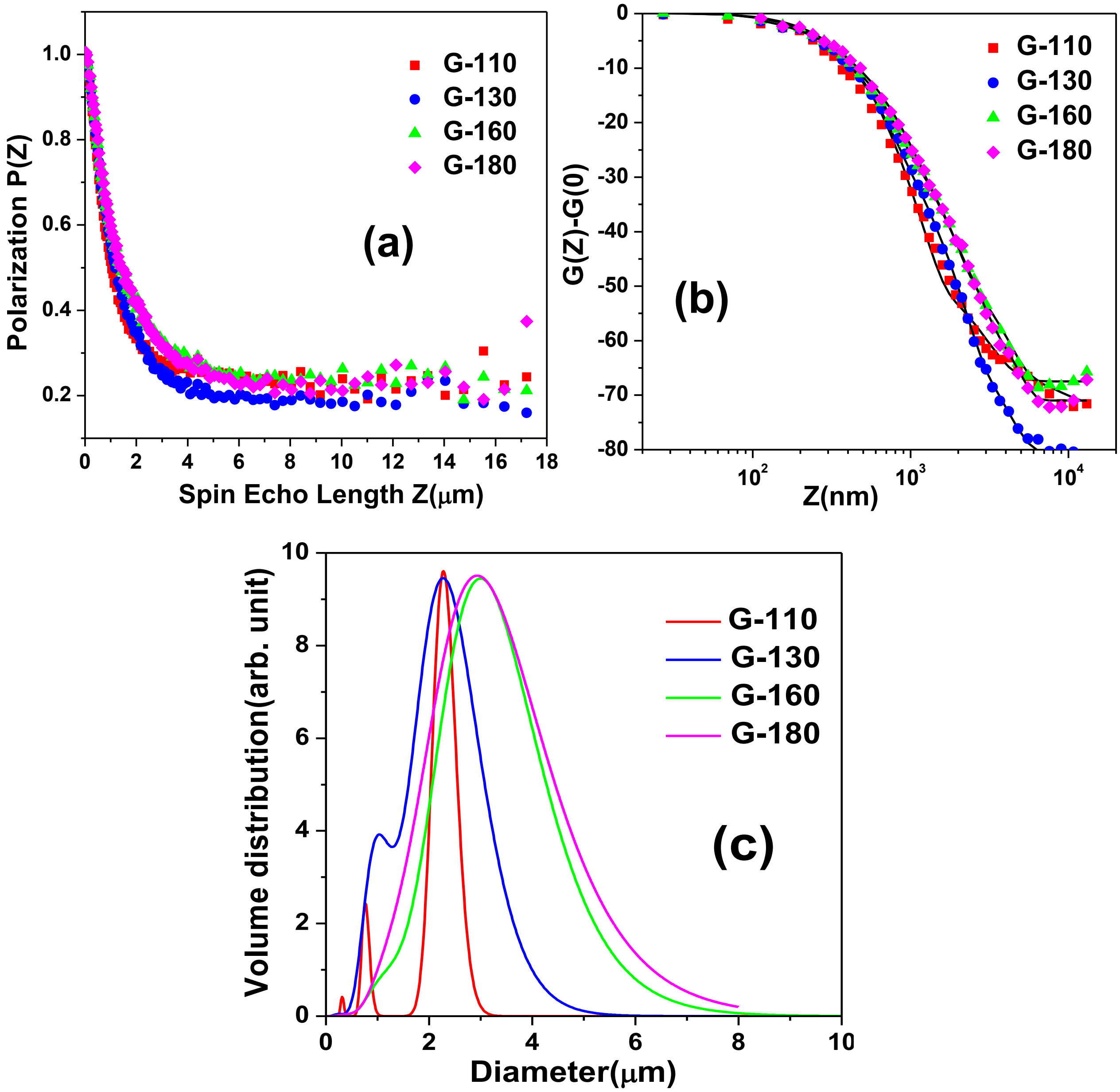

Fig. 3.9 (a) Variation of polarization with spin echo length. **(b)** Variation of normalized G(Z) vs Z profiles **(c)** Granular volume distribution as obtained from SESANS.

Sample	**Average radius (μm)**		**% hollowness**	**Polydispersity index**
	Outer R_{out}	**Inner R_{in}**		
G-110	1.09	0.11	10.0	0.1
G-130	1.15	0.23	20.0	0.2
G-160	1.69	0.48	28.4	0.3
G-180	1.71	0.68	39.8	0.4

Table 3.2 Parameters obtained from model fitting of the SESANS profiles.

Thus, SESANS, along with electron microscopy and SAS (MSANS and SAXS) complement each other to provide the complete structural characterization of the micro-granules.

3.1.3.4 Strength of drying and nanoparticle assembly process

As mentioned in Chapter 2.1, the quantitative measure of the strength of drying is given by the Peclet number P_e.[149-103] In short, it is the ratio of the mixing time, τ_{mix} of the nano-particles in the droplet to its drying time τ_d (Eq. 2.3). The shrinkage in the size of the droplet, due to diffusion limited evaporation is given by Eq. 2.1.[126] The drying time for an isolated droplet, τ_d was calculated from Eq. 2.1 and is given in Table 3.3 with an assumption that p_∞ is zero (disregarding the presence of other droplets in the surroundings). The ratio of maximum (for a drying temperature of 110°C) to the minimum (for 180°C) drying time is estimated to be nearly 6. Here, it should be noted that drying time in reality, will be much larger due to the presence of surrounding droplets in the drying chamber, making p_∞ non-zero. However, the above-mentioned simplified calculation gives an idea about the trend of the variation of the drying time with temperature. The Peclet number in each case was calculated from Eq. 2.1 using the obtained τ_d values and tabulated in Table 3.3, P_e was found to be greater than unity which suggests that drying occurs via shell formation (of the nanoparticles) at the air-water interface. P_e exhibits an increasing trend with drying temperature. This is due to the faster drying at higher temperatures leading to earlier shell formation than in the case of drying at low temperatures. The shell absorbs heat, creating a temperature difference across the droplet core and the silica shell. Such temperature gradient initiates a directional motion of the particles in the droplet commonly known as thermophoresis or the Ludwig-Soret effect.[208-209] Thus, under the non-isotropic drying scenario, shell formation and thermophoresis occur chronologically.

Sample	**Estimated drying time τ_d (ms)**	**Peclet Number**	**Soret Coefficient S_T (K^{-1})**	**$S_T\delta T$**	**$(dR_d/dt)_B$ (m/s)**
G-110	2.19 ± 0.05	52.2 ± 1.5	-0.0520 ± 0.0001	-3.64±0.04	$0.30(\pm 0.04)\text{x}10^{-12}$
G-130	1.23 ± 0.03	74.2 ± 1.7	-0.0510 ± 0.0001	-4.59±0.05	$0.60(\pm 0.04)\text{x}10^{-7}$
G-160	0.59 ±0.01	120.0 ± 1.9	-0.0480 ± 0.0001	-5.76±0.05	$1.00(\pm 0.03)\text{x}10^{-6}$
G-180	0.38 ± 0.01	157.1 ± 2.5	-0.0470 ± 0.0001	-6.58±0.06	$0.30(\pm 0.02)\text{x}10^{-5}$

Table 3.3. Calculated values of different physicochemical parameters.

The diffusive particle current-density (J) may be approximated to be composed of two parts: i) mass diffusion and ii) thermal diffusion. Thus,

$$J = J_{mass} + J_{thermal} = -D_M \nabla n - nD_T \nabla T = -D_M(\nabla n + nS_T \nabla T) \qquad (3.4)$$

where D_M and D_T are mass and thermal diffusion coefficients, respectively. S_T is the Soret coefficient. ∇n and ∇T represent the gradient in number density and temperature respectively. At steady state, *i.e.,* for J=0, integrating the above equation between n_s (concentration at the shell) and n_c (concentration at the core), we get

$$n_s = n_c e^{-S_T \delta T} \qquad (3.5)$$

where δT is the temperature difference between shell and core of the droplet. Thus, the product $S_T\delta T$ decides the depletion behaviour of the particles in the drying drop. Rusconi[210] and Ning *et al.*[211] have reported that S_T for silica nanoparticles is negative. Hence the exponent on the right-hand side of Eq. 3.5 is positive, implying that $n_s >> n_c$ i.e., higher particle concentration at the shell than at the core. Therefore silica nanoparticles tend to migrate from colder (centre of the droplet) to hotter region (shell). Such motion is termed as thermophilic. The temperature dependent S_T values, tabulated in Table 3.3 were obtained from the fit of Eq. 10 as given in Ning *et al.*[211] The value of δT in each case has been calculated considering the core temperature of the droplet as 40°C. The variation of Soret Coefficient (S_T) and Thermal Diffusion Factor ($S_T\delta T$) with temperature is shown in Fig. 3.10.

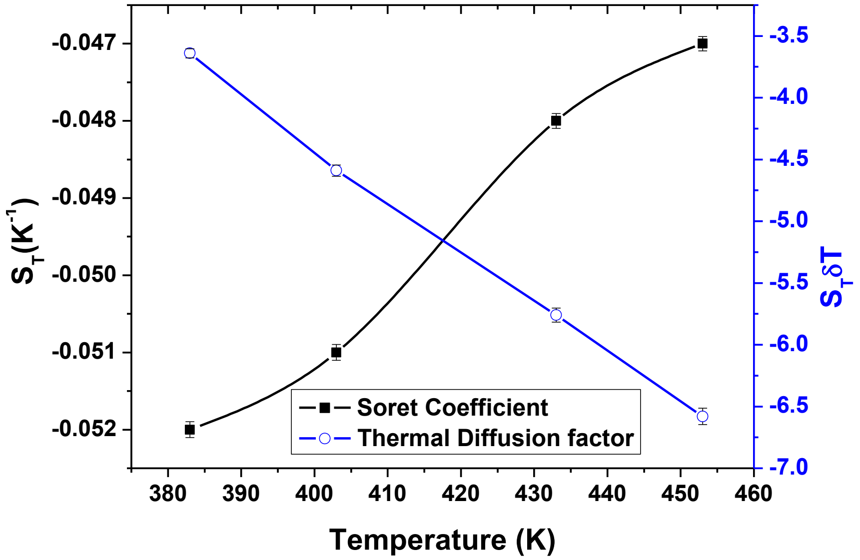

Fig. 3.10 Variation of Soret Coefficient (S_T) and Thermal Diffusion factor ($S_T\delta T$) with temperature.

It is seen that $S_T\delta T$ increases steadily with the increase in drying temperature. Hence by Eq. 3.5, the number density at the boundary (or the shell), n_s increases with increasing δT consequently making the core depleted of nanoparticles. Thus, after the shell formation, its thickening depends on how quick thermophoresis occurs depending on the temperature gradient. The final thickness of the shell will be limited by the buckling point as will be discussed below.

As mentioned in Chapter 2.1, shell formation is often followed by buckling under Darcy stress[155] build-up due to liquid flow across the porous shell. At the time of buckling, the buckling force due to Darcy stress is written as,[151]

$$\Delta F_B = \pi a^2 \Delta P_B \tag{3.6}$$

where ΔP_B is the pressure drop across the shell at the time of buckling and a is the silica nanoparticle radius (~14 nm). This force is, in fact, equal to the attractive DLVO force between the nanoparticles,

$$|F_{DLVO}| = \frac{A_H}{48a} \tag{3.7}$$

where 'A_H' is the Hamaker constant, typically ~0.85x10^{-20} J for silica.[212] Equating above two equations, we get $\Delta P_B = \frac{A_H}{48\pi a^3}$ which approximates to 21.5Pa in the present case. The Darcy pressure is written as,[213]

$$\Delta P_{Darcy} = \frac{\eta T_{Shell}(t)}{K}\frac{dR_d}{dt} \tag{3.8}$$

At the onset of buckling, ΔP_{Darcy} is replaced by ΔP_B and the rate of change of radius becomes $\left(\frac{dR_d}{dt}\right)_B$. K is calculated to be ~ 4x10^{-19}m^2 from Eq. 2.5 considering ϕ_{np} to be equivalent to volume fractions of nanoparticles as obtained from SAS profiles. The buckling time is given by,[155] $t_{Buckling} = \frac{\Delta P_B K}{\eta \frac{\phi_d}{\phi_{shell} - \phi_d}\left(\frac{dR_d}{dt}\right)_B^2}$ where ϕ_d is the silica volume fraction in the droplet. The thickness of the shell (T_{shell})at any given time t is,

$$T_{Shell}(t) = \frac{\phi_d}{\phi_{shell} - \phi_d}\left(\frac{dR_d}{dt}\right)t\,. \tag{3.9}$$

Using Eqs. 3.8 and 3.9, the temporal variation of ΔP_{Darcy} was plotted. Fig. 3.11(a) shows that the time required to attain the critical buckling pressure (ΔP_B =21.5 Pa) is the quickest at 180^{o}C and slowest at 110^{o}C. When compared with the approximate maximum drying time (~1 second, as calculated from the geometry of the drying chamber and the aspiration rate), it is seen that at 180^{o}C, the granule buckles much before it dries. Thus, due to lack of sufficient time before complete drying, the shell formed in this case is thinner. Such thin shells are more prone to buckling and hence, granules possess dented surfaces. Depending on the strength of buckling, the dent propagates and the granule eventually becomes a toroid. At lower drying temperatures (110^{o}C and 130^{o}C), $t_{buckling} >> t_{drying}$ allowing the shell to thicken considerably before drying thereby inhibiting buckling. Fig. 3.11(b) shows the relative buckling time for the different granules. The rates of radial decrease in each case are tabulated in Table 3.3.

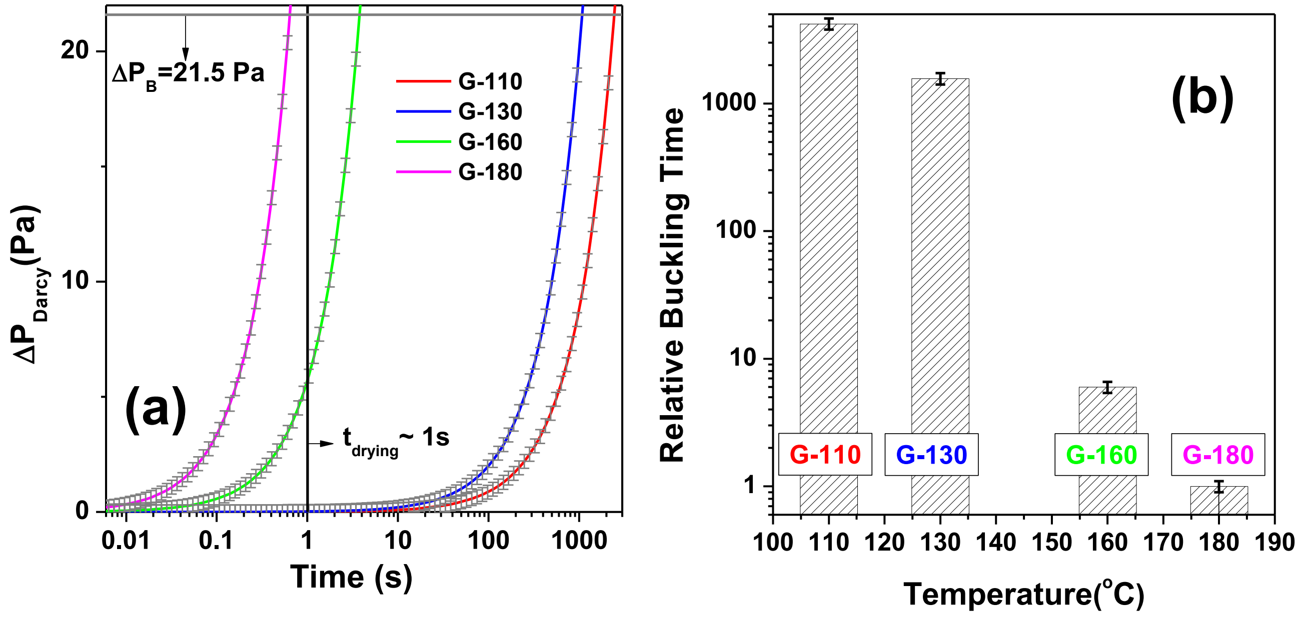

Fig. 3.11 (a) Variation of the Darcy pressure with time. t_{drying} marks the real drying time under experimental conditions. ΔP_B signifies the Darcy pressure at the time of buckling. **(b)** Comparison of buckling time ($t_{buckling}$) for the granules at different drying temperature.

3.1.3.5 Simulation of morphological transformation by Surface Evolver

The morphological transformation from sphere to toroid with the increase in the rate of drying is illustrated by simulation using Surface Evolver.[189] In short, the transformation process is based on earlier works by Quilliet *et al.*,[214] and Sen *et al*.,[54] which works on the principle of minimization of surface energy. Stretch and curvature energies are applied to a simulated spherical shell (which is initially generated from a regular cubic polyhedron) and the volume is decreased by keeping the area constant. The rate of decrease of volume is a measure of drying rate or the drying time. The ratio (γ) of stretching to bending energy is a direct measure of the extent of buckling and is known as Foppl-Von-Karman number.[215] γ is also related to the relative shell thickness $\left(T_{Shell}/R_g\right)$ by $\gamma = 12\frac{\left(1-\nu^2\right)}{\left(T_{Shell}/R_g\right)^2}$ where ν is the Poisson ratio (ratio of the transverse strain to the axial strain for a body under applied load). The target volume (V) and the rate of volume decrease have been varied to simulate the situations at different drying rates keeping Poisson ratio (for silica) fixed at ~0.33.[54] The computer simulated images are depicted in Fig. 3.12. The spherical shape is realized when the rate of decrease in each iteration remained slow (~$0.001V_0$; V_0 being the initial volume of the simulated regular cube). The rate was slowly increased to $0.03V_0$ that resulted in doughnut-like structures. In all of these cases, the γ optimized and kept fixed at 20. It is evident that the simulation results corroborate quite well with the experimental micrographs of the granules.

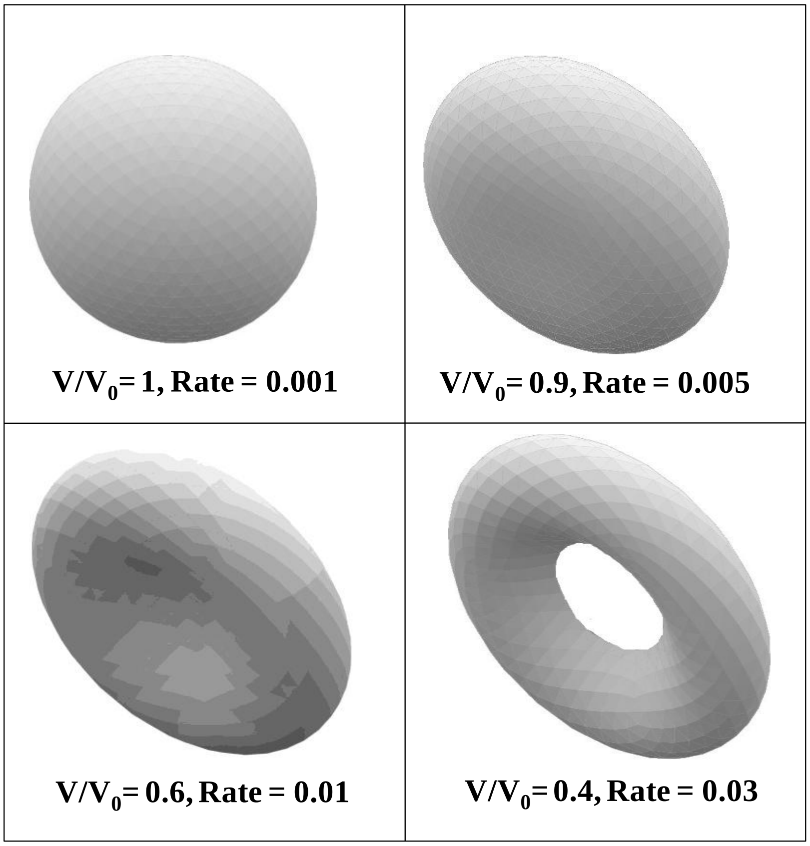

Fig. 3.12 Granular morphologies simulated using Surface Evolver. The rate is denoted by units of volume decrease per iteration.

3.1.3.6 Porosity of granules

The granules are composed of interlocked nanoparticles which enclose interstitial voids or pores. For a system of close-packed uniformly sized N number of spherical particles, there are 8N trigonal voids, 2N tetrahedral voids and N octahedral voids and the packing fraction is 74%. Further, the ratio of size of void to that of a particle is 0.155, 0.225 and 0.414 for trigonal, tetragonal and octahedral voids, respectively.[216] In the present case, the volume fraction is ~0.7 or 70%, as obtained from SAS. Therefore these nanoparticles enclose hierarchical pore sizes. Moreover granules synthesized at high drying temperatures possess significant hollowness which contributes to the pore structure as well. Formerly, it has been described that SAS quantified the specific surface area of these granules. The porosity of the granules can also be quantified with the help of gas adsorption technique, also known as Brunauer–Emmett–Teller (BET).[217]

BET experiments have been performed for all the samples using Surface Area Analyser (Model: Surfer), Thermofisher Scientific (Italy). Sample weight taken was nearly ~200 mg. Nitrogen at -196^{o}C was used as the adsorbing gas. The monolayer thickness is 0.354 nm and the molecular area of the gas is 0.162 nm^2. The results from BET are provided in Fig. 3.13. BET plots are linear for the range 0.02 - 0.4 P/P_0 (Fig. 3.13(a)). W represents the weight of the gas adsorbed at relative pressure P/P_0. The C values are given in Table 3.4 with a correlation coefficient of 0.99. High C values (>200) for G-130 and G-180 can be contributed to the large-sized pores. Differential pore volumes are plotted (Fig. 3.13(b)) against pore radius which reveal a peak around a mean radius at ~1 nm for G-110, which increases further for G-130 and G-180. G-160 possesses the highest peak at ~2.2 nm. Cumulative mesopore volume is highest for G-160 denoting more surface pores than other granules (Fig. 3.13(c)). This result is corroborated by the mono-layer volume which is also highest for G-160 (Table 3.4). The cumulative pore volume, average mesopore radius and specific surface area as obtained from BET are tabulated in Table 3.4. The adsorption isotherms (Fig. 3.13(d)) show a distinct adsorption and desorption branches, enclosing a hysteresis area. Hystereses can be contributed to various reasons such as capillary condensation of the sorbed gas in the pores, meta-stability of adsorbed multilayer due to delayed condensation in open-ended pores, or network of wider pores which have access to the outer surface by narrow necks (ink-bottle pore shapes).[218-219] The hysteresis loops near P/P_0~1 are not flat; rather have an increasing trend, denoting presence of macropores along with mesopores in the granules. The obtained specific surface areas (Table 3.4) from BET reveal the highest value for G-160.

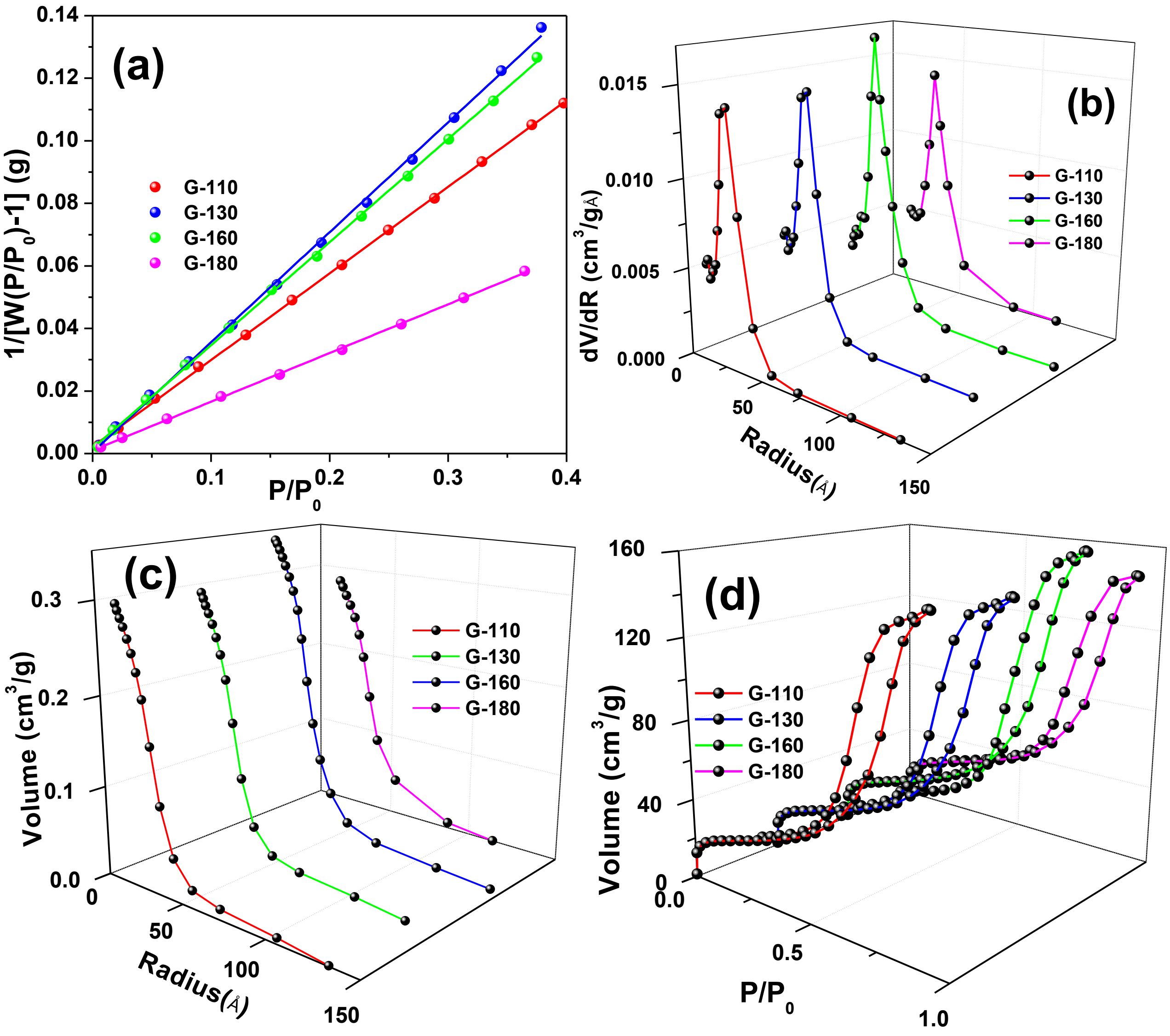

Fig. 3.13 (a) BET plots, **(b)** Differential mesopore volume distribution, **(c)** Cumulative mesopore volume distribution for granules, **(d)** Adsorption-desorption isotherms for the granules.

Granules	***C* value**	**Monolayer volume (cm^3/g)**	**Cumulative pore volume (cm^3/g)**	**Average pore radius (nm)**	**Specific Surface Area (m^2/g)**
G-110	98.1	22.3	0.29	3.3	97
G-130	267.5	21.6	0.31	3.6	94
G-160	125.5	23.2	0.34	3.5	101
G-180	255.3	20.9	0.28	3.0	91

Table 3.4 Obtained experimental values from BET.

3.1.3.7 Behaviour of trapped water in the nanometric pores

Trapped water displays unique traits approaching the freezing or boiling temperature, which is not displayed by bulk water.[220] Confinement in pores has a huge influence on the solid/liquid phase transitions. Such behaviour of water is relevant in various fields of science and technology such as geological profiling, soil chemistry, activity of water in living cells, food preservation, etc. In the present case, the nano-structured silica micro-granules possess hierarchical pore structures which allow the investigation of the effect of confinement of water in these granules. It has been demonstrated with the help of differential scanning calorimetry (DSC) that water in a nanoporous silica matrix can be cooled to temperatures much below its freezing point (up to 50^o lower).

DSC technique monitors the thermal changes occurring in a system during heating and cooling cycles, as a function of temperature.[221] The heat flow is measured and plotted against the temperature of furnace or time. The deviation observed above the baseline corresponds to an exothermic process and that below corresponds to endothermic processes. The area under the peak is proportional to the heat evolved or absorbed by the reaction whereas the height of the peak is proportional to the rate of reaction. Experiments were carried out with Mettler-Toledo Differential Scanning Calorimeter (DSC) for ~20 mg of powder each at a heating/cooling rate of $\sim 5^o$ per minute. Samples were studied for heating and cooling cycles starting by cooling below room temperature till -80^oC. Heat curve on heating process was monitored up to 200^oC.

Fig. 3.14 shows the heating and cooling graphs. The positive peaks denote exothermic process, i.e. release of heat, whereas negative peak denotes endothermic process, which absorbs heat. In the cooling cycle (room temperature, 25^oC to -80^oC) there is an exothermic peak around -46^oC for each of the granules sets. It corresponds to the freezing of the pore water, as it occurs at a temperature lower than the 0°C. It is to be noted that the peak is fairly sharp, denoting that freezing starts at -43°C and peaking at -46°C which depicts that the pores do not possess uniformity. It is also observed that at the cooling cycle of confined water, there a 2nd peak develops alongside a primary peak at ~47°C the development of this alien peak is as a result of partially filled pores.

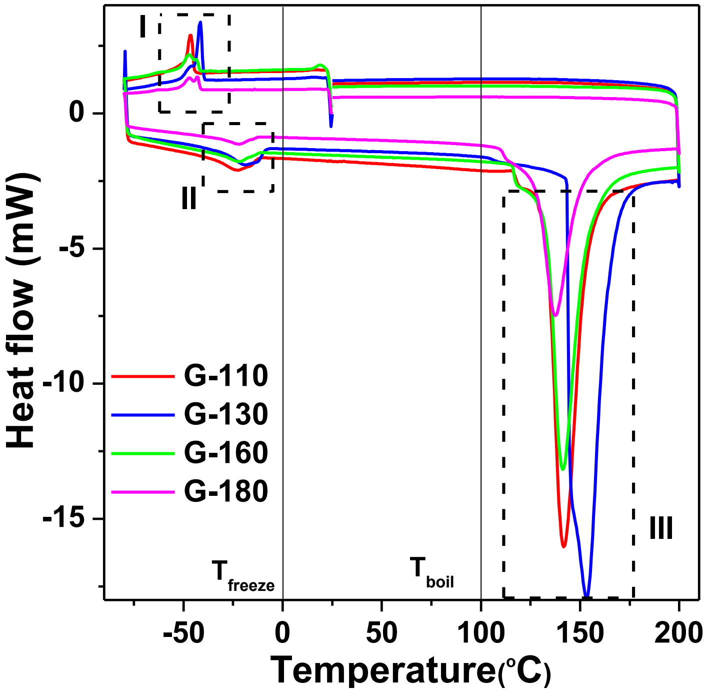

Fig. 3.14 DSC plots for the powder granules with dashed boxes depicting the change from bulk water behaviour. Regions **I**, **II** and **III** depicting the freezing, melting and boiling of trapped water in pores. T_{freeze} and T_{boil} denote the freezing and boiling temperature of bulk water.

3.1.4 Conclusions

This chapter demonstrates the evaporation-induced self-assembly of a virgin colloidal dispersion. The morphology of nano-structured micro-granules can be tuned simply by controlling the drying temperature during spray-drying process. Granules formed at lower temperatures are fairly monodisperse and spherical. Large, polydispersed hollow granules are obtained at higher drying temperatures with nanoparticles packed as a shell. The spatial distribution of the nanoparticles, either in bulk or as a shell depends on the thermophoretic motion of the nanoparticles in drying droplet under a temperature gradient. The formed shell is prone to buckling, depending on its thickness. Buckling results in toroidal morphology of the granules. The evolution of granule shape was modelled with the help of Surface Evolver simulations which is based on buckling of the elastic shell taking into consideration the rate of drying. Statistically averaged local volume fraction of the packed nanoparticles, as obtained from SAXS, remained nearly unchanged even though the external morphology changed significantly from sphere to toroid (as perceived from FESEM). SAS experiments further reveal a sticky-hard sphere type of correlation between the nanoparticles, irrespective of the overall granular shape. The large sizes of the granules are attributed to the existence of an internal hollow core which was characterized by SESANS technique. Granules synthesized at higher temperature are hollower than those at lower temperatures. The porosity analysis was carried out using gas adsorption technique of BET which yielded a specific surface area of ~100 m^2/g. The melting and boiling points of water show significant deviation from that of bulk water denoting the effect of confinement of water in the granular nano-pores.

Chapter 3.2: Morphology-dependent dye sorption by silica micro-granules

3.2.1 Preamble

As described in section 3.1.3.6, the micro-granules are porous in nature. This is due to nanoparticle-interstices and hollowness of the granules. From the utility point of view, such porous granules possess immense potential for various applications, such as catalysis,[222] molecular sieving,[223] ion exchange,[224] drug delivery,[225] etc. In this chapter, the dye sorption capability of the granules and its dependence on the morphology has been discussed for nano-structured silica micro-granules.[226]

Silica nanoparticles are negatively charged in an aqueous medium owing to the electronegative silanol groups on their surface. Such functionality allows attractive interactions with various cationic chemical species.[227-229] Thus, utilizing this advantage, the sorption capabilities of silica micro-granules for a cationic dye, Methylene Blue (MB) was investigated. These granules, being larger in size than nanoparticle units, settle faster after sorption allowing the easy decantation of supernatant. It is worth mentioning that MB is widely used in various industrial processes such as printing, dyeing of cotton and leather. It is also an efficient redox indicator and it have medicinal uses at low concentration.[230] However, at large concentration; MB is a toxic waste material.[231] Being water soluble, MB is very difficult to remove during industrial discharge into the environment. In this chapter, a low-cost and effective approach of removal of MB from water by nano-structured silica micro-granules has been demonstrated.

In the present case, the correlated silica nanoparticles in the micro-granules have an effective radius of ~14 nm as obtained from SAS (section 3.1.3.2). The equivalent radii of trigonal, tetragonal and octahedral interstitial voids in the granules are 2.2 nm, 3.2 nm and 6.0 nm, respectively.[216] A MB molecule has spatial dimensions (1.4nm x 0.6nm x 0.4nm).[232] Thus, the largest dimension of MB molecule is significantly less than the interstices. Therefore, MB can easily seep into the granules through the pores, thereby rendering nano-structured silica micro-granules as efficient sorbents. The sorption behaviour has been monitored with the help of Ultraviolet-Visible (UV-Vis) spectroscopy technique.

3.2.2 Spectral analysis by UV-Vis spectroscopy

Sorption of dye molecules by the synthesized granules was monitored by absorbance spectral analysis using JASCO V-650 UV-Vis spectrophotometer.[233] Blank measurement was performed using distilled water, followed by absorbance measurements for 50 ppm MB dye solution. Subsequently, in-situ measurement of sorption of MB molecules by the powder granules was started after adding 0.1g of the powder granules to the 50ppm MB solution. The wavelength range of 400 to 900 nm was accessed during experiments. Sorption data were collected at every ten-minute interval up to 2 hours and again after 24 hrs. In-situ measurement was started at time t=0 when the powder granules were added to the dye solution. It should be noted that the absorption due to silica at this wavelength range is negligible.[234] Thus, the change in absorbance recorded by the spectrophotometer will be due to (i) removal of MB from the light path or (ii) change in local concentration of MB as a result of sorption by the silica micro-capsules.

Visual evidence of the sorption is provided in Fig. 3.15 by the photographs of the vials of MB solution from t=0, continuing up to the end of 24 hours of exposure. The vials labelled 1, 2, 3 and 4 representing G-110, G-130, G-160 and G-180 respectively were all turbid at the start of the observation period. However, the vials become fully transparent at the end of 24 hours of exposure.

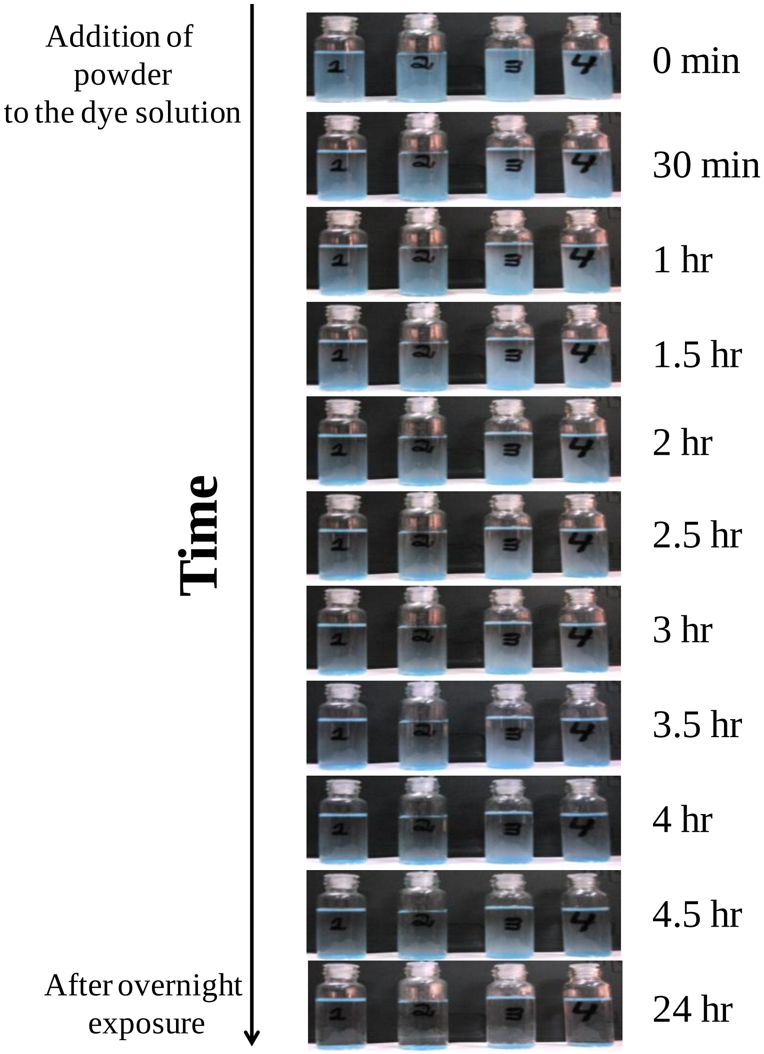

Fig. 3.15 Photographs of the vials over time, starting at t=0 min denoted by the addition of the granules to the dye solution, to t=24 hr completing overnight exposure. The capsules take up the MB dye and settle at the bottom leaving a clear supernatant. The vials 1,2,3,4 correspond to the case of G-110, G-130, G-160 and G-180, respectively.

The changes in the UV-Vis absorbance spectra of the dye solution with time for the wavelength range of 500 to 800 nm, is shown in Fig. 3.16. The UV-Vis spectrum for pure MB has a characteristic monomer peak around 664 nm. Presence of MB as dimer is denoted by a hump around 624 nm.[235] From Fig. 3.16, it is evident that the functionality and temporal evolutions of the absorption spectra are significantly distinguishable for the four cases. For nearly spherical and relatively compacted granules (G-110 and G-130), absorbance shows a monotonic decrease with time, whereas for hollow and toroidal granules, (G-160 and G-180) the temporal dependence of absorbance is significantly different.

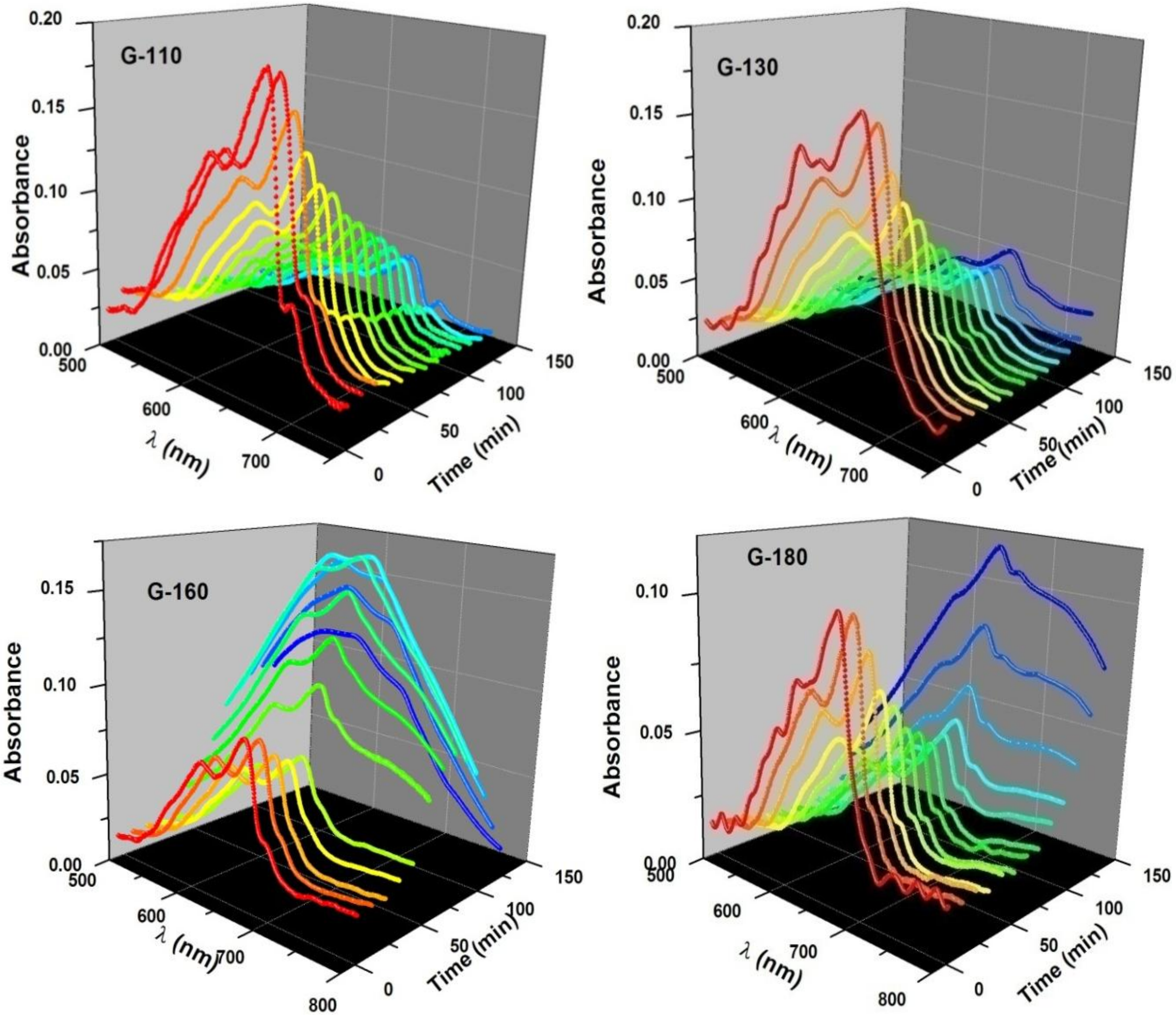

Fig. 3.16 Temporal evolutions of UV-Vis absorbance spectra of MB solution after addition of granules.

Owing to the presence of two peaks in the sorption spectra, the contribution of each can be obtained by de-convoluting the whole spectra into dimer and monomer contributions for each of the cases, as given in Fig. 3.17. The total absorbance has been represented by linear combination of two Gaussian functions, $y(x)=\sum_{i=1}^{2} A_i e^{-\frac{(x-\mu_i)^2}{2\sigma_i^2}}$ where, A_i denotes the scale factor, μ_1 and μ_2 are the peak wavelength value for the monomer and dimer absorbance peaks. The standard deviation σ_i and scale factor A_i were estimated using least square method.

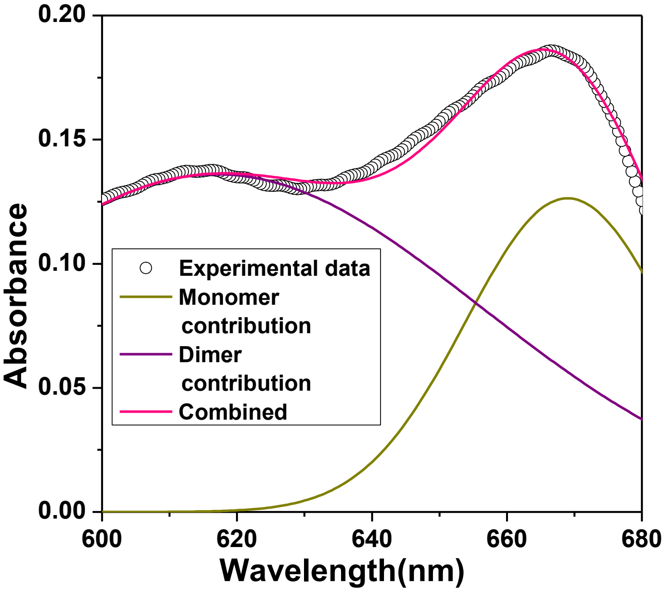

Fig. 3.17 Absorption spectrum de-convoluted by two Gaussian functions.

The behaviour of the de-convoluted monomer and dimer peaks with time over two hours is plotted on Fig. 3.18. Absorbance at t=0 for G-110 and G-130 is around ~0.14. It is evident from the trend of their sorption spectra that the peak value for both monomer and dimer decreases monotonically with time. This implies continuous sorption of the dye molecules by the granules and their eventual settling. On the other hand, the sorption behaviour of the G-160 granules is significantly different from the previous two cases. Here, the spectrum shows an increasing trend in absorbance during ~40 to 80 min reaching a maximum value at ~80 min and then falling continuously. G-160 granules stay afloat for a longer time as they are hollow and continue sorption before settling eventually. The rise in the absorbance peak is due to the preconcentration of MB in the floating granules. The eventual fall corresponds to the removal of MB from the path of the incident beam due to settling of the granules at the bottom, after sorption. Further for G-160, contribution from dimer is significantly more than that from monomer. This is because of enhanced dimerization of MB at the prominent dents on the surface (Fig. 3.1) and inside the hollow cores. For G-180, the granules are prominently doughnut shaped with central holes. However, because of the conversion of hollow spheres into doughnut (central hole reduces the effective available hollow space); the hollowness in this case gets reduced as compared to the G-160. Therefore a fraction of these granules settle down quicker than G-160 after dye sorption. This gives an initial decrease of absorbance in this case as seen for G-180 in Fig. 3.18. However, few hollow granules which still float continue to take up MB, increasing the local concentration of MB in the path of the optical beam after ~80 minutes.

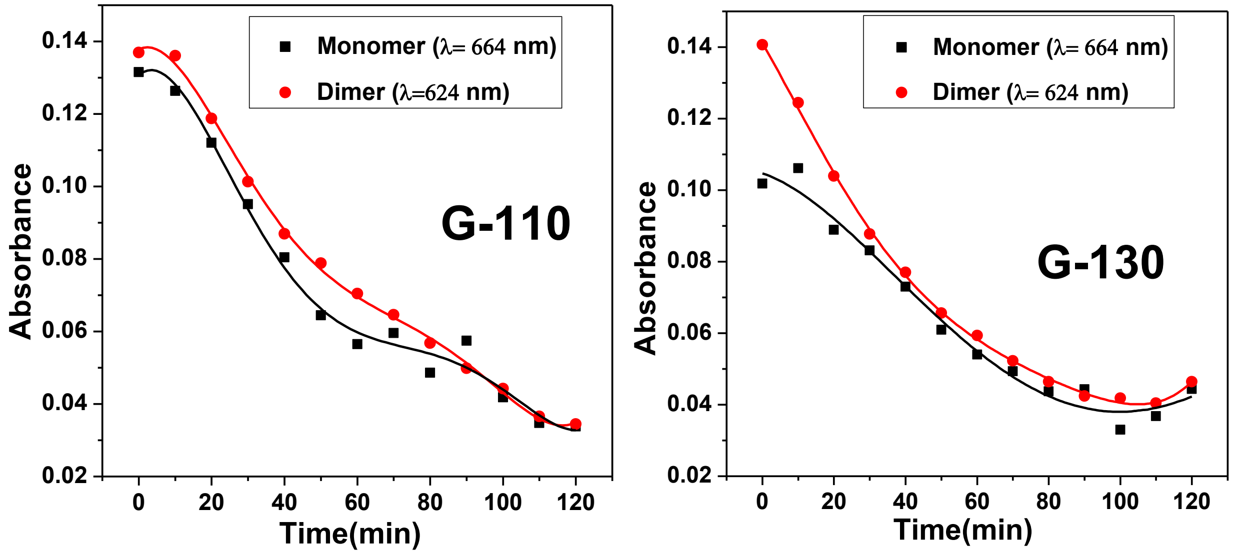

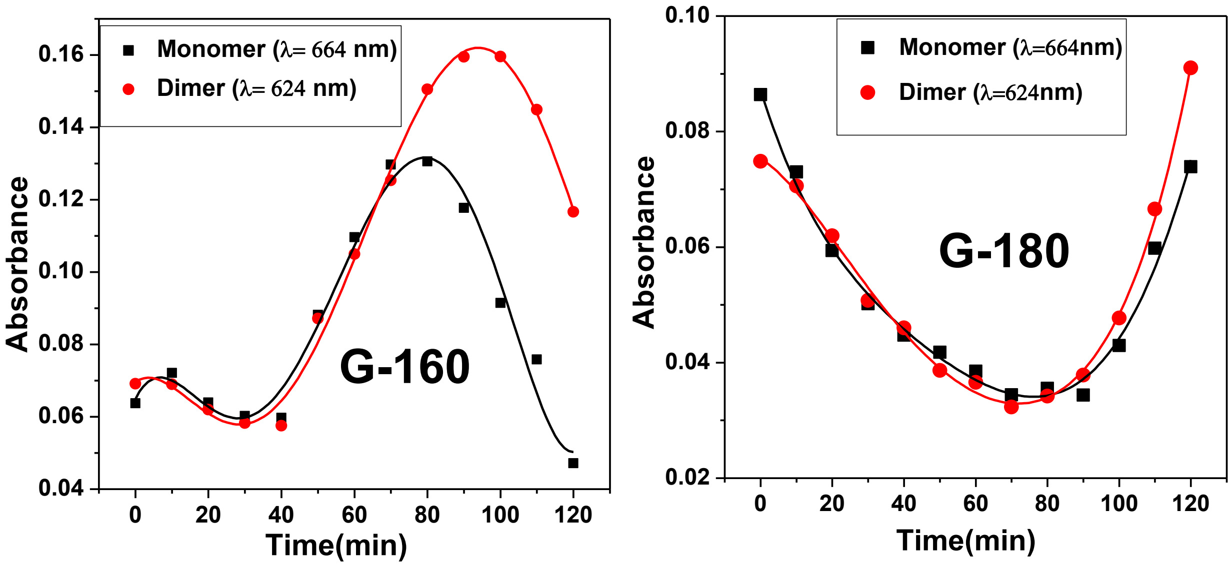

Fig. 3.18 Temporal variation of monomer and dimer absorbance peak in first two hours of sorption.

The percentage fall of the peak values of absorbance (compared to that of pure dye) for monomer and dimer with time is denoted in Table 3.5. It is seen that the instantaneous (at t=0), as well as the cumulative sorption varies distinctly in four cases. At t~0, the G-110 records the least fall in the monomer peak-absorbance value (~25%). For dimer, there is no appreciable change. The peak gradually falls with time up to 2 hrs (~82% sorption by the granule). G-130 shows a similar conduct but with a higher recorded percentage fall in absorbance. G-160 shows the highest dip in peak-absorbance value at t~0 (~63% instantaneous sorption) and registers a considerably higher absorbance (~91% sorption by granules) after 24 hours as well as compared to G-110 or G-130. G-180 also has a similar trend as that of G-160. Thus conclusively, hollower the granules, better is the sorption. Fig. 3.19 depicts the absorbance spectra at 24 hours from the start of the experimental period, denoting the sorption after overnight exposure of the granules to the dye solution.

Sample	% fall of peak absorption t=0		% fall in 1 hour		% fall in 2 hour		% fall at 24 hour
	Monomer peak (664nm)	Dimer peak (624nm)	Monomer peak	Dimer peak	Monomer peak	Dimer peak	(Change w.r.t 2nd hour)
			(Change w.r.t t=0)		(Change w.r.t 1st hour)		
G-110	24.7	-	64.7 (↑)	36.4	82.4 (↑)	74.6 (↑)	82.4 (↑)
G-130	40.0	-	70.6 (↑)	45.5	70.8 (↑)	57.6 (↑)	88.2 (↑)
G-160	62.9	37.3	41.2 (↓)	9.09 (↓)	70.6 (↑)	3.06 (↓)	91.2 (↑)
G-180	49.4	36.4	77.6 (↑)	67.3 (↑)	56.5 (↓)	18.2 (↓)	94.1 (↑)

Table 3.5 % fall of the absorbance peak Methylene blue dye at different time instances. For pure MB, the monomer peak value of absorbance is 0.17 while for dimer it is 0.12. ↑ indicates an increase of sorption by the granules, whereas ↓ indicates a decrease in sorption.

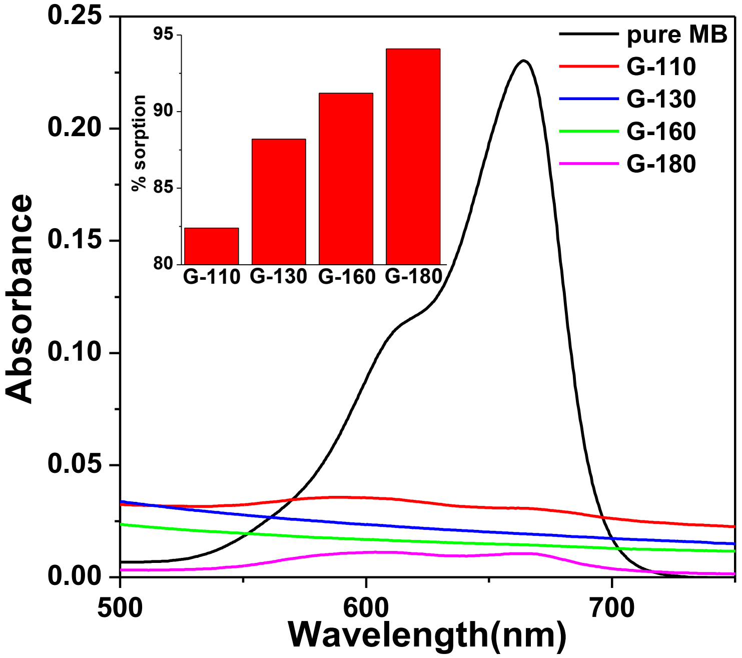

Fig. 3.19 UV-Vis absorption spectra for MB dye after 24 hours sorption by the granules compared to the pure dye. **INSET:** Percentage cumulative dye sorption after 24 hours.

Sorption studies have also been conducted for another well-known cationic dye, Rhodamine-B (Rh-B). Rh-B is known to possess a non-planar 3D structure having in-planar dimensions 1.5 x 0.98 x 0.43 nm and measuring 1.8 nm diagonally off-plane[236] unlike the planar molecules of MB that measures 1.4 x 0.6 x 0.4 nm[237] as shown in Fig. 3.20(a). The UV-Vis spectrum for the same over two hours is shown in Fig. 3.20(b). It is evident that the fall in absorbance peak (at 554nm) after 2 hours is significantly lesser (16%) when compared to that for MB (82%). Further, the peak absorbance value does not change appreciably with time even afterwards. Such retarded sorption kinetics in case of Rhodamine-B can be attributed to its structural as well as chemical characteristics. These molecules face steric hindrance during sorption in the granules due to their 3D bulky structure. MB is a stable cation in water due to the presence of positive charge on nitrogen. However, in the case of Rhodamine-B, the presence of the ethyl groups on the protonated nitrogen reduces its cationic character due to positive induction effect. At the same time, the presence of the carboxylic group tends to impart a negative charge on the molecule in an aqueous medium, thereby reducing the net positive charge of the molecule. Thus, the above-mentioned factors reduce the degree of positive charge of cationic Rhodamine-B ion. Therefore, the sorption probability of Rhodamine-B by the silica granules is lesser than that of MB. Hence the size of the sorbed entity is also crucial for efficient uptake of the dye along with properties such as size of the interstitial spaces, interaction with the sorbent, etc.

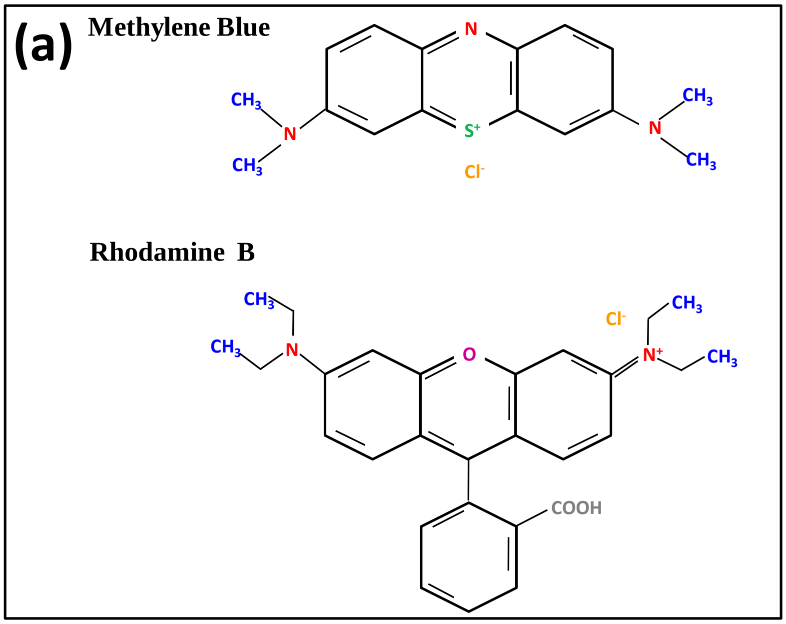

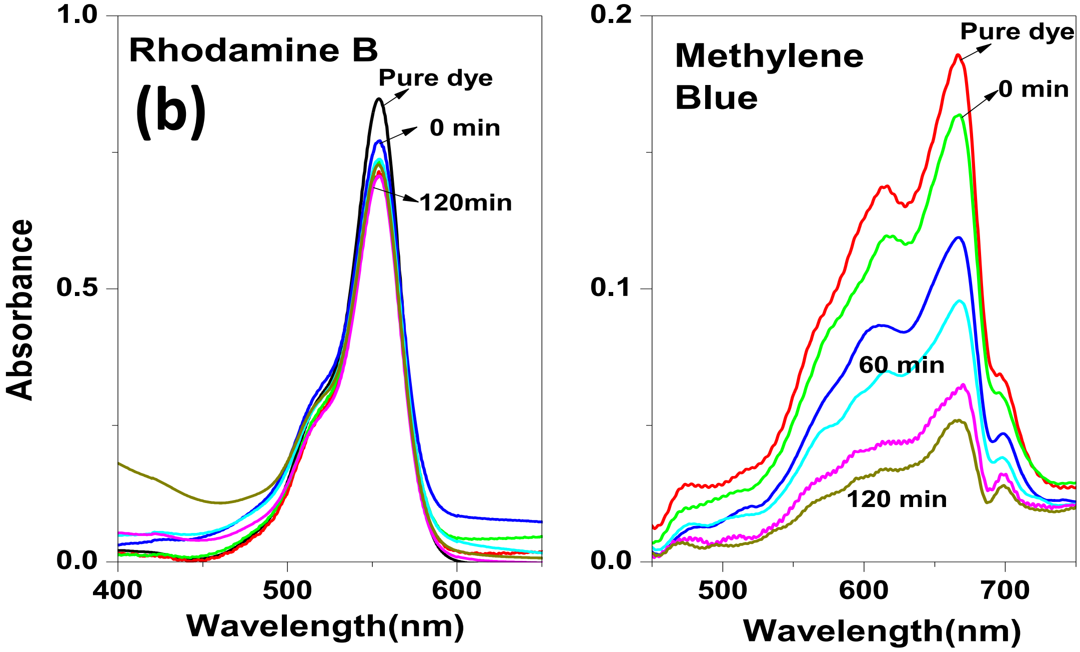

Fig. 3.20 (a) Molecular structure for Methylene Blue and Rhodamine B. **(b)** Evolution of absorption spectrum in two hours.

3.2.3 Evidence of dye sorption from SAS

The accumulation of dye in the granules is also reflected on the SAS profiles of the granules after dye sorption. The virgin granules (before sorption), as well as those after MB sorption, have been probed by small-angle X-ray scattering technique. SAXS, being a non-evasive technique, provides the correlation between the nanoparticles in the granule.[164] The scattering profile of the assembled granules before sorption $I_{before}(q)$ can be represented by additive scattering contributions from correlated nano-particles and from overall granules, having the form of Eq. 3.1. Scattering profile before and after sorption has been depicted in the same scale for comparison on Fig. 3.21. Intensity profiles ($I_{after}(q)$) of the dye-incorporated granules showed an additional scattering contribution over the scattering from the virgin granules ($I_{before}(q)$) i.e,.

$$I_{after}(q) = I_{before}(q) + I_{MB}(q) \tag{3.10}$$

where $I_{MB}(q)$ is the additional scattering contribution from the sorbed MB in the granules. As apparent from Fig. 3.21, the scattering at low q region is enhanced significantly due to MB sorption and the functionality follows a power law $I_{MB}(q) = Cq^{-\alpha}$ behaviour. The fitting parameters of the SAXS profiles are tabulated in Table 3.6. It is seen that the ratio of scattering intensity from the granules after and before sorption (I_{after}/I_{before}) is more for granules with more hollowness (G-160, G180), compared to those with lesser hollowness (G-110, G-130) affirming the fact that hollower the granules, better is the sorption.

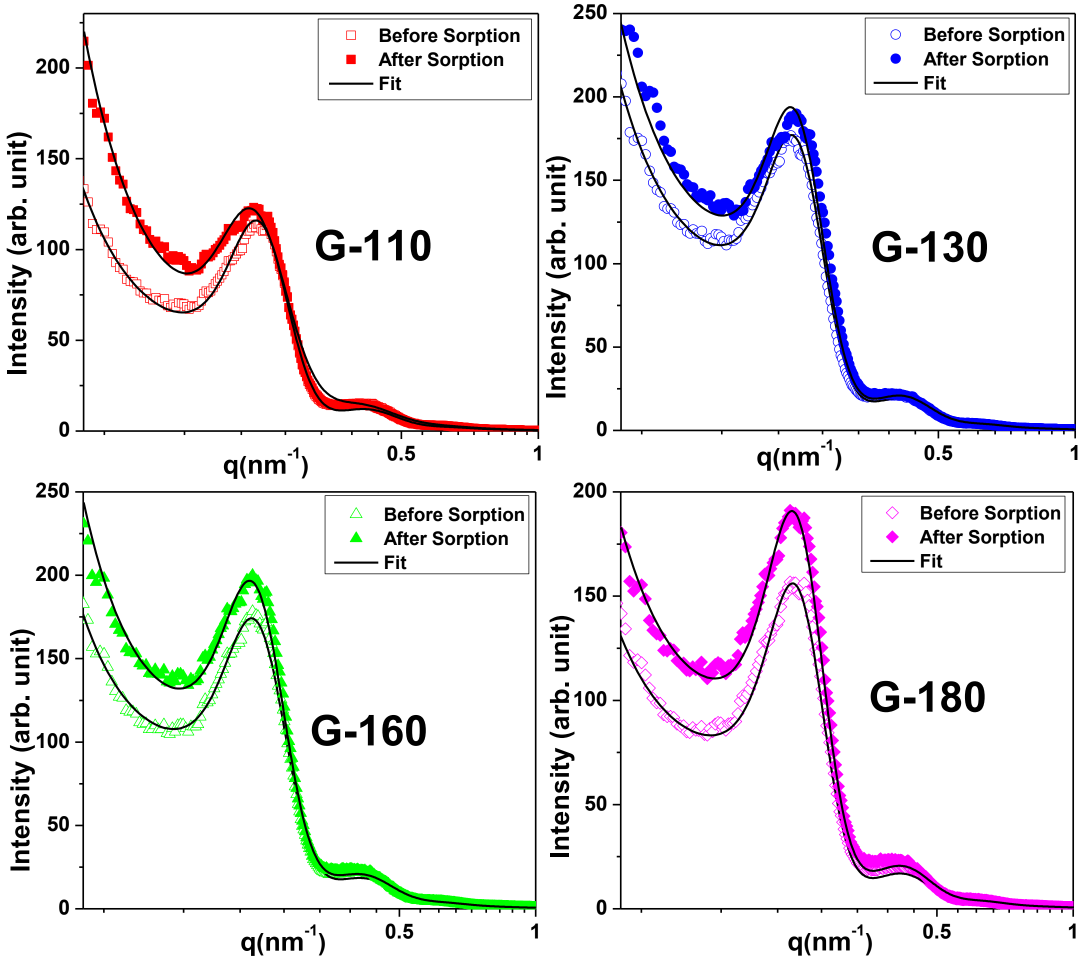

Fig. 3.21 SAXS profiles of the granules before and after dye sorption. The extra scattering at low q after sorption is due to the sorbed MB.

Sample	**Polydispersity index of lognormal nanoparticle size distribution**	**Median nanoparticle radius (nm)**	**Scattering from sorbed MB ($Cq^{-\alpha}$)**	
			[I_{after}/I_{before}] at q= 0.25 nm^{-1}	α
G-110	0.13	13.5	1.10	3.12
G-130	0.12	13.8	1.11	3.52
G-160	0.13	13.7	1.15	3.57
G-180	0.12	13.8	1.21	3.20

Table 3.6 Parameters obtained from model fitting of SAXS profiles of granules after dye sorption.

3.2.4 Thermal Analysis

With the increase of temperature, the sorbed dye in the granules undergoes various thermal changes that were investigated with the help of thermo-gravimetric analysis (TGA) and differential thermal analysis (DTA). TGA and DTA measurements on the four types of dye-incorporated powder granules were carried out using Netzsch Thermo-balance (Model No.: STA 409 PC Luxx) coupled to Bruker FTIR system (Model No.: Tensor 27) via a heated Teflon capillary (1 m long, 2 mm inner diameter) in air atmosphere.

TGA essentially measures the change of mass of the sample as a function of temperature. Fig. 3.22(a) depicts the mass loss due to the gradual decomposition of the sorbed dye in the granules with temperature. TGA profiles show two distinct zones. The rate of mass loss in the first zone, which extends up to ~130°C, is relatively fast and is due to surface water evaporation. The second zone, above this temperature, shows a slower descent compared to the first zone. The mass loss in the second zone is attributed to the release of confined water/organic/inorganic moiety. It is interesting to note that the percentage mass loss is maximum for G-110 while it is minimum for G-180. This indicates that sorbed dye molecules inside the hollow core in G-160 and G-180 tend to aggregate[238] and thus are unable to be released as fast as surface molecules in case of G-110 or G-130.

DTA technique monitors the temperature difference between sample under study and an inert reference under identical thermal cycles[239] to detect the various chemical changes occurring in the sample characterized by absorption or emission of heat. DTA measurements were carried out for the granules after dye sorption.[240] Fig. 3.22(b) depicts the DTA curves exhibiting both positive and negative peaks. Negative peaks are due to absorption of heat from the system corresponding to an endothermic process, such as evaporation. On the other hand, positive peaks denote liberation of heat, i.e. exothermic processes, such as dissociation or decomposition. The first endothermic dip is observed around 100°C. This corresponds to the evaporation of the surface water from the granules. It is to be noted that for free MB, degradation initiates around 250°C[241] where these molecules undergo cyclization, with the liberation of N atoms and dissociation of Cl. However, in the present case, the MB molecules are not truly free but confined to a nano-porous network, thus MB will respond differently to the temperature change. In the present case, we observe that there are two prominent exothermic peaks. The first peak initiates at around 200°C. The appearance of this peak is attributed to degradation occurring at a lower temperature. MB molecules can undergo two kinds of cyclization; intermolecular and self. Intermolecular cyclization is energetically more favoured because it does not involve multiple bond-breaking within the molecule and thus it will commence at a lower temperature (first exothermic peak in Fig. 3.22(b)). Proximity of the MB molecules inside the hollow structure, results in inter-molecular cyclization, and dimer formation. It is seen that there is almost no peak at ~200°C for G-110, this is because, G-110 are fairly dense granules, with sorbed MB residing only on the surface. On the other hand, we hypothesize that self-cyclization will occur at a high temperature, as represented by the peak above 400°C. This process will occur for all the four sets of granules as, rearrangement and bond-breaking within a molecule does not necessarily require confinement. It is to be noted here that these significant changes at ~200°C and ~400°C could not be spotted with TGA, as mass loss is negligible for the pre-concentrated MB in the granule.

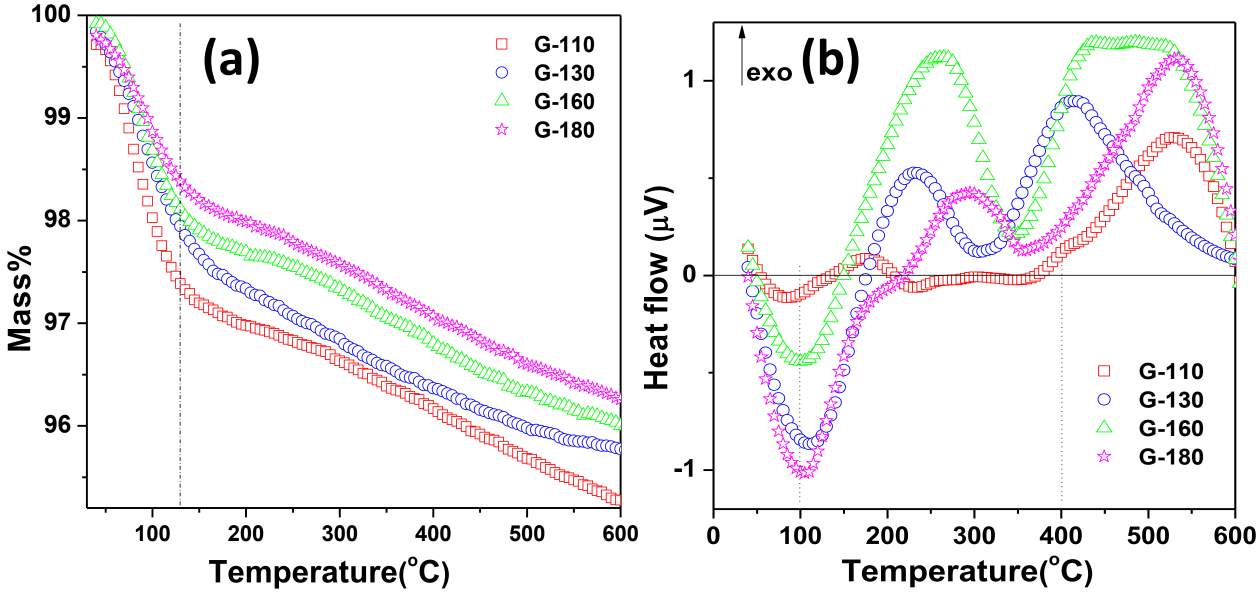

Fig. 3.22 (a) TGA curves showing the loss of mass as a function of temperature. **(b)** DTA plots denote the thermal changes occurring at different temperatures. Upward arrow indicates exothermic processes.

3.2.5 Conclusions

In summary, this chapter illustrated the application of nano-structured silica micro-granules as sorbent for water-soluble Methylene Blue dye. The sorption characteristics were found to be strongly morphology dependent. Hollow and doughnut-shaped capsules showed better sorption-efficiency as compared to the compacted spherical granules. The present investigation also indicated that compatibility of interstitial pore sizes and the molecular shape of the dye is a crucial factor as far as the sorption behaviour of the granules is concerned. This exercises suitable control for preferential dye sorption applications.

Chapter 4: Granules with hierarchical pores from bi-colloidal suspension

4.1 Preamble

The versatility of porous materials[242] has been a subject of immense intrigue over decades. Rigorous researches have been carried out, both from the synthesis and utilization points of view. The methods that are generally employed for synthesis of porous materials include freeze-drying,[243] micro-emulsion formation,[244] gas blowing techniques,[245] phase separation,[246] template imprinting,[100] suspension polymerization,[247] etc. The synthesis protocols for some of these methods are complex, involving the use of expensive chemicals or requiring significant energy consumption. The obtained porous materials are often in monolithic form rather than single entities with defined shapes. Furthermore, even though some of these techniques are suitable for production at a laboratory scale, they become extremely costly for large-scale up-gradation.

In Chapter 3.2, nano-structured micro-granules were reported to function as porous materials, owing to their inherent hollowness and inter-nanoparticle voids. The flexibility of the energy efficient spray-drying process further enthuse investigation of novel methods towards generating hierarchical pore structures in the micro-granules. The current work describes the method of porogenation of mesopores and macropores[248] in silica micro-granules synthesized via spray-drying of a mixed colloidal suspension. Porogenation is essentially by the removal of one of the components from such a composite granule. The choice of the colloidal mixture were made keeping in mind that one of the components would act as the template of the pore, which will later be removed.[249] Needless to say, control over the pore sizes would be exercised by the template component.[249-251] In general, micelles, polymer,[252] liquid crystals,[250] inorganic precursors,[253] etc. are used as templates of mesopores. For macropores, the use of bacterial templates[95] has also been reported. However, incorporation of both mesopores and macropores in the same material using a single template remains a challenge. Such porogenation is advantageous from the application point of view. For example, in case of catalysis; the active sites are often located in the micropores and mesopores, while the macropores aid mass transfer.[254] The present work describes an economic and facile process of synthesis of porous silica micro-granules with hierarchical pores using milk as the template.[255]

Spray-drying is carried out using a colloidal suspension composed of nano-silica and milk as the feed solution. Pores are generated in the composite micro-granules by the removal of milk by calcination. Milk act as the soft template for the pores whereas nano-silica forms the matrix. Milk in its natural colloidal form is a complex emulsion containing fat globules and casein micelles, which are suspended in an aqueous phase.[256] Shear during the atomization process of the spray droplets, can partially break the relatively large sized globules and agglomerates into smaller forms. Moreover, the re-agglomeration of a fraction of these broken units during sol to powder transition may lead to larger agglomerates as well. Thus, the type of pores depends on the size of milk agglomerates. It has been shown that depending on the initial milk concentration in the colloidal suspension, a combination of mesopores and macropores can be generated in the granules through the present technique.

4.2 Synthesis of micro-granules with hierarchical pores

Three types of silica nano-suspension, (i) HS-40 [LUDOX®, Sigma Aldrich, USA] with ζ potential ~ - 48 mV, (ii) VISA [M/S. VISA Chemicals, Mumbai, India] with ζ~ -44 mV and

(iii) VISA with ζ~ +53 mV were diluted to 2% by weight by adding distilled water. Amulya brand of milk powder [Gujarat Co-operative Milk Marketing Federation Ltd., Anand, India] was mixed with distilled water to make 1, 2 and 3% by weight emulsions (ζ ~ - 35 mV). The total fat content of milk was 20% by weight. 2% by weight colloidal HS-40 was mixed with the milk emulsions (1, 2 and 3%) separately to make three bi-colloidal dispersions. VISA silica with +ve ζ and –ve ζ (2% by weight) were also mixed to 2% by weight milk suspension individually to make two separate bi-colloidal suspensions. For further reference, the bi-colloidal granules with HS-40 will be referred to as S-H1, S-H2, and S-H3 for 1, 2, and 3% of milk in the granule respectively. Similarly, 2% by weight milk composite with VISA silica of +ve ζ and –ve ζ will be referred to as S-VP and S-VN, respectively. Each of these bi-colloidal dispersions was prepared as 100 mL precursor solutions for spray-drying by spray dryer, LU-228 (LABULTIMA, India). The precursor solution was fed into an atomizer at a constant feed rate of 2 mL min^{-1}. The atomizer nebulizes the suspension into tiny droplets with an average diameter of 10 μm. A constant aspirator rate and inlet temperature of 160^{o}C was maintained throughout the synthesis processes. For reference and comparison, pure silica dispersions (2% by weight) for HS-40, VISA (+ve ζ) and VISA (-ve ζ), were also subjected to spray-drying under the identical drying conditions.

Removal of milk from the composite granules after spray drying was carried out by two different processes: i) washing the freshly spray-dried granules (500 mg) with 50 mL of 10% (v/v) hydrogen peroxide solution where the aliquots were kept overnight under continuous stirring. The granules were recovered after disposing off the clear decants ii) the samples were calcined at 450^{o}C for about 7 hours in air to remove the template component through incineration.

4.3 Structural characterization by FESEM

Fig. 4.1 depicts: (a) the FESEM micrographs of the granules (b) surface topography and (c) Fourier transformed images of the micrographs. It is evident from the figure that the morphology of the formed granules strongly depends on the milk concentration as well as relative polarity (ζ-potential) of the individual components in the bi-colloidal dispersion. From the FESEM micrographs, it is evident that the granules are primarily doughnut-shaped for S-H1, 2, 3 and S-VN. However, S-VP granules are nearly spherical. The granules with higher concentration of milk show more deformation. It is interesting to note that for the cases where silica and milk both possess –ve ζ, the granules are doughnut-shaped. On the other hand, for opposite polarities of silica and milk (ζ_{Silica} ~ + 53 mV, ζ_{Milk} ~ - 35 mV) in case of S-VN, spherical granules are obtained. The doughnut shapes of the granules for the case of similar polarity of the components are attributed to buckling of hollow shells as was discussed in Chapter 3.1. However, for opposite polarity of the components, granules possess a spherical shape due to the hindrance of shell formation. This indeed indicates the significant role of the inter-particle interaction in morphological transformation. It should be mentioned that in some earlier works, [46-47, 53, 87-89, 93-95, 103, 188, 257, 54, 102] it was indicated that the spherical shape of droplet is retained even in the granule because of isotropic shrinkage of the droplets at slow drying rate. However, in the present case, at a drying temperature of 160°C, the granules are expected to be doughnut-shaped owing to the fast drying scenario.[188] The formation of spherical granules (S-VP) is attributed to the charge interaction among silica nanoparticles and milk in the bi-colloidal suspension. Owing to their opposite polarities the individual components tend to aggregate in the dispersion due to electrostatic attraction. During drying, the diffusion of these large-sized flocculates is slower than the individual nanoparticles. Hence, in this case, even under the fast drying scenario, shell formation is hindered due to the constrained diffusion. Thus, the granules are spherical in shape. In contrast, the situation for silica and milk having same polarity is similar to the case of shell formation as was discussed in Chapter 3.1. It is to be noted that the spray-dried composite granules are stable enough and calcination does not modify the overall structure of the granules, rather only generates pores due to the incineration of milk moieties.

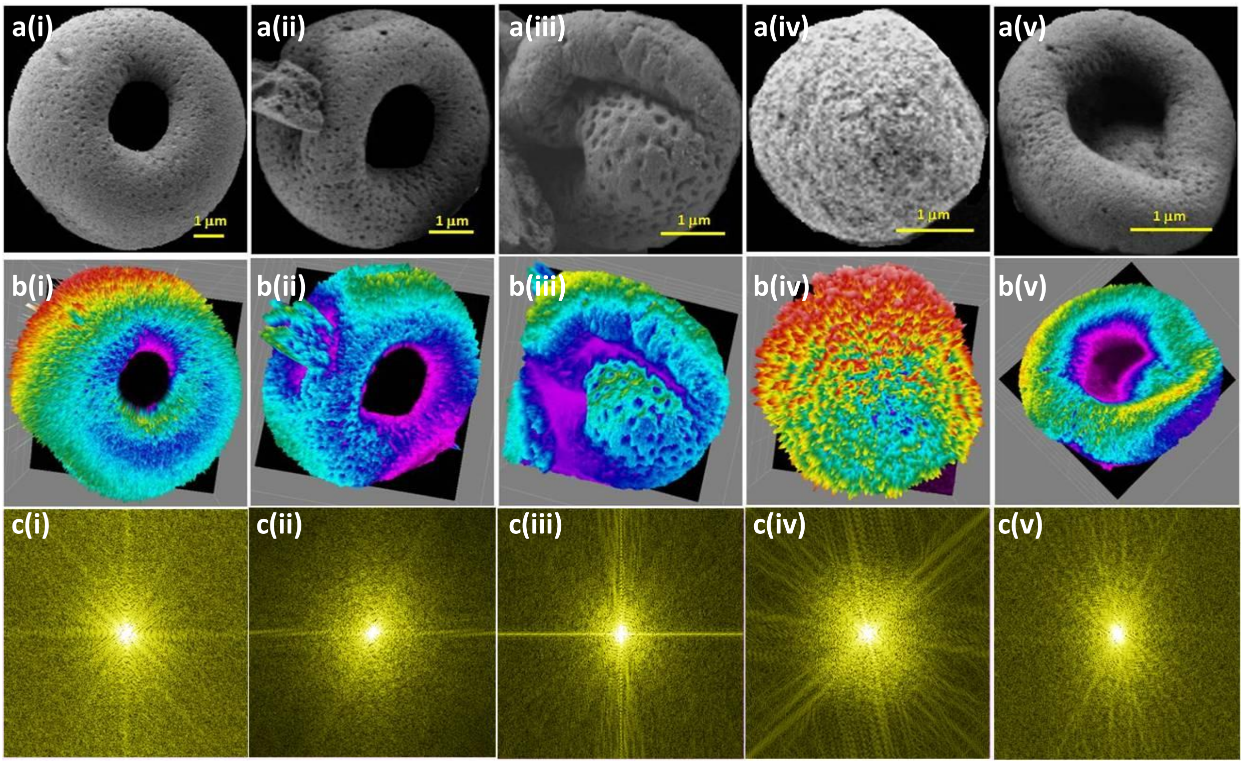

Fig. 4.1(a) FESEM micrographs. **(b)** Topographical representation by colour map. **(c)** Representation as Fourier transformed images. (i) S-H1 (ii) S-H2 (iii) S-H3 (iv) S-VP (v) S-VN

The FESEM micrographs of the granules have been represented as colour maps in Fig. 4.1 (b), to elaborate the roughness of the granular surface. It is discernible that for S-H3 (maximum milk concentration) and S-VP (opposite surface polarity), the roughness on surface is more pronounced as compared to S-H1, S-H2, S-VN. Fig. 4.1(c) depicts the 2D Fourier transform (FT) of the micrographs. FT images represent the surface features of the granule in reciprocal domain.[258] The spread of halo away from the central spot denotes smaller details of the image. Fig. 4.1(c(i)) show a number of centrally intersecting straight lines for S-H1 denoting significant symmetry. The delocalization of FT signal away from the centre indicates presence of numerous small pores on the surface. The outward spread of FT signal reduces in case of S-H2 (Fig. 4.1(c(ii)) and furthermore for SH-3 (Fig. 4.1(c(iii))) indicating the increase in pore sizes. Thus, a qualitative idea of variation of pore sizes on the surface of the granule is obtained from FT analysis of the FESEM micrographs.

The granular shape symmetry is depicted graphically in Fig. 4.2(a). The correlation between the top and bottom halves of each image in Fig. 4.2(a) has been presented by plotting diametrically opposite effective chord lengths (σ_y^+, σ_y^-). For a perfectly symmetric granule, a plot between σ_y^- and σ_y^+ will be a straight line passing through the origin and having a slope equal to unity. Deviation from this line indicates the extent of non-symmetry. The dotted line on figure shows the idealized symmetric case for clarity. Fig. 4.2(a) reveals that S-H1 and S-H2 are nearly symmetric whereas S-H3 shows maximum deviation from symmetry, having a slope value of ~0.4. This deviation is due to granular deformity as a result of buckling during spray drying. The milk concentration in the bi-colloidal solution influences the extent of buckling in the dried granule as is evident from this preliminary analysis. Fig. 4.2(b) represents the qualitative trend of the dimension of the macro-pores as obtained from image analysis.

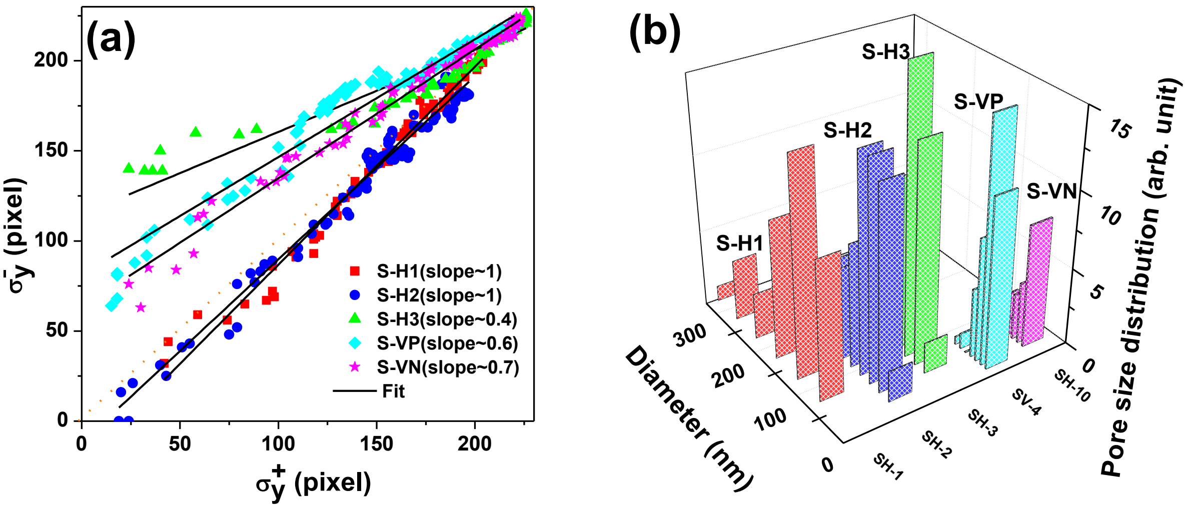

Fig. 4.2(a) Estimate of the symmetry in the granules **(b)** Macro-pore size distribution.

4.4 Fourier Transform Infrared (FTIR) spectroscopic analysis

FTIR studies were performed for the composite and pure silica granules in order to account for changes occurring in the spectra due to the removal of milk by peroxide washing and calcination. The FTIR profiles are shown in Fig. 4.3(a-e). It is evident from the comparative studies that the spectra before and after peroxide washing/calcination show clear distinction. It was observed that initially, the composite granules show characteristic peaks corresponding to silica as well as extra peaks due to the milk components. After treating with hydrogen peroxide, the spectra show partial disappearance of the milk peaks and after calcination, the FTIR profile resembles that of pure silica. The characteristic dips in the FTIR profiles at ~3317 cm^{-1}, ~2925 cm^{-1}, ~1741 cm^{-1}, ~1534 cm^{-1}, ~1108 cm^{-1} which are present for the composite granules are absent for pure silica and for the calcined granules in each of the cases. Thus, calcination proves to be a more efficient method for porogenation than peroxide washing. The structural characterization of the pores by SAS and gas adsorption techniques are discussed in the following sections.

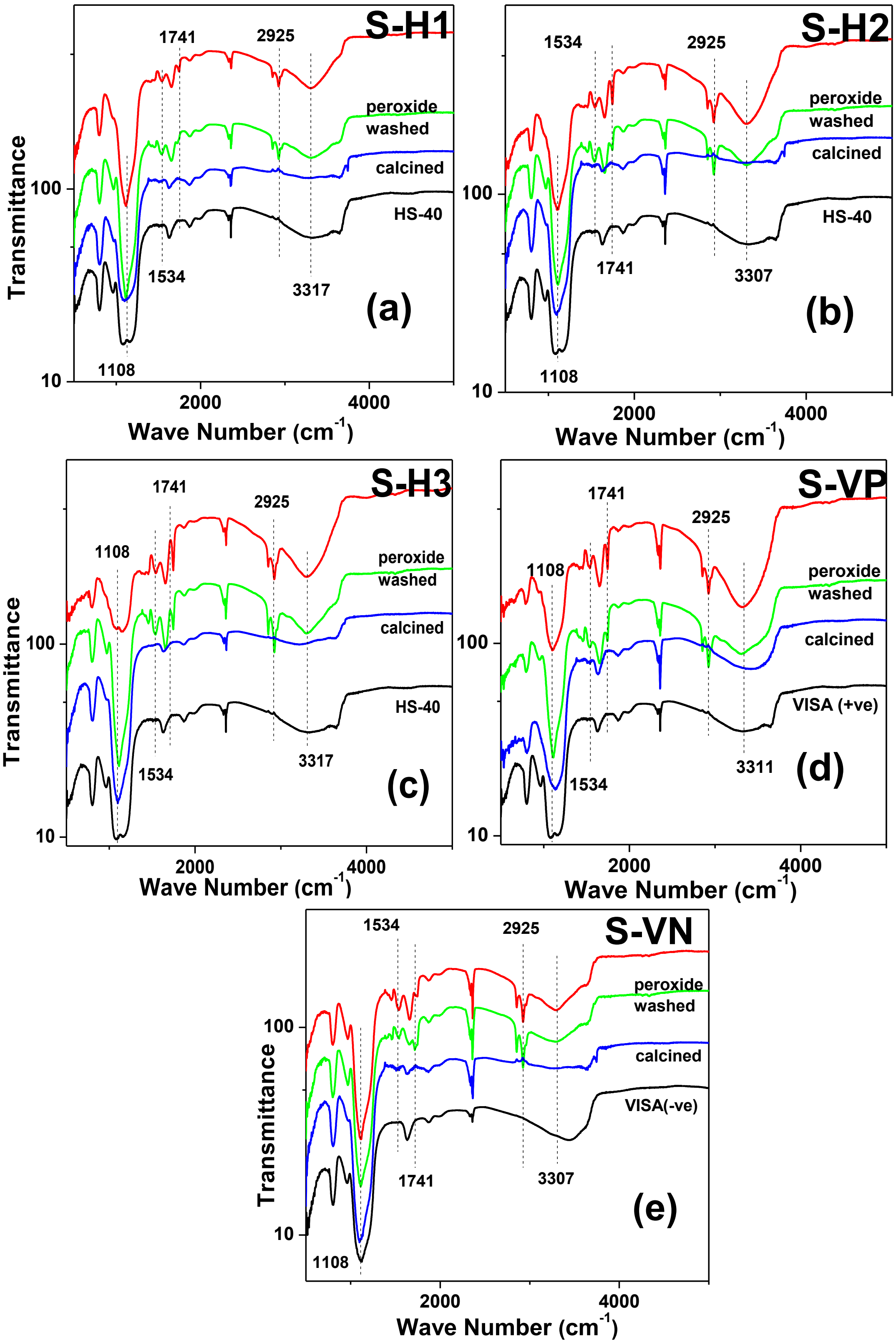

Fig. 4.3 FTIR profiles for the composite granules **(a)** S-H1, **(b)** S-H2, **(c)** S-H3, **(d)** S-VP, **(e)** S-VN, drawing comparison with pure silica granules, calcined and peroxide washed granules for each.

4.5 Mesoscopic structure characterization by SAXS

SAS provides a quantitative idea about the mesoscopic length scales in the granules. The structural, as well as inter-particle correlation among the components of the composite micro-granules and its alteration due to chemical treatment and calcination, is obtained from SAS in a statistical sense. It should be mentioned here that due to the presence of density fluctuations in the hierarchical length-scales of the present multi-component system, the analysis of scattering data becomes quite complex. However, for a simplistic approach, such scattering intensity profile can be represented by cumulative contributions from individual scattering components.[94-95, 104, 259] For calcined granules, the total scattering intensity $I(q)$ is approximated as a summation of scattering contribution from correlated silica, as well as from the whole granule following Eq. 3.1.[164] The decoupling of the scattering contributions works well in the present case where the size of the inhomogeneity in the different length scales differ widely.[104] The granules were characterized by both SAXS and MSANS corresponding to the high and low q regions respectively. Therefore MSANS furnish information about the large-sized inhomogeneity such as granular and macropore sizes whereas SAXS provides information about the silica nanoparticle sizes, correlation and mesopore sizes.

SAXS measurements were carried out for composite granules, granules after peroxide treatment and for calcined granules as well. Fig. 4.4 compares the SAXS profiles for each of the cases. Analysis of the SAXS profiles for the composites revealed that a sticky hard sphere type of correlation[192] exists between the silica nanoparticles. Table 4.1 summarizes the obtained parameters from SAS profiles of calcined granules. It is interesting to note here that SAXS data reveals two values of volume fraction of nanoparticles which denote non-uniform packing of nanoparticles in the granule. The nanoparticles are more close-packed at regions devoid of milk deposits, denoted by the higher volume fraction (ϕ_1) and loosely-packed at zones near the milk template mesopores, resulting in lower packing fraction (ϕ_2). For templated HS-40 granules (S-H1, S-H2, S-H3), it is observed that the value of ϕ_1 is typically 0.7, which is similar to its packing fraction in pure silica granules while ϕ_2 decreases with the increasing concentration of templated milk in the granule. It is to be mentioned that removal of milk from composite granules does not alter the silica correlation because of their secure interlocking during spray drying.

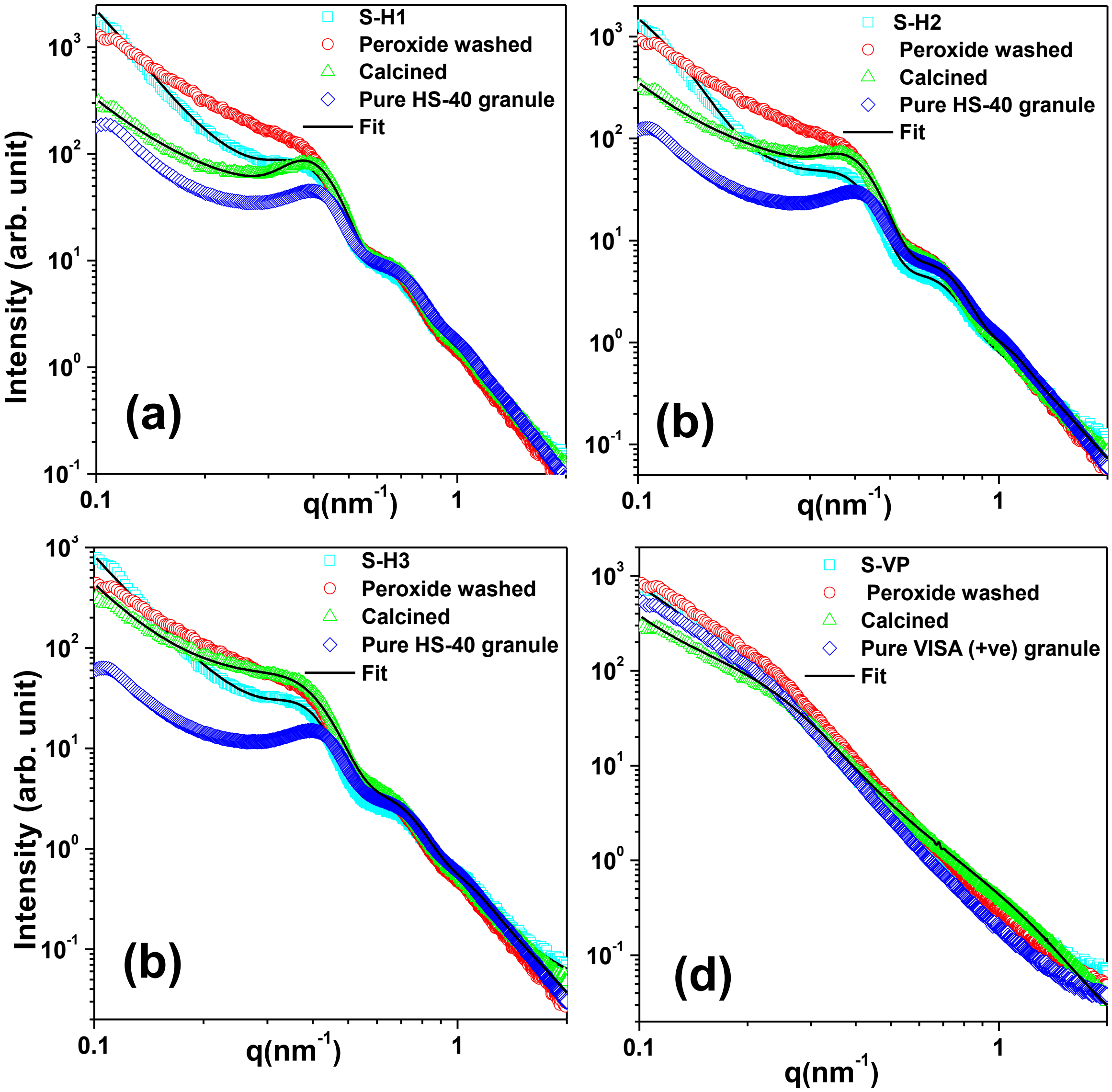

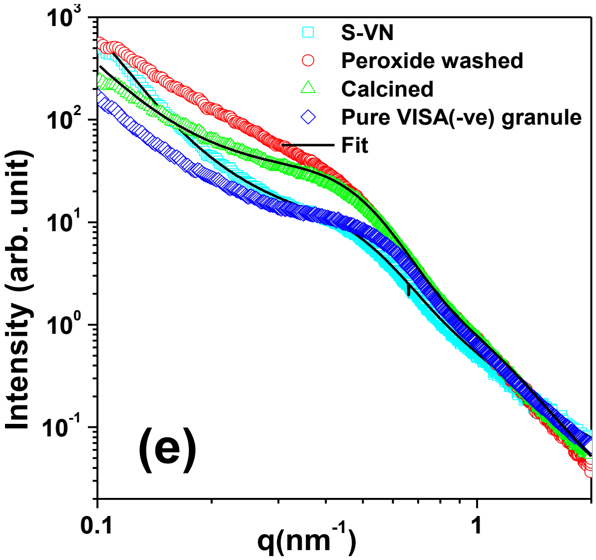

Fig. 4.4 SAXS profiles for **(a)** S-H1, **(b)** S-H2, **(c)** S-H3, **(d)** S-VP, **(e)** S-VN drawing comparison with scattering profiles of peroxide treated, calcined and pure silica granules.

Granules	Silica nanoparticles			
	Polydispersity index	Effective median size (nm)	Packing Fraction (ϕ_1)	Packing Fraction(ϕ_2)
Pure HS-40	0.16	7.80	0.72	-
S-H1	0.16	7.80	0.70	0.52
S-H2	0.16	7.80	0.70	0.47
S-H3	0.16	7.80	0.67	0.40
Pure VISA (+ve)	0.28	10.45	0.54	-
S-VP	0.28	10.45	0.54	-
Pure VISA (-ve)	0.27	4.65	0.49	-
S-VN	0.27	4.65	0.49	0.27

Table 4.1 Parameters obtained from model fitting of SAXS profiles of the bi-colloidal granules compared with pure silica granules.

Fig. 4.4 reveals noticeable differences in the scattering profiles of the granules, particularly in the low *q* regime. There is a significant dip in the scattering intensity in this *q* regime in case of the calcined granules when compared to that for composite granules. This is due to the removal of milk aggregates from the granules by calcination. On the other hand, in case of chemical treatment by peroxide, there is an increase in scattering at low *q* indicating the coalescence of milk moieties instead of removal. Thus, it is evident that calcination provides a better way of realizing porous structure by removal of milk template from the assembled bi-colloidal granules. However, there is a subtle difference between the profiles of the calcined granule and those of pure silica granules owing to the changed silica packing fractions due to mesopore generation as depicted by ϕ_2 in Table 4.1.

4.6 Characterization of porosity by MSANS and BET

The signatures of the macropores in the calcined granules were obtained from MSANS experiments which probed the *q* range (0.003-0.173 nm^{-1}). Fig. 4.5 depicts the MSANS profiles of the calcined granules. The estimated size of macropores and the corresponding specific surface area from MSANS is provided in Table 4.2.

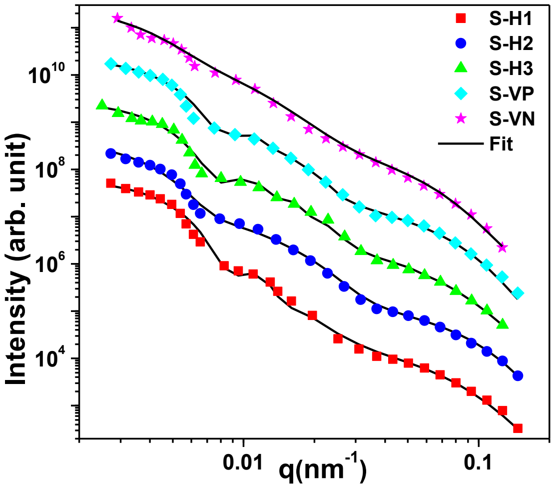

Fig. 4.5 MSANS profiles for calcined granules.

Sample	Specific Surface Area (m^2/g)			Average pore radius (nm)	
	Mesopores		Macropores (From MSANS)	Mesopores (From BET)	Macropores (From MSANS)
	(From SAXS)	(From BET)			
S-H1	171.0	137.2	26.9	2.77	82
S-H2	172.3	99.2	42.2	3.99	99
S-H3	170.1	96.6	37.0	8.51	115
S-VP	167.2	87.8	33.4	5.92	124
S-VN	170.4	133.7	27.8	3.81	98

Table 4.2 Pore sizes and specific surface area compared by BET and scattering techniques.

Granular porosity, specifically the mesopore sizes and the corresponding specific surface area was also obtained using BET technique. As depicted in Table 4.2, the average mesopore sizes were found to increase with the increase in milk concentration for S-H granules. On the other hand, the specific surface area decreases with milk concentration. Hence it is inferred that increased concentration of the soft template leads to a fewer number of pores having a large size (S-H3), as compared to a large number of small-sized pores at low concentration (S-H1). The adsorption-desorption hysteresis plot, the differential pore volume and the cumulative mesopore distribution as obtained from BET is shown in Fig. 4.6(a-c). Distinct differences in the plot are apparent due to the individual porosity of the granules.

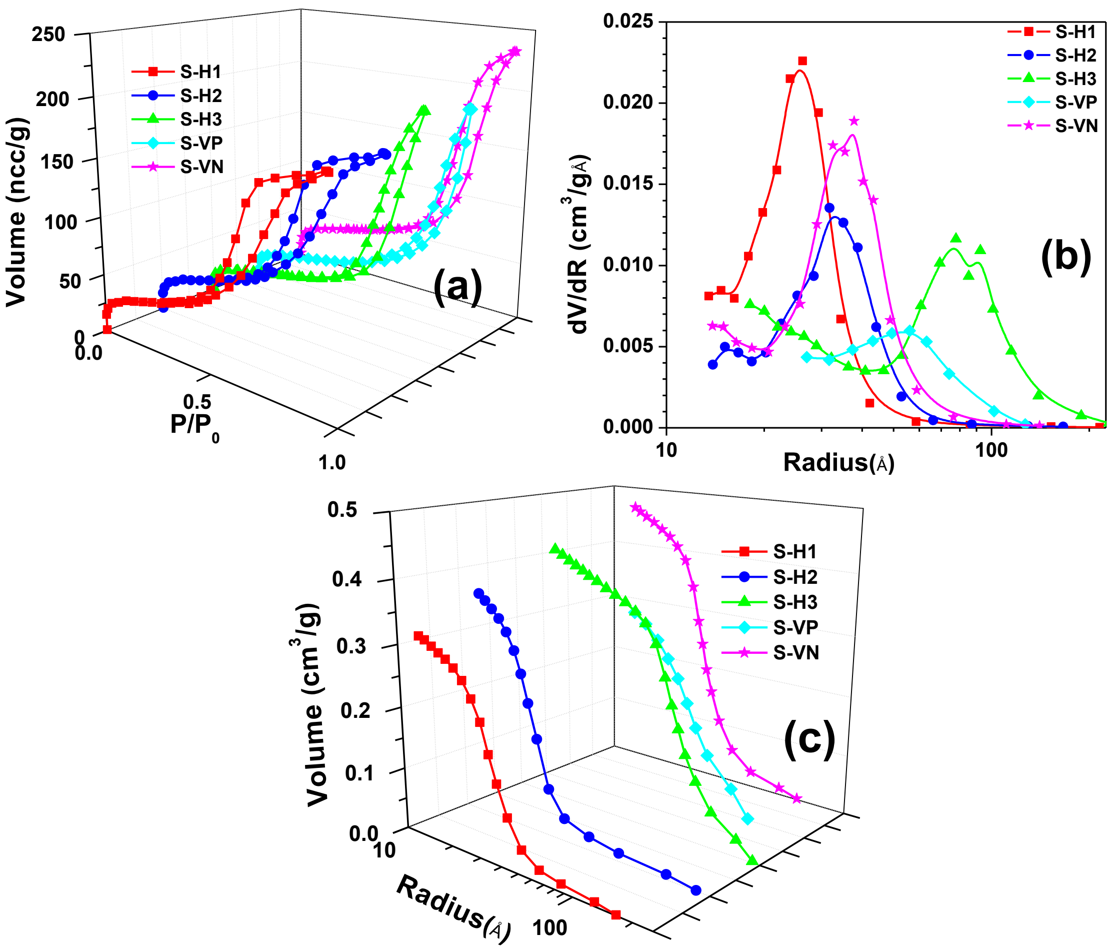

Fig. 4.6 (a) Adsorption-desorption isotherm as obtained from BET for the granules. **(b)** Differential mesopore volume distribution, **(c)** Cumulative mesopore volume distribution for granules.

It is apparent from Table 4.2 that there is a distinct difference between the *S*/*V* values obtained from the two techniques (SAXS and BET). This is because, BET being an adsorption/desorption technique, provides information about connected/open pores only. However, scattering results provide a cumulative contribution from both open and closed pores. Moreover, MSANS provided the specific surface area due to the macro-pores in the granule. A significant gain of *S*/*V* has been recorded for the calcined granules owing to the mesopores and macropores, when compared to the *S*/*V* for pure HS-40 silica micro-granules (80 m^2/g).

4.7 Conclusions

To summarize, the motivation of this work was to demonstrate a facile way of synthesizing porous granules via spray drying of bi-colloidal dispersion. The polarity and concentration of the colloidal components play a key role in governing the granular morphology. The soft component of the colloidal mixture acts as pore template in the granules. Efficient control of the pore sizes and the specific surface area was obtained by tuning of the concentration of the soft component. Both mesopores and macropores were generated forming a hierarchical pore network in the granule, by the use of a single template. This work unravels yet another potential applicability of nano-structured micro-granules as porous material, with a facile tuning of its porosity.

Chapter 5: Wrinkled micro-granules: Role of anisotropic interparticle interactions

5.1 Introduction

Surface wrinkling is ubiquitous in nature and is a commonly observed phenomenon on dehydrated fruits, ageing human skin, etc. which originate as a consequence of the simultaneous interplay of multiple physicochemical stimuli such as, temperature, humidity,[260] strain mismatch,[261] etc. Wrinkling patterns on a surface are useful for various applications including active size-selective adsorption/release,[262] stretchable electronics,[263] etc. Literature reveals the various methods by which surface wrinkling was induced on curved surfaces such as spheres.[260, 264] However, the synthesis techniques implemented were time-consuming and often uses rare chemicals.[265] Moreover in some cases the tuning of wrinkling patterns are complex and often result in partial wrinkling.[266] Mostly, the synthesis methods are successful at laboratory length scale but cannot be upscaled for industrial applications. In this chapter, a facile method of synthesis of surface-wrinkled granules has been demonstrated which overcomes all the above-mentioned technical drawbacks. To elaborate, evaporation-induced self-assembly proves to be a unique tool via which nano-structured micro-granules with wrinkled exteriors can be obtained from anisotropic colloidal suspension.

So far in this doctoral thesis, the effects of drying rate and the addition of soft template were investigated. However, in both of these cases, the obtained granules have smooth exteriors albeit their morphological differences. The role of colloidal interparticle interactions for the generation and tuning of wrinkled surface and modulation on nano-structured micro-granules has been discussed in this chapter. These granules possess enhanced surface area owing to the modulations which makes them useful for specific applications requiring a large contact area such as catalysis,[267-268] filtration,[269] sorption,[226] etc.

A mixture of two stable colloids was suitably chosen to demonstrate the effect of the interparticle interactions. The shape and surface charge of colloidal particles are two governing factors that are accounted for by the DLVO formalisms.[71] Other non-DLVO factors such as hydrophobicity and depletion interactions also significantly affect the interactions in a colloidal system.[39] A model system, comprising of an aqueous colloidal mixture of spherical silica nanoparticles (NS) with water-dispersible cylindrical carbon nano-tubes (CNT) was chosen to demonstrate the origin of anisotropic interactions and consequently the production of wrinkled granules. NS and CNT, being dissimilar with respect to shape and wettability, illustrates a contradictory behaviour during drying of the colloidal droplet. Moreover, depending on the polarity of these components, the dispersion exhibits dominance of attractive or repulsive DLVO potentials. In this chapter, the effect of these factors on the assembly process during drying vis-a-vis the control of the granular surface modulation has been illustrated.

5.2 Synthesis

The synthesis of single-walled carbon nanotube (SW-CNT) has been elaborated by Kim *et al.*[270] In short, non-covalently functionalized isolated single-walled CNTs were obtained by dispersing HiPco SW-CNTs in water by using a cationic surfactant having polymerizable counter-ions.[271] The surfactant monolayer was fixed permanently on the SW-CNTs by *in situ* free-radical polymerization of the counter-ions, followed by freeze-drying. Atomic force microscopy(AFM) revealed a radius of 2.5 nm and length of 500 nm of the CNTs. Polymerized SW-CNTs were then dissolved in water and were kept at vortex until the CNTs made a stable dispersion. This dispersion was then diluted with water to make CNTs of 0.1% and 0.05% by weight (50 mL each). The ζ-potential value of CNT was found to be -6.5 mV. LUDOX® HS-40, nano-silica suspension (ζ-potential = - 48mV), 2% by weight (in 50 mL water) was mixed with 0.1% and 0.05% CNT dispersions separately to make two 100mL bi-component dispersions. Similarly, LUDOX® CL nano-silica (ζ-potential = -44mV), 2% by weight (in 50 mL water) was mixed with 0.05% CNT to make another 100 mL bi-component solution. Thus three mixed dispersions, namely i) 0.05% CNT - 2% HS-40 ii) 0.05% CNT - 2% CL and iii) 0.1% CNT - 2% HS-40 were prepared. Each of the diluted dispersions was fed into spray dryer at a constant feed rate of 2 mL per minute under continuous stirring. The suspension is atomized into droplets with an average diameter of ~10 μm. Constant aspirator rate and inlet temperature of 130°C were maintained throughout the synthesis processes in each case. For easier reference, the nomenclature of the powder granules made according to the abbreviated name of the type of silica nanoparticles and the CNT concentration: H-0.1, H-0.05, and CL-0.05.

5.3 Structural characterization by FESEM

The granular morphologies are discernable from the FESEM micrographs in Fig. 5.1. H-0.1 and H-0.05 show distinct wrinkle-like modulation on the surface which is absent for CL-0.05. The left panel depicts the whole granules (Fig. 5.1 (a), (c), (e)) whereas the right panel lists their magnified surfaces at 150kX magnification (Fig. 5.1 (b), (d), (f)). It is perceivable from the right panel that granules with HS-40 silica (H-0.1 and H-0.05) bear prominent wrinkle-like roughness on the surface.

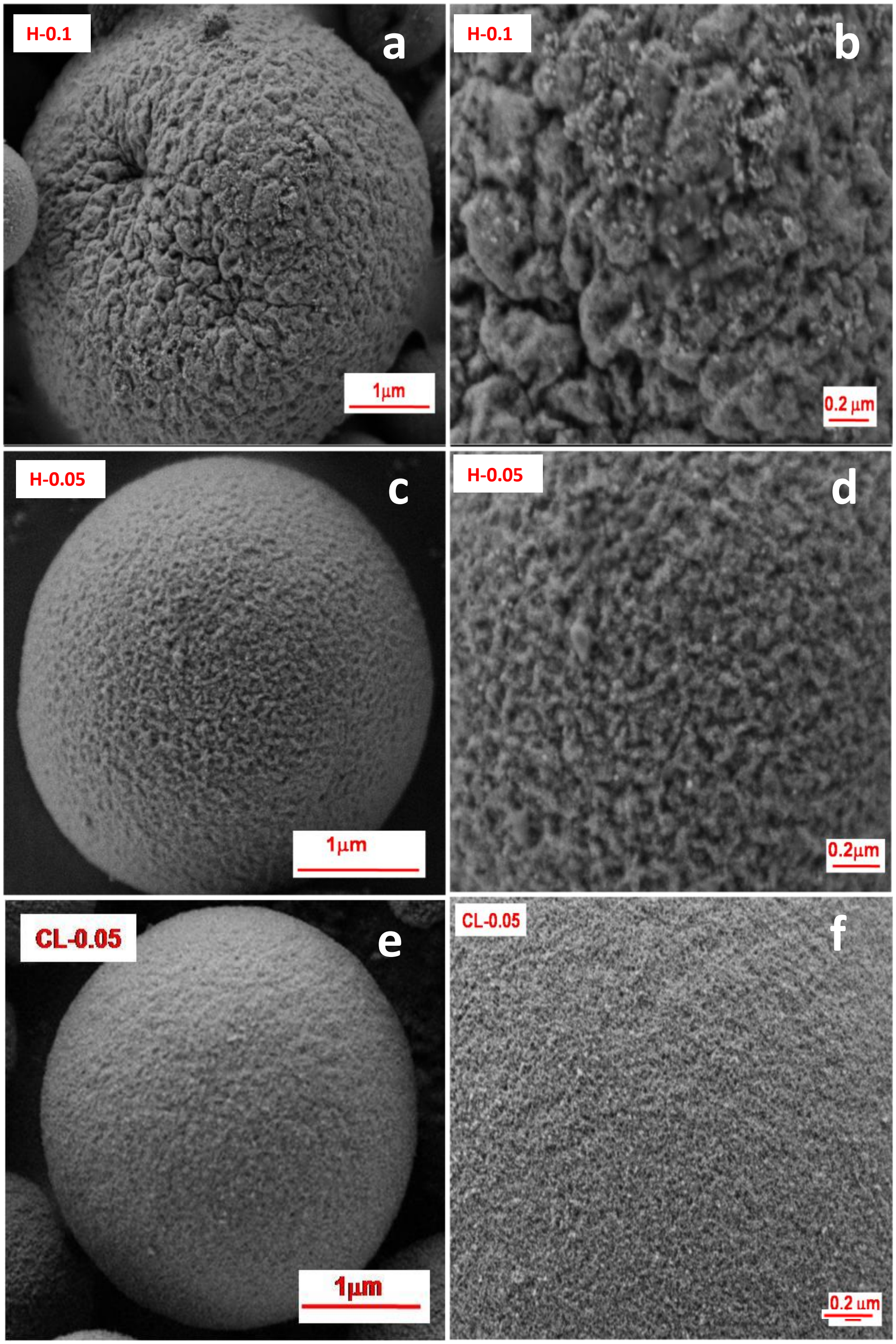

Fig. 5.1 FESEM micrographs showing the morphology of granules. Left panel **(a)**, **(c)**, **(e)** shows the overall morphology. Right panel **(b)**, **(d)**, **(f)** shows the zoomed view of the surface.

The surface roughness of the granules as perceived from Fig. 5.1 (b), (d), (f) were represented as normalized gray-scale intensity variation as a function of length in Fig. 5.2(a). The intensity fluctuations were quantified in terms of wavelength and amplitude of the intensity plots. Wavelength corresponds to the extent between two consecutive bright or dark regions, whereas amplitude denotes the brightness or the peak intensities. Hence, an estimate of the comparative surface roughness for the three cases can be made by comparing the intensity fluctuations. For H-0.1, the fluctuations are more pronounced, as perceived by the distinct bright and dark regions on the FESEM micrographs (Fig. 5.1(a), (b)). The gray-scale intensity plot for H-0.1 is denoted in red in Fig. 5.2(a). An average wavelength for the fluctuation was found to be ~60 nm along with the largest average amplitude as compared to the other granules. In contrary, the amplitude for CL-0.05 (denoted by green) is nearly constant (without any prominent fluctuation) indicating the smoother surface of the granules. H-0.05 has a profile lying midway between the above two cases. Inset of Fig. 5.2(a) depicts a zoomed view of the intensity plot to provide a further clearer picture of the comparison of fluctuations. Thus when compared at the same magnification, the surface of H-0.1 show maximum roughness, followed by H-0.05, whereas CL-0.05 has negligible surface modulation.

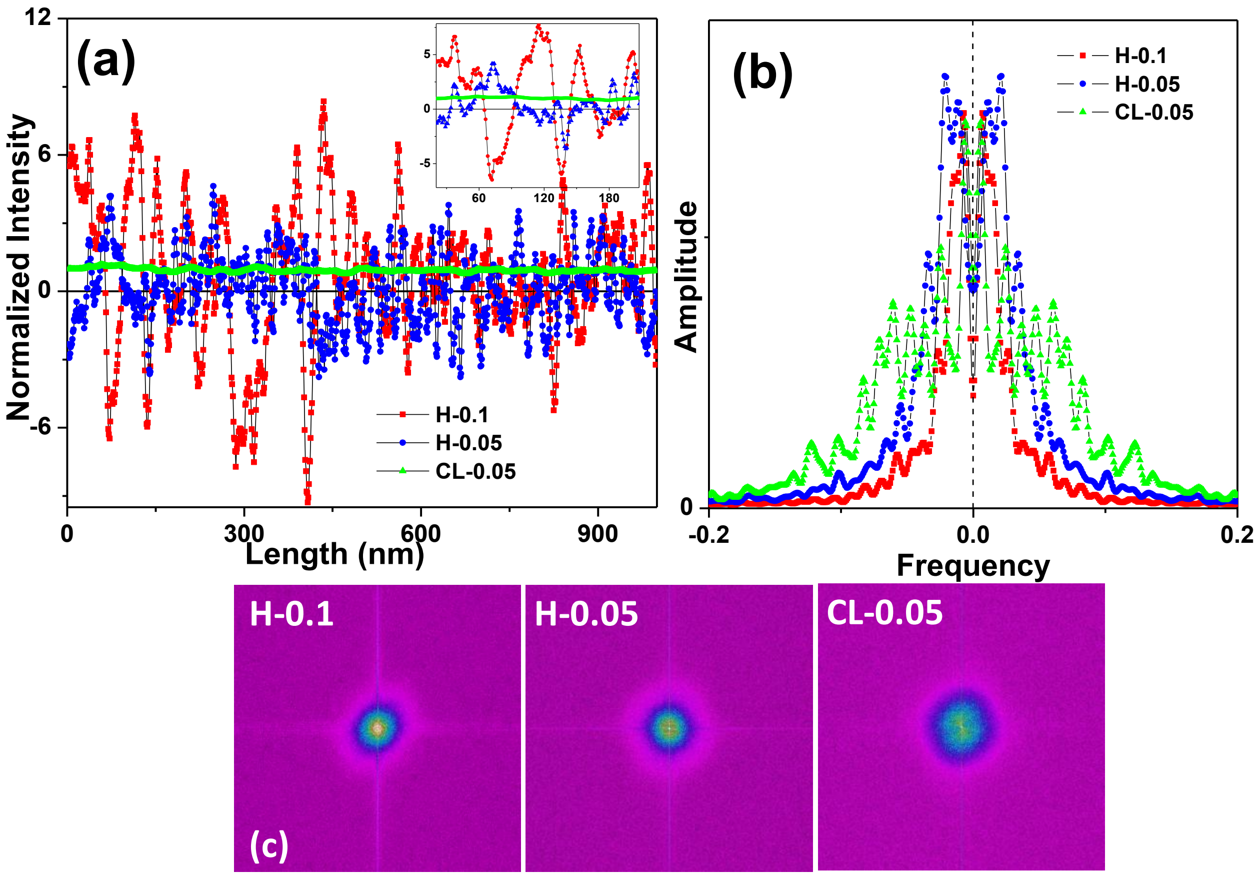

Fig. 5.2 (a) Spatial gray-scale intensity plot of the granular surface **(b)** Frequency spectra of the gray-scale variation **(c)** 2D Fourier transformed images.

Fourier analysis of the zoomed images provides a further clearer idea about the extent of roughness on the granule. Fig. 5.2(b) depicts the Fourier spectra showing the distinct contribution of the frequency components of the gray-scale spatial intensity fluctuation obtained from the spectral decomposition of the zoomed micrographs (Figs. 5.1 (b), (d), (f)). The contribution of high-frequency components is found to be more for CL-0.05, whereas least for H-0.1. Thus, as per the Fourier principle,[258] the surface modulation in case of H-0.1 is extended over a larger length scale. Fig. 5.2(c) compares the 2D Fourier transformed image in three cases. It is evident that the spread of the halo is more for CL-0.05 owing to the small scale modulation in contrary to H-0.1 where the halo is much more localised at the centre.

5.4 Mesoscopic structure characterization by SAS

The mesoscopic structure of the composite granules and the inter-particle correlation among the components were quantified using SAS. The higher q range was accessed by SAXS which probed the length sizes from ~3-60 nm which includes the nanoparticle sizes and the CNT radii.[270] SAXS measurements were performed for the colloidal suspension as well as for the granules. The SAXS profiles for three types of granules are depicted in Fig. 5.3(a-c). SAXS profiles for raw CNT in solid form and dispersed in solution are compared in Fig. 5.3(d). The scattering intensity from composite granules may be approximated to be the cumulative contribution of scattering from the two different length scales as given in Eq. 3.1. The cross-terms of the intensity can be neglected because the involved length scales are significantly wide-spread (e.g. individual NS particle radius ~ 8 nm, CNT length ~500 nm while the granule radius > 2500 nm). Thus, following Eq. 3.1, the total scattering intensity of the composite $I_{total}(q)$ may be represented as,

$$I_{total}(q) = I_{comp}(q) + I_g(q) \tag{5.1}$$

Scattering intensity $I_g(q)$ is the whole granular contribution whereas $I_{comp}(q)$ is the contribution from the components of the composite granule, i.e., CNT as $I_{CNT}(q)$ and silica nanoparticles as $I_{NS}(q)$, which can be written as $I_{comp}(q) = I_{CNT}(q) + I_{NS}(q)$. Under local mono-disperse approximation,[182]

$$\begin{aligned}
I_g(q) &= C_g \int_0^\infty P_g(q,r) v_g^2(r) D_g(r)\, dr \\
I_{CNT}(q) &= C_{CNT} \int_0^\infty P_{CNT}(q,r) v_{CNT}^2(r) D_{CNT}(r) S_{CNT}(q,r)\, dr \\
I_{NS}(q) &= C_{NS} \int_0^\infty P_{NS}(q,r) v_{NS}^2(r) D_{NS}(r) S_{NS}(q,r)\, dr
\end{aligned} \tag{5.2}$$

where C_{CNT}, C_{NS} and C_g are q independent scale factors related to corresponding scattering contrast and number density for CNT, silica nanoparticles and the granules, respectively. v_x represents respective particle volume. $D_x(r)$ represents the size distribution function. $S_x\,(q,r)$ represents the inter-particle structure factor. $P_x\,(q,r)$ represents form factors given by,[164]

$$
\begin{aligned}
P_{NS}(q,r) &= \frac{9\left[\sin(qr) - qr\cos(qr)\right]^2}{(qr)^6} \\
P_{CNT}(q,r) &= \int_0^{\pi/2}\left[\frac{2J_1(qr\sin\alpha)}{qr\sin\alpha}\,\frac{\sin\left(qL\cos\left(\alpha/2\right)\right)}{qL\cos\left(\alpha/2\right)}\right]^2 \sin\alpha\, d\alpha
\end{aligned}
\qquad (5.3)
$$

$P_{NS}(q,r)$ represents the form factor for spherical silica nanoparticles whereas $P_{CNT}(q,r)$ represents the corresponding form factor for the cylindrical CNTs. L is the length of the cylinder and $J_1(x)$ is first order Bessel function. Based on AFM and scattering results,[270] a monodisperse $D_{CNT}(r)$ was considered with length (L) 500 nm and radius (r) 2.5 nm. Standard log-normal size distribution[191] function was considered for NS ($D_{NS}(r)$) as well as the granules ($D_g(r)$).

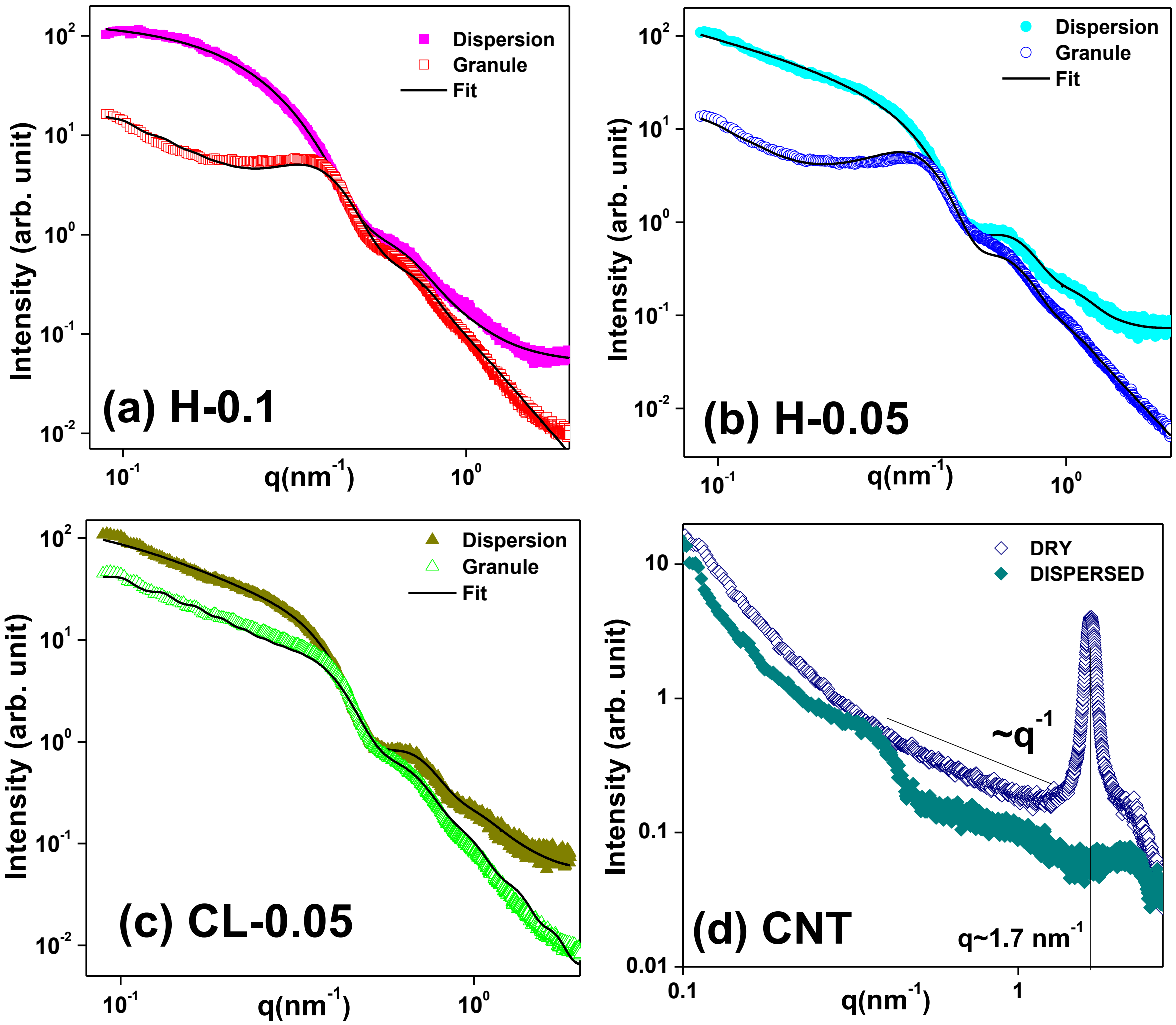

Fig. 5.3 Comparison of SAXS profiles, before and after spray drying: **(a)** H-0.1, **(b)** H-0.05, **(c)** CL-0.05, **(d)** CNT.

Fig. 5.3(a-c) depict the differences in scattering profiles between NS and CNT in dispersion form and after granulation for each of the cases. A correlation peak gains prominence in the scattering profiles of the granules for H-0.1 and H-0.05 which is absent in the profiles of the corresponding dispersions (Fig. 5.3 (a), (b)). The peak position at ~ 0.36 nm^{-1}, corresponding to a characteristic length of 18 nm, represents the inter-nanoparticle distances in the granule. The parameters obtained from the model fitting are tabulated in Table 5.1. The average nanoparticle size is ~ 8 nm. It is observed from the analysis that nanoparticles exhibit sticky hard sphere correlation in the granule. The fitting parameters are provided in Table 5.1. MSANS profiles of the composite granules (Fig. 5.4) reveal characteristic radii of the CNTs which is much larger than the radii obtained from AFM[270], due to the bundling of CNTs in the granules. H-0.1, which has a higher concentration of CNT, exhibit a larger bundle size compared to H-0.05. CL-0.05, on the other hand, shows the least bundling. The mechanism of bundle formation during evaporation-induced assembly and consequently the origin of surface wrinkles have been explained in detail in the later sections of this chapter. Interestingly, the corresponding length of CNTs in all three cases are found to be ~500 nm (Table 5.1), suggesting that the CNT does not bend or break during compressive assembly.

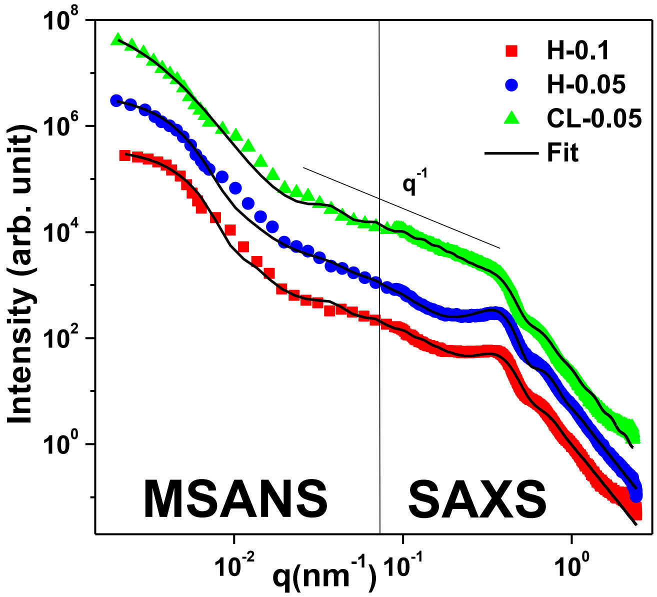

Fig. 5.4 Combined MSANS and SAXS profiles over the whole accessible q-range.

Composite	NS (From SAXS)		CNT bundle (From MSANS)	
	Median Radius (nm)	Packing Fraction	Dimension (nm)	
			Bundle radius	Length
H-0.1	8.25	0.64	18.2	500
H-0.05	8.00	0.60	15.0	455
CL-0.05	8.00	0.60	8.60	454

Table 5.1 Fitted parameters from SAXS/MSANS profiles of silica-CNT granules.

It is interesting to note that the SAXS profile of CL-0.05 (Fig. 5.3(c)) does not show any distinct correlation peak. Moreover, analysis of the SAXS profile of the CL-CNT dispersion revealed a characteristic packing fraction and stickiness for CL nanoparticles in the solution. This is because, in this case, CNT and CL nanoparticles posses opposite polarities. Hence attraction between the CL particles and CNT cause lesser bundling of the CNTs as NS now tend to adhere to the CNT surface. Therefore, in contrary to H-0.1 and H-0.05, here the bundle radii are lesser (Table 5.1). The details of the assembly process have been illustrated in section 5.5 of this chapter. It will be demonstrated that the difference in the assembly process in case of granules with HS-40 NS (-ve charge) and CL NS (+ve charge) is, in fact, the cause of the topographical difference of the granular surface.

Fig. 5.3(d) shows a prominent peak at q ~1.6 nm^{-1} in the scattering profiles of virgin CNTs, which is absent in case of scattering profile of CNT dispersion. This characteristic length scale corresponds to the diameter of the CNTs which is calculated to be 5.0 nm ($=2\pi/q$). This value corroborates well with that obtained from AFM as reported by Kim *et al.*[269] The combined MSANS-SAXS scattering profiles reveal a negative slope of -1 corresponding to the 1D CNTs in the granules (Fig. 5.4).[163]

5.5 Origin of surface wrinkles

So far in this chapter, it has been established from FESEM and SAS that granules having similarly charged NP and CNT display a wrinkled exterior (H-0.1 and H-0.05) whereas granules with opposite polarity of NP and CNT are smoother. Moreover, the extent of wrinkling in the first case is more when the CNT concentration is more (H-0.1). At this stage, it can be inferred from these observations that the granular topology is essentially governed by the interparticle interactions between the assembling nanostructures. Thus, a step-wise assessment of the evaporation-induced self-assembly process starting from the initial dispersion is indispensable to evaluate the changes in the interparticle interactions leading to wrinkled granules.

Literature reveals the various types of interparticle interactions in a colloidal dispersion. As mentioned in Chapter 1, section 1.3.1, for a suspension comprised of charged colloidal particles, long-ranged repulsive electrostatic force and short-ranged attractive van der Waal (VW) force constitutes the DLVO potential. When the attractive forces dominate, the particles flocculate and dispersion is unstable. However, when the repulsive forces dominate, owing to the similar charge of the suspended particles, the solution is stable. From the DLVO viewpoint, each of the dispersion can be deconstructed into the individual contributory attractive and repulsive components.

The net DLVO interaction energy between two colloidal particles (W_{DLVO}), as a function of inter-particle distance (d), is the resultant of the attractive van der Waals (W_{VW}) and repulsive electrostatic double layer (W_{DL}) interaction energies given by,

$$W_{DLVO}(d) = W_{VW}(d) + W_{DL}(d) \tag{5.4}$$

For identical spherical NS particles,[39] W_{DLVO} is given by,

$$W_{NS}(d) = -\frac{A_{NS}R_{NS}}{12d} + \frac{R_{NS}e^{-\kappa d}\Psi}{2} \tag{5.5}$$

where A_{NS} is the Hamaker constant, R_{NS} is the radius of the spherical particle; κ^{-1} is the Debye length in the solvent, interaction constant Ψ is given by, $\Psi = 64\pi\varepsilon_0\varepsilon\left(\frac{k_BT}{e}\right)^2 tanh^2\frac{e\zeta}{4k_BT}$ where ε_0 is the permittivity of free space (8.85x10^{-12} C^{2}N^{-1}m^{-2}), ε is the dielectric constant (78.4) of the water at room temperature T= 298 K, k_B is the Boltzmann constant (1.38x10^{-23} JK^{-1}). Electronic charge 'e' (1.6x10^{-19} C), ζ being the electric double-layer potential or ζ-potential. Similarly, for cylindrical particles,[39] with radius R_{CNT} and length L_{CNT} and Hamaker constant A_{CNT}, the total energy (W_{CNT}) is represented as,

$$W_{CNT}\left(d\right)=\left(-\frac{A_{CNT}\sqrt{R_{CNT}}}{24d^{1.5}}+\frac{e^{-\kappa d}\Psi}{2}\sqrt{\left(\frac{\kappa R_{CNT}}{\pi}\right)}\right)L_{CNT} \tag{5.6}$$

However in the present case, along with the two above-mentioned DLVO interactions, namely W_{NS} (among silica nanoparticles) and W_{CNT} (among CNTs), there exists a third type of interaction between the NS and CNT which depends on both**,** component geometry and surface charge. The attractive part (VW interaction) is represented as,[272]

$$W_{VW}^{NS-CNT}\left(d\right)=-\frac{4AR_{NS}^{3}}{3\pi}\int_{V_{CNT}}\frac{dV_{CNT}}{(r^{2}-R_{NS}^{2})^{3}} \tag{5.7}$$

where 'r' is the distance between an arbitrary point 'P', considered in the cylinder and the centre of the sphere, 'O' (Fig. 5.5). In cylindrical coordinates, the volume element dV_{CNT} is given by '$\rho d\rho d\phi dz$' and

$$r^{2}=\left(d+R_{NS}+R_{CNT}+\rho\cos\phi\right)^{2}+\left(\rho\sin\phi\right)^{2}+z^{2}$$

where 'ρ' is the radial distance of 'P' from the z-axis, 'ϕ' is the azimuthal angle and z is the height at which the considered point is situated with respect to the origin plane as shown below in Fig. 5.5. Substituting r^2 in Eq. 5.7,

$$\begin{aligned}W_{VW}^{NS-CNT}\left(d\right)&=-\frac{16A}{3\pi}R_{NS}^{3}\cdot\\&\int_{0}^{\pi}d\phi\int_{0}^{R_{CNT}}\rho d\rho\int_{0}^{L_{CNT}}\left[\left(d+R_{NS}+R_{CNT}+\rho\cos\phi\right)^{2}+(\rho\sin\phi)^{2}+z^{2}-R_{NS}^{2}\right]^{-3}dz\end{aligned} \tag{5.8}$$

which is the functional form of interaction energy due to attractive van der Waal force.

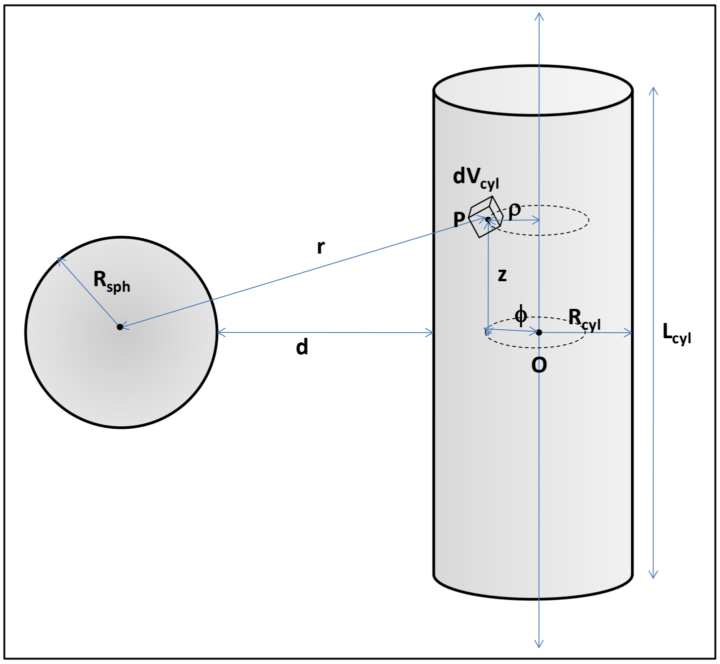

Fig. 5.5 Schematic representation of the defining parameters of sphere and cylinder. Sphere having a radius 'R_{NS}' and cylinder has a radius of 'R_{CNT}'. The sphere is separated from the cylinder by a distance'd'. The volume element in the cylinder is denoted as 'dV_{CNT}'. The separation distance between the volume element and the centre of the sphere is denoted as 'r'. The geometry is described with cylindrical coordinates (ρ, ϕ, z). The radial distance 'ρ' is the Euclidean distance from the z-axis to the volume element. The azimuth 'ϕ' is the angle between the reference direction and the line from the origin to the projection of the volume element on the plane. The height 'z' is the distance from the volume element to the origin plane.

The electric double layer interaction energy between sphere and cylinder, as a function of inter-particle distance, was evaluated by Li *et al.*,[272]

$$W_{DL}^{NS-CNT}\left(d\right)=D_1\left[\begin{array}{l}\left\{\int_0^{\pi/2} d\theta \int_0^{R_{CNT}} F_1\left(\kappa,x\left(d,y,\theta\right)\right)ydy\right\}+\\ \left\{\int_{R_{CNT}}^{R_{NS}} ydy \int_0^{sin^{-1}\left(R_{CNT}/y\right)} F_1\left(\kappa,x\left(d,y,\theta\right)\right)d\theta\right\}\end{array}\right] \qquad (5.9)$$

where, $D_1 = 4\varepsilon_0\varepsilon\kappa\zeta_{NS}\zeta_{CNT}$ and ζ_{NS} and ζ_{CNT} represent the ζ-potential of spherical and cylindrical particle respectively; $F_1(\kappa,x) = cos\,ech\kappa x + D_2(1-coth\,\kappa x)$ in which, D_2 and $x(d,y,\theta)$ are dimensionless quantities given by $D_2 = \frac{\zeta_{NS}^2 + \zeta_{CNT}^2}{2\zeta_{NS}\zeta_{CNT}}$ and

$$x(d,y,\theta) = d + R_{NS} - \sqrt{R_{NS}^2 - y^2} + R_{CNT} - \sqrt{R_{CNT}^2 - y^2\sin^2\theta}.$$

The total interaction energy is the sum of the two contributions is therefore,

$$W_{NS-CNT}(d) = W_{VW}^{NS-CNT}(d) + W_{DL}^{NS-CNT}(d) \tag{5.10}$$

The variation of total interaction energy $W_{NS\text{-}CNT}$ are plotted with distance'*d*' for the individual dispersions in Fig. 5.6.

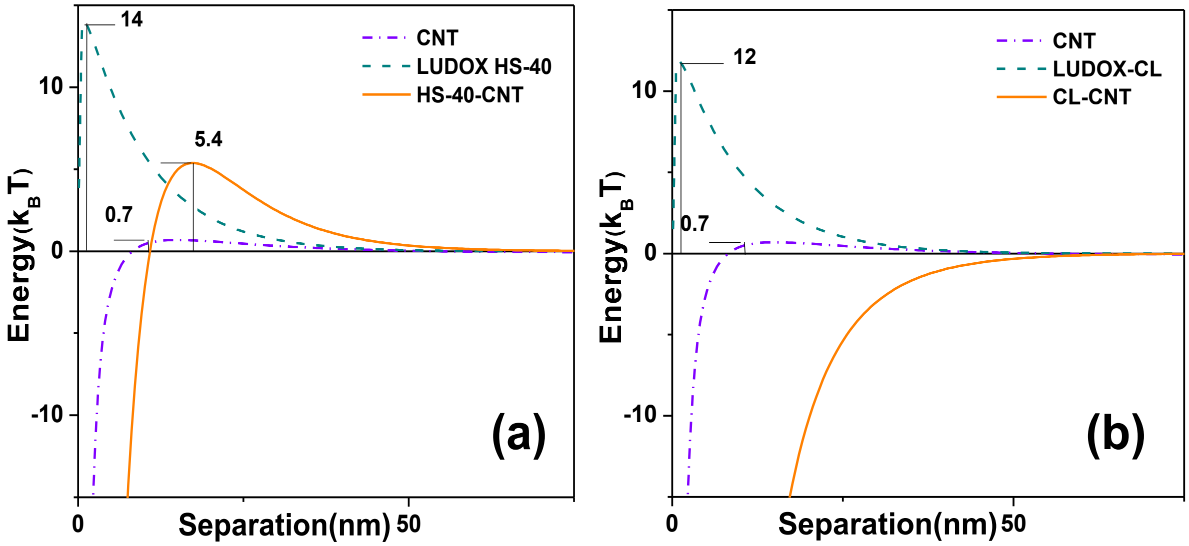

Fig. 5.6 DLVO potential plots for **(a)** HS-40 and CNT suspension, **(b)** CL and CNT suspension.

In the dispersion comprising of CNT with HS-40 (Fig. 5.6(a)), both the components have a negative ζ-potential (CNT = -6.5 mV and HS-40 = -48 mV). The individual plots are W_{NS} for silica nanoparticles, W_{CNT} for CNT and $W_{NS\text{-}CNT}$ for interaction between the corresponding NS and CNT. The interaction energy is expressed in terms of k_BT. 'A_{NS}' for silica is 0.8 x 10^{-20} J, the average radius R_{NS} (for HS-40 as well as CL silica) being 8 nm as obtained from SAS, κ^{-1} has been calculated to be ~ 9.6 nm, at room temperature.[39] Similarly, for CNT A_{CNT} is 0.85 x 10^{-20} J[272] and κ^{-1} is ~16.4 nm.[39] R_{CNT} and L_{CNT} is taken as 2.5 nm and 500 nm respectively, as obtained from AFM.[270] The DLVO potentials, in this case, are repulsive. Silica records the highest barrier height of 14 k_BT whereas CNT is barely 1 k_BT. The repulsive barrier between NS and CNT lies in between the two at 5.4 k_BT. For dispersion comprising of CL and CNT, the height for CL is 12 k_BT, depicted in Fig. 5.6(b). CL has a ζ-potential value of +44mV whereas CNT has a negative ζ-value of 6.5 mV. Hence here the net DLVO potential is attractive.

On the basis of these interaction potentials, the colloidal dispersion either remains stable or flocculates. For the case of HS-40 and CNT, the dispersion is stable owing to the repulsive barriers whereas, CNT and CL experience attractive interactions. Hence, NS being smaller in size (8 nm radius) compared to the CNT length and oppositely charged, adheres to the CNT surface. Analysis of SAXS profiles for the dispersion revealed a sticky hard sphere correlation between NS with a stickiness coefficient of 6.6, which denotes proximity of NS to each other on the surface of CNT. Such correlation between NS is absent for the dispersions of HS-40 and CNT. Thus, SAXS provides evidence of coating of CNT strands with NS for oppositely charged CL and CNT. Fig. 5.7 schematically depicts the attraction between CL and CNT, resulting in CL-coated CNT strands in the dispersion.

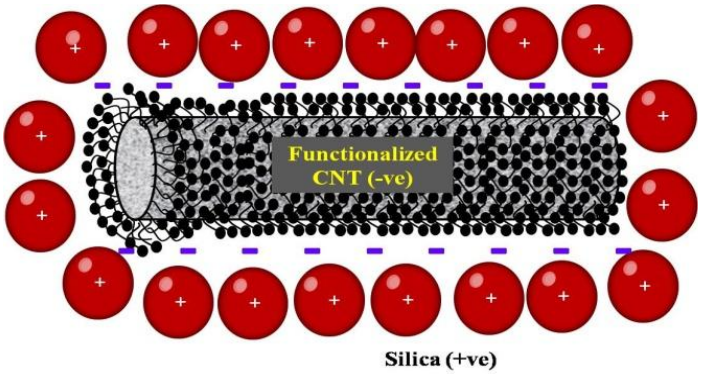

Fig. 5.7 Interaction between CL and CNT in suspension.

During drying, the components undergo diffusion the coefficient of which can be calculated by the Stokes-Einstein equation, $D_{sphere} = \frac{k_B T}{6\pi\eta r}$ where k_B is the Boltzmann constant (1.38 x 10^{-23} JK^{-1}), η is the solvent viscosity, r is the radius of the particle. For a silica nanoparticle of typically ~8 nm radius (r) at a drying temperature of 130°C, η of water being 0.21 x 10^{-3} Pa.s, D_{NS} is calculated to be 17.3 x 10^{-11} m^2s^{-1}. For cylindrical particles with large aspect ratio, P where $P = \frac{L}{2r}$, diffusion coefficient is given by,[273] $D_{cylinder} = \frac{1}{3} \cdot \frac{k_B T \ln P}{\pi\eta L^3}$. In the present case considering r and L to be 2.5 nm and 500 nm respectively,[270] D_{CNT} is calculated to be 2.55 x 10^{-11} m^2s^{-1}. Thus as drying commences in the droplet, the particles undergo directed diffusion where CNT diffuses slower than NS.

It is worth mentioning that indeed the surface features of the granule are governed by the type of particle at the surface which is being exposed to the drying air. FESEM micrograph in Fig. 5.1 depicts that H-0.1 granules are more wrinkled, having more dents on the surface compared to H-0.05. The difference in the topology is apparently due to the difference in concentration of CNT in the granules. It should be kept in mind that silica nanoparticles are hydrophilic.[274] Water-dispersible functionalized CNTs are also hydrophilic due to the layer of polymerizable surfactant group (CTVB) on its surface.[270] Thus, during evaporation of water from the droplet, both CNT and NS undergo outward hydrophilic motion, following the outflow of water through the air-water interface.[269] With the commencement of evaporation in the droplet, capillary forces emerge, initiating the assembly among the particles. Capillary forces between two particles are shape-dependent. For two spherical nanoparticles, the capillary force is of the order of 10^{-11} N given by Eq. 1.6, which is equivalent to the energy of the order of 10^{-20} J or ~10^{3} k_BT. For CNTs, the order of magnitude is also similar.[187] Hence, the effective capillary energy for interlocking of particles is large enough to overcome the DLVO barrier (few k_BT). However, the chronology of the assembly will be dictated by the barrier height.

For the case of similar polarities of NS and CNT (dispersion with HS-40 silica nanoparticles), the assembly process is sequential. The barrier height for inter-CNT potential is the least among the three with the peak reaching up to ~0.7 k_BT. Thus at the start, this repulsive barrier gets overpowered and CNT strands bundle among themselves. The bundling process is random owing to the quick drying time scale of observation and hence the formed bundles are irregular and polydisperse. Bundling is followed by the assembly between NS and CNTs (barrier height ~5.4 k_BT). It is to be mentioned that due to the prior bundling of the CNTs, the NS accumulation occurs on these bundles. Finally, the repulsive barrier (~14 k_BT) between HS-40 nanoparticles is overcome, leading to self-assembly and adhering on the NS-coated CNTs as well, forming composite bundles. These composite bundles are large and irregular in shape, owing to the polydispersity in shape and size of the CNT bundles. Composite bundles are slow to diffuse and mostly get jammed at the surface. The irregular bundles enclose gaps and channels in between which lends a rough and wrinkle-like appearance to the surface. Top half of Fig. 5.8 schematically depicts the above-mentioned assembly process. For H-0.05, the concentration of

CNT is lesser (0.05%) than the previous case (0.1%) thus CNT bundles are fewer in number. Therefore the surface irregularity is reduced than the previous case. A rough estimate of the granule and composite bundle size were made from Fig. 5.1(b) and (d) using ImageJ. For H-0.1, the average size of granules is ~6 μm and size of a typical composite bundle is ~250 nm whereas H-0.05 has an average size of ~3 μm and a bundle size of ~120 nm on the surface. As the NS concentration is identical (2%) in both the case, the bundle size essentially depends on the CNT concentration. Thus, the surface roughness and the overall granular morphology depend on the relative concentration and polarity of the components

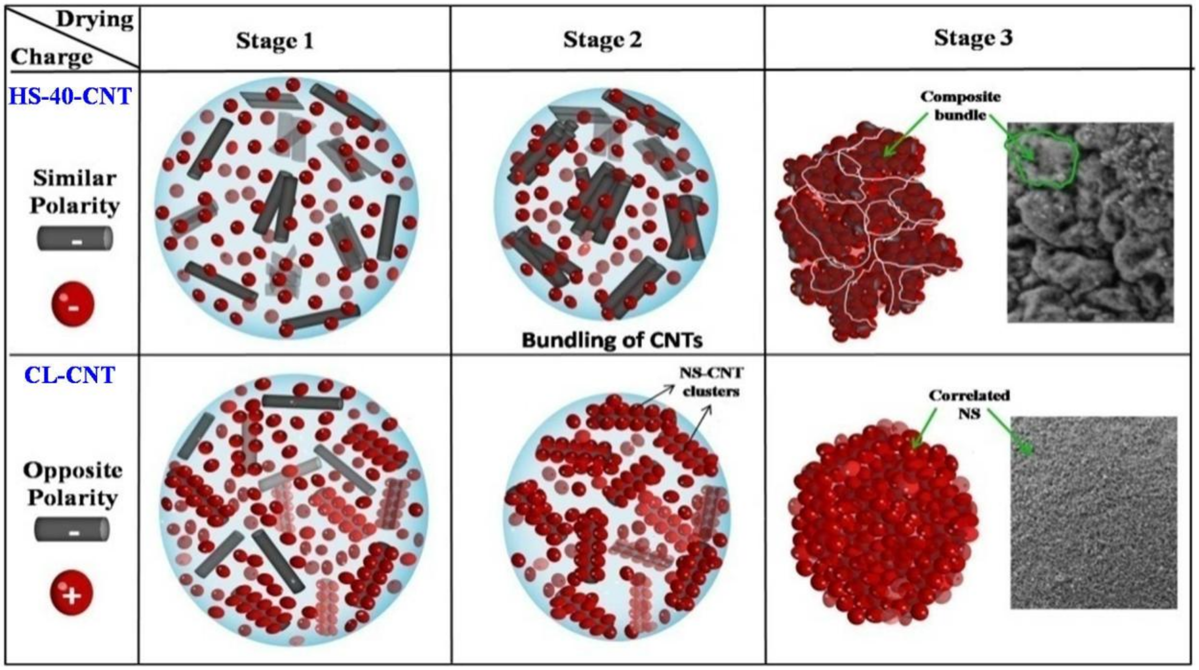

Fig. 5.8 Schematic representation of the drying process of a colloidal droplet comprised of **TOP**: HS-40 and CNT and **BOTTOM**: CL and CNT.

For CL-CNT dispersion, attractive interactions exist between the components owing to the opposite ζ-potential polarities (-6.5 mV for CNT and +44 mV for CL nano-silica). The DLVO-potential plots are provided in Fig. 5.6(b). There is a net attractive interaction between NS and CNT leading to attachment of NS on CNT surface (schematically depicted in Fig. 5.7).

NS, being much higher in concentration than CNT, is in excess in the dispersion after an optimum amount of NS attaches to the CNT surface. These NS units remain charge separated. During evaporation, assembly takes place between the NS-coated CNTs and also among individual excess NS. NS-coated CNTs are bulkier in size hence undergo slower diffusion than individual NS. With the commencement of drying and outflow of water, the excess NS diffuses faster to the evaporation front and gets jammed forming a relatively smooth surface of the granules. The bottom half of Fig. 5.8 illustrates this process. Although the FESEM micrograph for CL-0.05 granules does not show any distinct signature of CNT, SAS studies earlier confirmed the presence of CNT by the characteristic q^{-1} slope.

The chemical composition of the granules can also be obtained from Energy Dispersive X-ray (EDS) spectroscopy. Fig. 5.9 depicts the EDS spectra for the granules. Distinct peaks for carbon (C), silicon (Si) and oxygen (O) are observed for all the three cases. For CL-0.05, an extra peak is observed corresponding to aluminium which is due to the alumina coating on LUDOX CL nano-particles which imparts its positive charge.

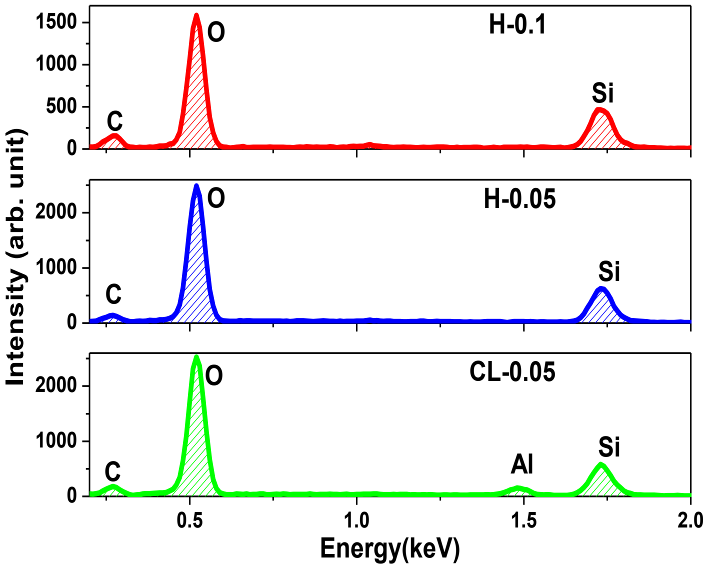

Fig. 5.9 Energy dispersive spectra for the granules.

5.6 Raman spectral measurements

Raman spectroscopy measurements were carried out for elemental analysis and understanding the modifications of various frequency modes of the granule constituents, in particular for the CNTs. It is to be noted that the granules are formed through compressive stress by the effect of capillary forces during fast evaporation. Thus, the components are in a jam-packed environment. Such close proximity in a compressive environment may modify their molecular vibrational modes of the components.[275] Raman spectroscopy is a non-destructive characterization technique which investigates the change in the vibrational modes of the components. Raman measurements were carried out using 532 nm laser. Backscattered light was analyzed using a home-built 0.9 m single monochromator, coupled with an edge filter and detected by a cooled CCD.

The alteration of vibrational characteristics of isolated CNT, when compared with CNT in the micro-granules, is elucidated in Fig. 5.10. It should be mentioned that for SWCNTs, there are three distinct Raman modes, namely, the G band (around 1580 cm^{-1}), the D mode (around 1350 cm^{-1}) and the radial breathing mode (RBM)[276] (frequency ν_{RBM} in the range of 100-500 cm^{-1}). G and $G^{/}$ peaks in G band corresponds to the in-plane vibrations along the tube axis and circumferential direction respectively. D mode corresponds to the structural defects in nano-tube. It is evident that in the present case, the position of D (1325 cm^{-1}), G (1580 cm^{-1}) and $G^{/}$ (1532 cm^{-1}) peak for CNT remain unchanged in all the cases. RBM is the bond-stretching mode for which all the carbon atoms move coherently in the radial direction.[276] Therefore, any change in frequency of this mode signifies the extent up to which the CNT can radially stretch. In other words, the effect of external compression on the nano-tube will be depicted by the changes in this mode. Fig. 5.10 shows that for CNT, a prominent ν_{RBM} appears at 270 cm^{-1}. However, for the composite granules H-0.1 and H-0.05 a prominent second RBM peak arises on the lower frequency side (220-240 cm^{-1}). Thus, CNT in composites have non-uniformity in radial breathing of the nanotubes. In case of composites with HS-40, the CNTs are bundled, thus the effective compression on a CNT is much more because of the presence of other CNTs at its proximity. Hence the radial stretching is compromised such that CNTs "breathe" slower in a confined environment. In contrast, in CL-0.05, the second RBM peak is not pronounced. As explained earlier, in this case, CNT bundling is lesser, unlike the previous case. Hence, the restriction on the "breathing" of the CNT is also less.

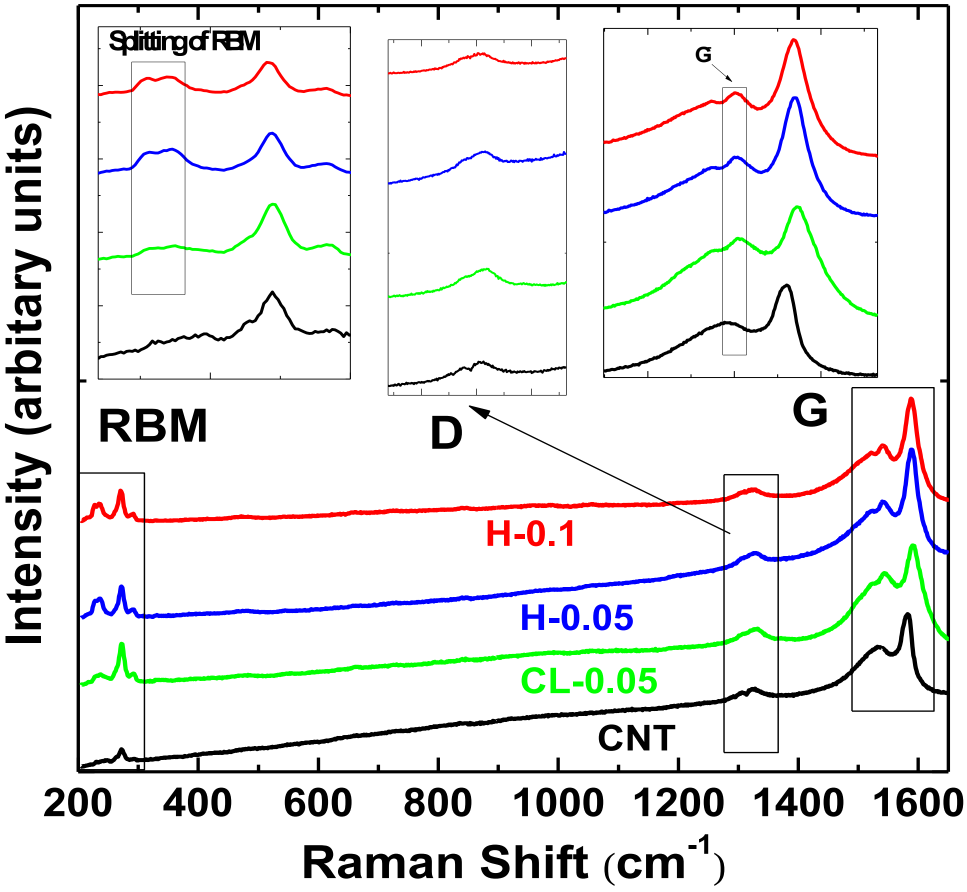

Fig. 5.10 Raman spectra for the composite granules, compared with that for CNT.

5.7 Evaluation of granular porosity

Preliminary observation by FESEM showed that H-0.05 and H-0.01 have dark crevasses on the surface, owing to the voids between the jammed composite bundles. As discussed earlier, the NS encloses spaces in between them. Moreover, the internal hollowness of the CNTs also contributes to the total empty space in the granule. Thus the investigation of the porosity is indeed necessary to harness the full potential of these granules for various application-based utilizations. Porosity, in terms of specific surface area and average mesopore radius, was quantified with the help of the gas adsorption technique of BET.

Fig. 5.11 depict the experiment results obtained from BET. In all of these plots, CL-0.05 shows visibly different functionality as compared with the other two composites. The differential mesopore volume distribution is shown in Fig. 5.11(a). The average mesopore radius is found to be ~3 nm for all three. Fig. 5.11(b) depicts the cumulative volume distribution for the composites. CL-0.05 is found to have significantly smaller cumulative mesopore volumes and monolayer volume than the other two, depicting the lesser number of accessible pores in this case. Adsorption-desorption isotherms are shown in Fig. 5.11(c). The hysteresis isotherms of CL-0.05 have lower saturation level of the adsorbed volume. This suggests that fewer pores are accessible by the adsorbed gas. The numerical values obtained from BET are given in Table 5.2. H-0.1 accounts for the maximum porosity, as denoted by the high *C*-value and the specific surface area. Specific surface area for purely HS-40 granules has been reported earlier in Chapter 4 as ~80 m^2g^{-1}. In the present case, the area is found to have increased significantly (by ~ 64%) owing to the presence of CNTs, surface roughness and micro-channels in HS-40-CNT composite granules.

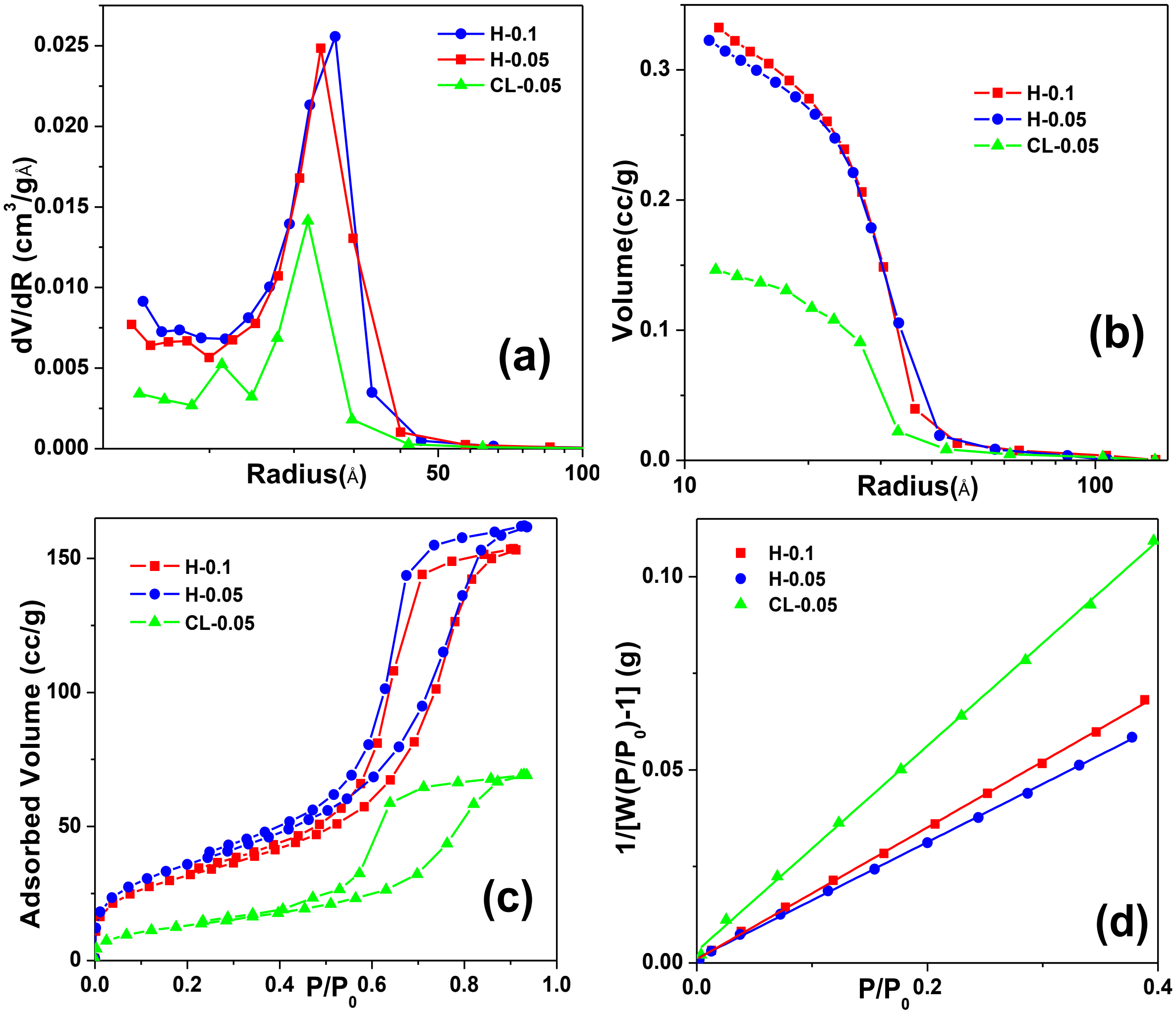

Fig. 5.11 (a) Differential mesopore volume distribution **(b)** Cumulative mesopore volume distribution for granules. **(c)** Adsorption-desorption isotherm as obtained from BET for the granules. **(d)** BET plots.

Composite	***C* value**	**Monolayer volume (cc/g)**	**Cumulative volume (cm^{3}g^{-1})**	**Average pore radius (nm)**	**Specific Surface Area (m^{2}g^{-1})**
H-0.1	164.0	25.5	0.332	3.0	131
H-0.05	74.7	30.1	0.32	3.0	111
CL-0.05	75.4	11.0	0.15	2.8	48

Table 5.2 Obtained parameters from BET measurements of silica-CNT granules.

5.8 Dye sorption behaviour

The significant gain in specific surface area has been the primary motivation in investigating the dye sorption characteristics of these granules. An aqueous solution of Methylene Blue (MB), 75ppm by weight was added to 0.1g of the powder. Sorption behaviour was monitored *in situ* using spectral analysis by JASCO V-650 UV-Vis spectrophotometer similar to the process discussed in Chapter 3.2. The change in the sorption spectra was recorded over a time period of two hours. Photographic evidence was also collected to monitor the visible colour change of dye solution due to sorption (Fig. 5.12). Raw CNT records nil sorption over the whole period of observation. The sorption by pure NS micro-granule for MB was ~85% in two hours. In the present case, the enhanced morphological characteristics of the composite granules accelerate the sorption significantly. UV-Vis absorbance spectra, given in Fig. 5.13 shows dye sorption of ~100% in two hours by H-0.05 and H-0.1, as recorded by the fall in the characteristic absorption peaks. In contrast, CL-0.05 records significantly low sorption (~8%) of cationic MB dye for the same time duration. This is because of the positive charge of CL nanoparticles. Moreover, the absence of pore channels, in this case, leads to a minimal available surface area (as evident from Table 5.2). Hence the morphological characteristics of the granules play a crucial role in dye sorption behaviour.

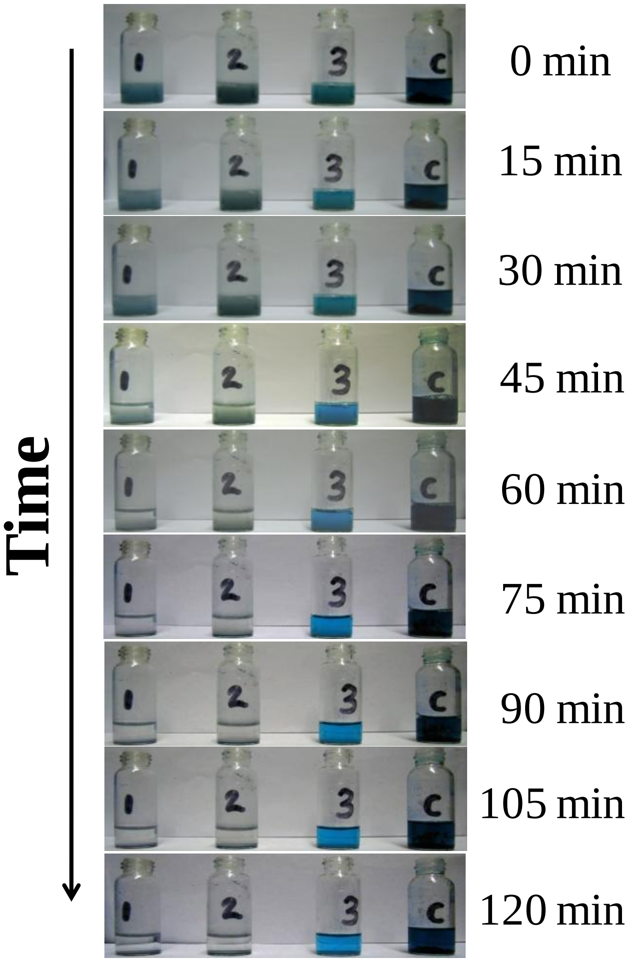

Fig. 5.12 Photographs of the vials over time, starting at t=0 min denoted by the addition of the granules to the dye solution to t=2 hr. The capsules take up the MB dye at settles at the bottom leaving a clear supernatant. The vials 1, 2, 3, C correspond to the case of H-0.05, H-0.1, CL-0.05 and CNT, respectively.

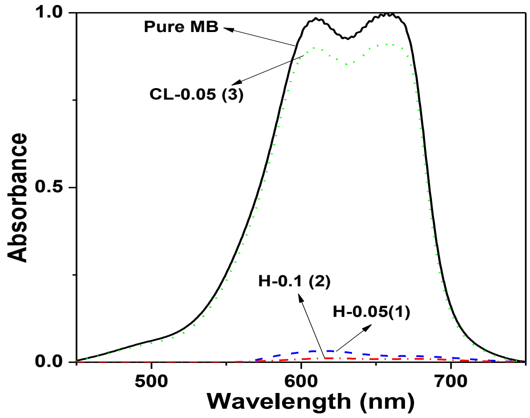

Fig. 5.13 UV-Vis sorption spectra after 2 hours compared with the spectrum of pure MB (Absorbance was normalized by the peak value of pure MB).

5.9 Conclusions

The role of interparticle interactions during evaporation induced self-assembly in colloidal droplets comprised of silica nanoparticles and CNT have been elaborated in this chapter. Dissimilarity in shape and polarity of the particles resulted in anisotropy of the interparticle interaction which manifested itself as prominent roughness of the granular surface. The concentration of CNT regulates the extent of wrinkling on the granular surface for like-polarity of the components. Sequential assembly takes place in this case according to the ascension of DLVO barrier heights. On the other hand, for opposite polarities of the components, the net DLVO interaction is attractive hence assembly is again random, yielding granules with smooth surfaces. A significant enhancement (64%) of the granular specific surface area was recorded for wrinkled granules over smoother ones. Rough granules exhibit faster sorption (99% in two hours) of Methylene Blue dye owing to the enhanced surface area.

Chapter 6: Summary and the path ahead...

This doctoral thesis attempts to provide a fairly comprehensive study of evaporation-induced self-assembly (EISA) process in colloidal droplets leading to the formation of nano-structured micro-granules. Understanding the droplet to granule transition requires a stepwise approach starting from the colloidal interactions under non-equilibrated drying conditions, which in turn governs the granular morphological aspects. The present thesis aims to encompass the different aspects of synthesis and characterization of nano-structured micro-granules, along with application-specific utilizations.

6.1 Summary

The motivation of this doctoral thesis was to fundamentally demonstrate EISA under intrinsic and extrinsic drying scenarios. The synthesis of nano-structured micro-granules by spray-drying process exercises facile control over the self-assembly and consequently their morphologies, extrinsically. This technique is versatile and encompasses a variety of colloidal systems and solvents. Easy up-gradation of the technique to large-scale production of powder granules is also possible.

The hierarchical length scales in the granule demand the utilization of two complementary characterization techniques, namely, Scanning Electron Microscopy (SEM) and Small-angle Scattering (SAS). SEM provides a direct image of the granules from which the overall shape and size could be perceived. SAS on the other hand quantifies the structure and correlation between the nanoparticles in the granule.

A stepwise approach has been adopted in this thesis; at the start, EISA for a primary colloidal dispersion of nano-silica has been demonstrated. The role played by the spray-drying temperature during self-assembly and consequently in determining the granular morphology has been demonstrated. At lower temperatures, spherical granules were obtained whereas, at higher temperatures, larger, doughnut-shaped hollow granules were produced. In short, the dependence of the morphology on an extrinsic experimental parameter has been looked into phenomenologically and evidenced with the help of complementary characterization techniques and simulations.

Owing to the unique morphological attributes of the granules (such as hollowness and porosity), their potentiality as sorbents for water-soluble Methylene Blue dye have been investigated. Sorption was shown to depend on the granular morphology. The importance of the chemical composition and molecular size of the dye molecules have also been established by comparative study with Rhodamine B dye.

The inherent granular porosity also facilitates the study of the behaviour of trapped water. Suppression of the freezing point (up to -50^{o}C) has been observed which can be utilized to indirectly map the granular porosity.[277]

The second issue that has been addressed in this thesis is EISA of a colloidal mixture droplet. The intrinsic role played by the inter-particle interactions during the self-assembly process and consequently, the determination of the granular shape have been investigated. Two studies have been carried out in this regard. The first one illustrates the effect of addition of emulsion (soft template) to homogeneous colloidal dispersion. A mixture of milk and nano-silica has been utilized as a model system to demonstrate the dependence of the concentration of soft component on the granular morphology. The relative polarity of the components is also proven to be a crucial parameter in governing the assembly and to determine the final morphology. The choice of milk as the soft component was advantageous as it allowed facile porogenation of mesopores and macropores in the granules through calcination of the powder granules in air. The porosity and specific surface area of the calcined porous granules are shown to depend on the initial milk concentration. Thus, efficient tuning of granular porosity was achieved by regulating the soft template concentration.

The second study elucidates the effect of anisotropic interactions on the EISA and the final granular morphology. A colloidal mixture comprised of particles having two different shapes (namely, spherical nano-silica and rod-like carbon nanotubes) have been chosen in this regard. Anisotropy in the interparticle interaction arises due to the shape and polarity dissimilarity of the components. Granules with prominent wrinkle-like modulations were realized from drying of droplet composed of similar polarity of the components. On the other hand, smooth granules were obtained for oppositely polarized components. The wrinkling, in the first case could be regulated by varying the concentration ratio of the colloidal components. Needless to mention here that wrinkling significantly enhances the specific surface area of the granules (by ~64%). Consequently, the dye sorption capabilities also improved drastically when compared with sorption in the previous case.

6.2 Future Outlook

Synthesis of next generation of materials for photonics, molecular electronics, drug delivery devices, sensors, etc. from nanometric building blocks has become convenient due to the advent of spontaneous and directed self-assembly processes. The versatility of spray-drying process is undeniable in this regard. Nonetheless, there are certain aspects of the process such as uniformity of the drying conditions, control over the granule size distribution and compatibility of raw materials with the drying conditions, etc. that holds scope for improvement. Alternative techniques such as freeze drying[278] can be used in cases specific to the system under consideration. Other novel method for contact-free drying includes utilization of the Leidenfrost effect.[279] in which droplets remain suspended on a cushion of its own vapour. Implementing grazing-incidence *in-situ* SAXS or GI-SAXS[280] in such a setup will furnish the evolution of scattering profiles with the progress of drying. Spraying can be bypassed by acoustic levitation where droplets are suspended by standing acoustic waves, [281] which will give a better droplet size distribution and will facilitate *in situ* SAXS characterizations as well.[282] Fig 6.1(a) depicts the two methods schematically.

The study of drying colloidal droplets can be extended to a variety of scientifically or industrially relevant systems. For example self-assembly is particularly interesting for various anisotropic particles such as patchy particles, having discrete, attractive interaction sites called "patches",[283] Janus particles, which are asymmetric and imparts directional dependence of physical or chemical properties in the same particle,[281] disc or spindle-shaped (Fig. 6.1(b)) particles such as beidellite clay[284] or magnetic haematite,[285] etc. Investigation of EISA in colloidal mixtures composed of lyophilic and lyophobic particles is particularly interesting to understand core/shell phenomena. The role played by the solvent is also crucial during EISA with respect to the DLVO interactions in the system. Various organic solvents, ionic liquids can be used as the dispersant in order to study the ensuing self-assembly in the system.

Encapsulation is a widely used technique in food industries[286] to entrap flavours and active ingredients inside a carrier material. Spray drying technique can prove to be very facile for the synthesis of encapsulated granules. Schematic representation of two types of encapsulated granules is provided in Fig. 6.1(c). For example spay drying of a colloidal mixture of phosphorescent[287] and non-phosphorescent particles to generate composite granules which can then be tuned according to specific structure-function requirements. Along with complementary techniques of imaging and small-angle scattering, fluorescence spectrophotometric studies[288] can also be used to further assay the system. A similar technique can also be used to synthesize composite granules from ferroelectric and non-ferroelectric component colloidal mixture, which can then be tested for energy storage functions.[289] The P-E hysteresis loop is particularly useful in optimizing the component concentration for such applications.

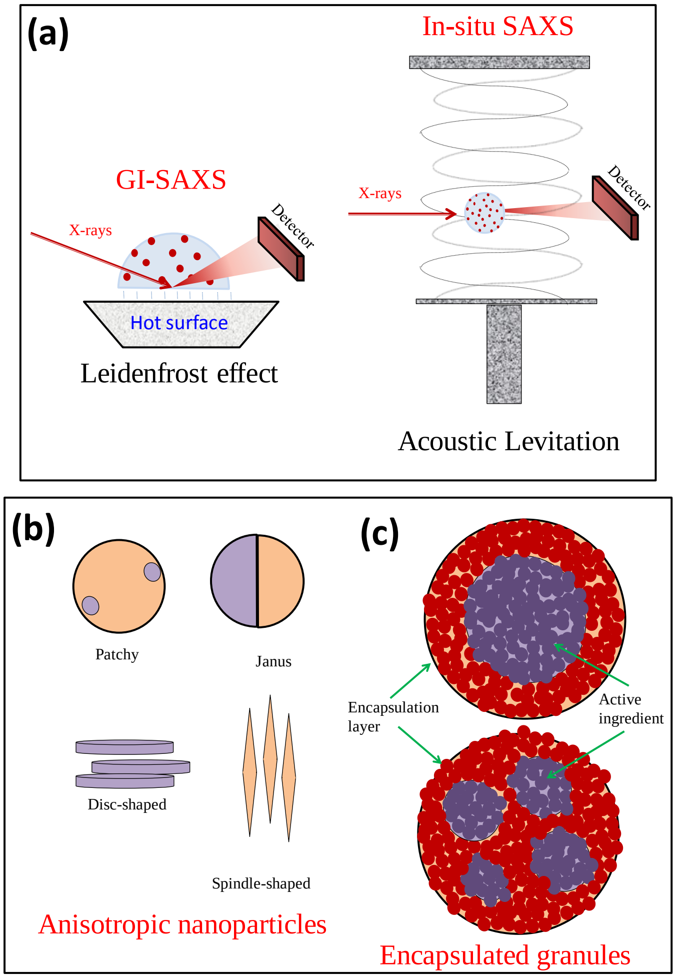

Fig. 6.1 Schematic representations of: **(a)** Alternative methods of contact-free drying of colloidal droplets. **(b)** Different types of anisotropic nanoparticles **(c)** Encapsulated granules.

From the application point of view, on the basis of their inherent porosity, the granules can be modelled for filtration,[269] catalysis,[267-268] etc. Alternative porosity characterization techniques such as mercury porosimetry[290] can be used. Use of Atomic Force Microscopy (AFM) can reveal finer details of the granular surface such as change of slope, etc. AFM is also advantageous to determine physical properties like, stiffness, elasticity, adhesion, magnetic and electrostatic fields, temperature distribution, spreading resistance, conductivity, etc. Element compositional analysis using Energy Dispersed Spectroscopy (EDS), X-ray Photoelectron Spectroscopy (XPS), Nuclear Magnetic Resonance (NMR), etc. can be carried out for multi-component granules.

As an extension of the synthesis and study of CNT-incorporated silica micro-granules described in Chapter 5, microwave absorption studies[291] can be carried out, which shows applicability as absorbing paints, etc. Carbon-doped silica granules will also be beneficial for low-κ dielectric applications in memory devices. Computer simulations of contact-free droplet drying under various extrinsic and intrinsic conditions, mimicking actual experimental conditions using Molecular Dynamics or Monte Carlo techniques is also an exciting unexplored arena of research.

References

1. G. L. Hornyak, J. J. Moore, H. F. Tibbals and J. Dutta, *Fundamentals of Nanotechnology*, CRC Press, Boca Raton, Florida, 2008.
2. M.-H. Education, *McGraw-Hill Dictionary of Scientific and Technical Terms*, 6th edition, McGraw-Hill Professional, 2002.
3. Y. S. Lee, *Self-Assembly and Nanotechnology*, John Wiley & Sons, Hoboken, New Jersey, 2008.
4. J. A. Potton, G. J. Daniell and B. D. Rainford, *J. Appl. Cryst.*, 1988, **21**, 891-897.
5. I. Laoufi, M.-C. Saint-Lager, R. Lazzari, J. Jupille, O. Robach, S. Garaudee, G. Cabailh, P. Dolle, H. Cruguel and A. Bailly, *J. Phys. Chem. C*, 2011, **115**, 4673–4679.
6. A. K. Sinha, S. Seelan, S. Tsubota and M. Haruta, *Top. Catal.*, 2004, **29**, 95-102.
7. A. W. Snow and H. Wohltjen, *Chem. Mater.*, 1998, **10**, 947–949.
8. http://www.nobelprize.org/nobel_prizes/chemistry/laureates/1925/zsigmondy-facts.html.
9. R. Zsigmondy, *Justus Liebigs Ann. Chem.*, 1898, **309**, 29-54.
10. T. Mappes, N. Jahr, A. Csaki, N. Vogler, J. Popp and W. Fritzsche, *Angew. Chem. Int. Ed.*, 2012, **51**, 11208–11212.
11. G. Binnig and H. Rohrer, *IBM J. Res. Dev.*, 1986, **30**, 355-369.
12. H. W. Kroto, J. R. Heath, S. C. O'Brien, R. F. Curl and R. E. Smalley, *Nature*, 1985, **318**, 162-163.
13. K. E. Drexler, *Engines of Creation - The Coming Era of Nanotechnology*, Anchor Books, New York, 1986.
14. http://www.nobelprize.org/nobel_prizes/physics/laureates/1965/feynman-facts.html>.
15. http://metamodern.com/2009/12/29/theres-plenty-of-room-at-the-bottom%E2%80%9D-feynman-1959/.
16. N. Taniguchi, *Proc. Int. Conf. Prod. Eng.*, Tokyo, 1974.
17. E. K. Drexler, *Nanosystems: Molecular Machinery, Manufacturing, and Computation*, Wiley, 1992.
18. http://www.foresight.org/prize/.
19. http://www.kavliprize.org/.

20. http://sites.ieee.org/nanotech/awards/.
21. T. Takagahara and K. Takeda, *Phys. Rev.B*, 1992, **46**, 15578-15581.
22. F. W. Wise, *Acc. Chem. Res.*, 2000, **33**, 773-780.
23. X. Zhao, C. M. Wei, L. Yang and M. Y. Chou, *Phys. Rev. Lett.*, 2004, **92**, 236805.
24. M. Cahay, 6th International Symposium on Quantum Confinement: Nanostructures Materials and Quantum Devices, San Francisco, 2001.
25. H. Haug and S. W. Koch, *Quantum Theory of the Optical and Electronic Properties of Semiconductors*, World Scientific, 1994.
26. A. D. Yoffe, *Adv. Phys.*, 1993, **42**, 173-262.
27. D. J. Norris and M. G. Bawendi, *Phys. Rev. B*, 1992, **53**, 15578.
28. K. J. Klabunde, J. Stark, O. Koper, C. Mohs, D. G. Park, S. Decker, Y. Jiang, I. Lagadic and D. Zhang, *J. Phys. Chem.*, 1996, **100**, 12142-12153.
29. F. Raimondi, G. G. Scherer, R. Kötz and A. Wokaun, *Angew. Chem. Int. Ed.*, 2005, **44**, 2190–2209.
30. G. M. Whitesides and M. Boncheva, *Proc. Nat. Acad. Sci. USA*, 2002, **99**, 4769-4774.
31. H. Sirringhaus, T. Kawase, R. H. Friend, T. Shimoda, M. Inbasekaran, W.Wu and E. P. Woo, *Science*, 2000, **290**, 2123-2126.
32. J. A. Rogers, Z. Bao, K. Baldwin, A. Dodabalapur, B. Crone, V. R. Raju, V. Kuck, H. Katz, K. Amundson, J. Ewing and P. Drzaic, *Proc. Nat. Acad. Sci. USA*, 2001, **98**, 4835-4840.
33. S. A. Jenekhe and X. L. Chen, *Science*, 1999, **283**, 372-375.
34. Y. Xia, B. Gates, Y. Yin and Y. Lu, *Adv. Mater.*, 2000, **12**, 693–713.
35. M. H. Wu and G. M. Whitesides, *Appl. Phys. Lett.*, 2001, **78**, 2273–2275.
36. C. M. Lieber, *Sci. Am.*, 2001, **285**, 58-64.
37. V. I. Klimov, A. A. Mikhailovsky, S. Xu, A. Malko, J. A. Hollingsworth, C. A. Leatherdale, H. Eisler and M. G. Bawendi, *Science*, 2000, **290**, 314-317.
38. S. H. Sun, C. B. Murray, D. Weller, L. Folks and A. Moser, *Science*, 2000, **287**, 1989–1992.
39. J. N. Israelachvili, *Intermolecular and Surface Forces: Revised Third Edition*, Academic Press, 2011.
40. S. E. Aniagyei, C. DuFort, C. C. Kao and B. Dragnea, *J. Mater. Chem.* 2008, **18**, 3763-3774.
41. C. A. Fustin, G. Glasser, H. W. Spiess and U. Jonas, *Langmuir*, 2004, **20**, 9114-9123.
42. J. H. Clint, *Surfactant Aggregation*, Springer, Netherlands, 1992.

43. P. Alexandridis and B. Lindman, *Amphiphilic Block Copolymers: Self - assembly and Applications* Elsevier, Amsterdam, 2000.
44. S. Kralj and D. Makovec, *ACS Nano*, 2015, **9**, 9700–9707.
45. M. Grzelczak, *ACS Nano*, 2010, **4**, 3591–3605.
46. J. Bahadur, D. Sen, S. Mazumder, B. Paul, H. Bhatt and S. G. Singh, *Langmuir*, 2012, **28**, 1914-1923.
47. J. Bahadur, D. Sen, S. Mazumder, B. Paul, A. Khan and G. Ghosh, *J. Colloid Interface Sci.*, 2010, **351**, 357-364.
48. C. J. Brinker, Y. Lu, A. Sellinger and H. Fan, *Adv. Mater.* 1999, **11**, 579-585.
49. D. Grosso, F. Cagnol, G. Soler-Illia, E. L. Crepaldi, H. Amenitsch, A. Brunet-Bruneau, A. Bourgeois and C. Sanchez, *Adv. Funct. Mater.*, 2004, **14**, 309-322.
50. A. Mishra, J. S. Melo, D. Sen and S. F. D'Souza, *J. Colloid Interface Sci.*, 2014, **414**, 33-40.
51. S. Narayanan, J. Wang and X.-M. Lin, *Phys. Rev. Lett.*, 2004, **93**, 135503.
52. T. Narita, P. Hebraud and F. Lequeux, *Eur. Phys. J. E*, 2005, **17**, 69-76.
53. D. Sen, J. Bahadur, S. Mazumder, G. Santoro, S. Yu and S. V. Roth, *Soft Matter*, 2014, **10**, 1621-1627.
54. D. Sen, J. Bahadur, S. Mazumder, G. Verma, P. A. Hassan, S. Bhattacharya, K. Vijai and P. Doshi, *Soft Matter*, 2012, **8**, 1955-1963.
55. J. Xu, J. Xia, S. W. Hong, Z. Lin, F. Qiu and Y. Yang, *Phys. Rev. Lett.*, 2006, **96**, 066104.
56. L. Yang, Y. Zhang, J. Luo, Y. Luo, K. Gao, D. Li and Q. Meng, *Phys. Rev. E*, 2011, **84**, 031605.
57. R. D. Deegan, O. Bakajin, T. F. Dupont, G. Huber, S. R. Nagel and T. A. Witten, *Nature*, 1997, **389**.
58. Y. Lu, B. F. McCaughey, D. Wang, J. E. Hampsey, N. Doke, Z. Yang and C. J. Brinker, *Adv. Mater.*, 2003, **15**.
59. Y. Lu, H. Y. Fan, A. Stump, T. L. Ward, T. Rieker and C. J. Brinker, *Nature*, 1999, **398**, 223-226.
60. M. Etienne, A. Quach, D. Grosso, L. Nicole, C.Sanchez and A. Walcarius, *Chem. Mater.*, 2007, **19**, 844-856.
61. T. S. Glazneva, E. V. Rebrov, J. C. Schouten, E. A. Paukshtis and Z. R. Ismagilov, *Thin Solid Films*, 2007, **515**, 6391-6394.

62. N. Krins, J. D. Bass, D. Grosso, C. Henrist, R. Delaigle, E. M. Gaigneaux, R. Cloots, B. Vertruyen and C.Sanchez, *Chem. Mater.*, 2011, **23**, 4124–4131.
63. J. Bahadur, D. Sen, S. Mazumder, B. Paul and I. G. Sharma, in *International Conference on Physics of Emerging Functional Materials*, eds. D. K. Aswal and A. K. Debnath, **1313**, 2010, 146-148.
64. C. Boissiere, D. Grosso, A. Chaumonnot, L. Nicole and C. Sanchez, *Adv. Mater.*, 2011, **23**, 599-623.
65. F. Iskandar, L. Gradon and K. Okuyama, *J. Colloid Interface Sci.*, 2003, **265**, 296-303.
66. F. Iskandar, I. W. Lenggoro, B. Xia and K. Okuyama, *J. Nanopart. Res.*, 2001, **3**, 263-270.
67. H. Hu and R. G. Larson, *J. Phys. Chem. B*, 2006, **110**, 7090–7094.
68. B. Jirgensons and M. E. Straumanis, *A Short Textbook of Colloid Chemistry*, 2nd Edition, Pergamon, 1962.
69. I. N. Levine, *Physical Chemistry*, 5th Edition., McGraw-Hill, Boston, 2001.
70. N. Vogel, M. Retsch, C.-A. Fustin, A. Campo and U. Jonas, *Chem. Rev.*, 2015, **115**, 6265–6311.
71. B. V. Derjaguin and L. Landau, *Acta Physicochim*, 1941, **14**, 633-662.
72. E. J. W. Verwey and J. T. G. Overbeek, *Theory of the Stability of Lyophobic Colloids*, Elsevier, Amsterdam, 1948.
73. W. B. Russel, D. A. Saville and W. R. Schowalter, *Colloidal Dispersions*, Cambridge University Press, Cambridge, 1989.
74. I. E. Dzyaloshinskii, E. M. Lifshitz and L. P. Pitaevskii, *Soviet Phys. Usp.*, 1961, **4**, 153–176.
75. H. C. Hamaker, *Physica*, 1937, **4**, 1058-1072.
76. P. Debye and E. Hückel, *Phys. Z.*, 1923, **24**, 185-206.
77. C. P. Collier, T. Vossmeyer and J. R. Heath, *Annu. Rev. Phys. Chem.*, 1998, **49**, 371-404.
78. A. D. Dinsmore, J. C. Crocker and A. G. Yodh, *Curr. Opin. Colloid Interface Sci.*, 1998, **3**, 5-11.
79. J. Crocker and D. Grier, *MRS Bulletin*, 1998, **23**, 24-31.
80. P. F. Damasceno, M. Engel and S. C. Glotzer, *Science*, 2012, **337**, 453–457.
81. L. Rossi, S. Sacanna, W. T. M. Irvine, P. M. Chaikin, D. J. Pine and A. P. Philipse, *Soft Matter*, 2011, **7**, 4139–4142.

82. T. D. Nguyen, E. Jankowski and S. C. Glotzer, *ACS Nano*, 2011, **5**, 8892–8903.

83. J. D. Forster, J.-G. Park, M. Mittal, H. Noh, C. F. Schreck, C. S. O'Hern, H. Cao, E. M. Furst and E. R. Dufresne, *ACS Nano*, 2011, **5**, 6695–6700.

84. Y. Zhang, F. Lu, D. van der Lelie and O. Gang, *Phys. Rev. Lett.*, 2011, **107**, 135701–135704.

85. M. R. Jones, R. J. Macfarlane, B. Lee, J. Zhang, K. L. Young, A. J. Senesi and C. A. Mirkin, *Nature Mater.*, 2010, **9**, 913–917.

86. M. R. Jones, R. J. Macfarlane, A. E. Prigodich, P. C. Patel and C. A. Mirkin, *J. Am. Chem. Soc.*, 2011, **133**, 18865–18869.

87. J. Bahadur, D. Sen, S. Mazumder, S. Bhattacharya, H. Frieinghaus and G. Goerigk, *Langmuir*, 2011, **27**, 8404-8414.

88. J. Bahadur, D. Sen, S. Mazumder, P. U. Sastry, B. Paul, H. Bhatt and S. G. Singh, *Langmuir*, 2012, **28**, 11343-11353.

89. A. Khan, D. Sen, P. Kothalkar, B. K. Sapra, S. Mazumder and Y. S. Mayya, *Drying Technol.*, 2012, **30**, 679-686.

90. W. Liu, W. D. Wu, C. Selomulya and X. D. Chen, *Langmuir*, 2011, **27**, 12910-12915.

91. Y. Lu, H. Fan, N. Doke, D. A. Loy, R. A. Assink, D. A. LaVan and C. J. Brinker, *J. Am. Chem. Soc.*, 2000, **122**, 5258–5261.

92. D. Sen, J. Bahadur, S. Mazumder and S. Bhattacharya, *Soft Matter*, 2012, **8**, 10036-10044.

93. D. Sen, S. Mazumder, J. S. Melo, A. Khan, S. Bhattyacharya and S. F. D'Souza, *Langmuir*, 2009, **25**, 6690-6695.

94. D. Sen, J. S. Melo, J. Bahadur, S. Mazumder, S. Bhattacharya, S. F. D'Souza, H. Frielinghaus, G. Goerigk and R. Loidl, *Soft Matter*, 2011, **7**, 5423-5429.

95. D. Sen, J. S. Melo, J. Bahadur, S. Mazumder, S. Bhattacharya, G. Ghosh, D. Dutta and S. F. D'Souza, *Eur. Phys. J. E*, 2010, **31**, 393-402.

96. D. Sen, O. Spalla and A. Thill, in *Doped Nanopowders: Synthesis, Characterisation Applications*, eds. W. Lojkowski, J. R. Blizzard, U. Narkiewicz and J. D. Fidelus, 2007, **128**, 73-80.

97. J. Bahadur, D. Sen, S. Mazumder, B. Paul and A. Khan, *Int J Nanosci.*, 2011, **10**, 995-999.

98. S. Lyonnard, J. R. Bartlett, E. Sizgek, K. S. Finnie, T. Zemb and J. L. Woolfrey, *Langmuir*, 2002, **18**, 10386-10397.

99. K. Master, *Spray Drying Handbook*, Longman Scientific & Technical: Harlow, Essex, U.K, 1991.

100. J. S. Melo, D. Sen, S. Mazumder and S. F. D’Souza, *Soft Matter*, 2013, **9**, 805-810.

101. L. Peltonen, H. Valo, R. Kolakovic, T. Laaksonen and J. Hirvonen, *Expert Opin. Drug Deliv.*, **7**, 705-719.

102. D. Sen, A. Khan, J. Bahadur, S. Mazumder and B. K. Sapra, *J. Colloid Interface Sci.*, 2010, **347**, 25-30.

103. D. Sen, O. Spalla, O. Tache, P. Haltebourg and A. Thill, *Langmuir*, 2007, **23**, 4296-4302.

104. A. Thill and O. Spalla, *J. Colloid Interface Sci.*, 2005, **291**, 477-488.

105. K. Waldron, Z. Wu, W. D. Wu, W. Liu, D. Zhao, X. D. Chen and C. Selomulya, *J. Mater. Chem. A*, 2014, **2**, 19500-19508.

106. K. Waldron, W. D. Wua, Z. Wua, W. Liu, C. Selomulya, D. Zhao and X. D. Chen, *J. Colloid Interface Sci.*, 2014, **418**, 225–233.

107. A. Gharsallaoui, G. Roudaut, O. Chambin, A. Voilley and R. Saurel, *Food Res. Int.*, 2007, **40**, 1107–1121.

108. http://www.synthite.com/synthite/our-products/Industrial-Products-By-Category/Encapsulated-and-Spray-Dried.

109. M. Jain, G. Lohare, M. Bar, R. Chavan, S. Barhate and C. Shah, Res. J. Pharma. Dosage Forms and Tech., 2012, **4**, 74-79.

110. J. Patil, *J. Pharmacovigil.*, 2016, **4**, 2.

111. Y. I. Rabinovich, M. S. Esayanur and B. M. Moudgil, *Langmuir*, 2005, **21**, 10992–10997.

112. L. Aragao-Santiago, H. Hillaireau, N. Grabowski, S. Mura, T. L. Nascimento, S. Dufort, J. L. Coll, N. Tsapis and E. Fattal, *Nanotoxicology*, 2016, **10**, 292-302.

113. H. Bahadar, F. Maqbool, K. Niaz and M. Abdollahi, *Iran Biomed J.*, 2016, **20**, 1-11.

114. A. B. D. Nandiyanto and K. Okuyama, *Adv. Powder Technol.*, 2011, **22**, 1-19.

115. E. Lintingre, F. Lequeux, L. Talini and N. Tsapis, *Soft Matter*, 2016, **12**, 7435-7444.

116. M. R. Lauro, C. Carbone, F. Sansone, B. Ruozi, R. Chillemi, S. Sciuto, R. P. Aquino and G. Puglisi, *Drug Dev. Ind. Pharm.*, 2016, **42**, 1127–1136.

117. L. Chen, T. Okuda, X. Y. Lu and H. K. Chan, *Adv. Drug Deliv. Rev.*, 2016, **100**, 102–115.

118. C. Anandharamakrishnan and P. I. S, *Spray Drying Techniques for Food Ingredient Encapsulation*, 1st Edition., John Wiley & Sons, 2015.

119. S. H. Anwar and B. Kunz, *J. Food Eng.*, 2011, **105**, 367–378.
120. M. Ameri and Y. F. Maa, *Drying Technol.*, 2006, **24**, 763–768.
121. R. Vehring, *Pharm. Res.*, 2008, **25**, 999–1022.
122. D. F. Cortés-Rojas and W. P. Oliveira, *Drying Technol.*, 2012, **30**, 921–934.
123. P. B. Fourie, W. A. Germishuizen, Y.-L. Wong and D. A. Edwards, *Expert Opin. Biol. Ther.* 2008, **8**, 857-863.
124. D. McAdams, D. Chen and D. Kristensen, *Expert Rev. Vaccines*, 2012, **10**, 1211-1219.
125. S. Y. Lee, L. Gradon, S. Janeczko, F. Iskandar and K. Okuyama, *ACS Nano*, 2010, **4**, 4717-4724.
126. A. Frohn and N. Roth, *Dynamics of droplets*, Springer−Verlag, Berlin, 2000.
127. V. Paramita, K. Iida, H. Yoshii and T. Furuta, *Drying Technol.*, 2010, **28**, 323-329.
128. W. Gauvin and S. Katta, *AIChE J.*, 1976, **22**, 713–724.
129. J. Plateau, *Experimental and theoretical statics of liquids subject to molecular forces only*, Gauthier-Villars, Paris, 1873.
130. W. D. Wu, W. Liu and T. Gengenbach, *J. Food Eng.*, 2014, **123**, 130–135.
131. S. K. Aslanov, *Tech. Phys.*, 1999, **44**, 1386-1387.
132. S. P. Lin and Z. W. Lian, *AIAA J.*, 1990, **28**, 120-126.
133. C. Weber, *J. Appl Math. Mech.*, 1931, **11**, 136–154.
134. W. V. Ohnesorge, *J. Appl Math. Mech.*, 1936, **16**, 355–358.
135. K. Murali, S. M. Kannan and M. S. Prabhu., *Am. J. Eng. Res.*, 2014, **3**, 339–345.
136. I. C. Kemp, T. Hartwig, R. Herdman, P. Hamilton, A. Bisten and S. Bermingham, *Drying Technol.*, 2015, **34**, 1243-1252.
137. F. T. Turan, A. Cengiz and T. Kahyaoglu, *Innov. Food Sci. Emerg. Technol.*, 2015, **32**, 136-145.
138. H. Lixin, K. Kumar and A. S. Majumdar, *Russia TSTU Trans.*, 2004, **10**, 83–100.
139. A. Jaworek, *Powder Technol.*, 2007, **176**, 18-35.
140. R. B. Keey and Q. T. Pham, *Chem. Eng.*, 1976, **311**, 516-521.
141. D. E. Oakley, *Drying Technol.*, 2004, **22**, 1371–1402.
142. P. Seydel, J. Blomer and J. Bertling., *Drying Technol.*, 2006, **24**, 137–146.
143. A. Dolinsky, *Drying Technol.*, 2001, **19**, 785–806.
144. M. Farid, *Chemical Engineering Science*, 2003, **58**, 2985–2993.

145. C. M. Gohel, R. K. Parikh, S. A. Nagori, A. V. Gandhi and T. C. Patel, *Pharm. Rev.*, 2009, **7**, 1-23.
146. D. E. Dobry, D. M. Settell, J. M. Baumann, R. J. Ray, L. J. Graham and R. A. Beyerinck, *J. Pharm. Innov.*, 2009, **4**, 133–142.
147. A. J. Hoekstra, 2000, ‘Gas Flow Field and Collection Efficiency of Cyclone Separators’, the Delft University of Technology, Delft, 2000.
148. L. Theodore and A. J. Buonicore, *Industrial Air Pollution Control for Particulates*, CRC Press, Cleveland, OH, 1976.
149. H. P. Huinink, L. Pel and M. A. J. Michels, *Phys. Fluids*, 2002, **14**, 1389−1395.
150. N. Tsapis, D. Bennett, B. Jackson, D. A. Weitz and D. A. Edwards, *Proc. Nat. Acad. Sci. USA*, 2002, **99**, 12001-12005.
151. N. Tsapis, E. R. Dufresne, S. S. Sinha, C. S. Riera, J. W. Hutchinson, L. Mahadevan and D. A. Weitz, *Phys. Rev. Lett.*, 2005, **94**, 0183021-0183024.
152. L. Pauchard and Y. Couder, *Europhys. Lett.*, 2004, **66**, 667-673.
153. L. Pauchard and C. Allain, *Europhys. Lett.*, 2003, **62**, 897-903.
154. H. M. van der Kooij, G. T. van der Kerkhof and J. Sprakel, *Soft Matter*, 2016, **12**, 2858–2867.
155. É. Lintingre, G. Ducouret, F. Lequeux, L. Olanier, T. Périé and L. Talini, *Soft Matter*, 2015, **11**, 3660-3665.
156. S. P. Timoshenko and J. M. Gere, *Theory of Elastic Stability*, McGraw Hill, New York, 1961.
157. J. A. Yanez, T. Shikata, D. S. Pearson and F. F. Lange, *J. Am. Ceram. Soc.*, 1996, **79**, 2917–2924.
158. G. W. Scherer, *Journal of Non-Crystalline Solids*, 1997, **215**, 155–168.
159. J. S. Pedersen, *Adv. Colloid Interface Sci.*, 1997, **70**, 171-210.
160. R. D. Preston, *The physical biology of plant cell walls*, Chapman and Hall, London, 1974.
161. C. G. Golding, L. L. Lamboo, D. R. Beniac and T. F. Booth, *Sci. Rep.*, 2016, **6**, 26516.
162. C.Alfonso, J.M.Bermond, J.C.Heyraud and J.J.Métois, *Surf. Sci.*, 1992, **262**, 371-381.
163. T. Zemb and P. Lindner, *Neutron, X-rays and Light. Scattering Methods Applied to Soft Condensed Matter*, Elsevier, Amsterdam, 2002.
163. O. Glatter and O. Kratky, *Small Angle X-ray Scattering*, Academic Press, New York, 1982.

164. A. Guinier, G.Fournet, B. C. Walker and L.K.Yudowith, *Small angle scattering of X-rays*, Wiley, New York, 1955.
165. U. Valdre, *Electron Microscopy In Material Science*, Academic Press, New York, 1971.
166. W. Burchard, *Static and dynamic light scattering from branched polymers and biopolymers*, Springer, Berlin, 1983.
167. L. A. Feigin and D. I. Svergun, *Structural Analysis by Small Angle X-Ray and Neutron Scattering*, Plenum Press, New York, 1987.
168. W. Zhou and Z. L. Wang, *Scanning Microscopy for Nanotechnology*, Springer, New York, 2006.
169. K. Kanaya and S. Okayama, *J. Phys. D: Appl. Phys.*,1972, **5**, 43-58.
170. A. Fleming, *J. Sci. Instrum.*, 1934, **11**, 44.
171. R. Shimizu, Y. Kataoka, S. Kawai and T. Tanaka, *Appl. Phys. Lett.*, 1975, **27**, 113-114.
172. J. B. McGinn, L. W. Swanson, N. A. Martin, M. A. Gesley and M. A. McCord, *J. Vac. Sci. Technol. B* 1991, **9**, 2925-2928.
173. A. V. Crewe, D. N. Eggenberger, J. Wall and L. M. Welter, *Rev. Sci. Instrum.*, 1968, **39**, 576-583.
174. J. Goldstein, D. E. Newbury, P. Echlin, D. C. Joy, C. E. Lyman, E. Lifshin, L. Sawyer and J. R. Michae, *Advanced Scanning Electron Microscopy and X-Ray Microanalysis*, Springer, Boston, 1986.
175. P. Krishnamurti, *Indian J. Phys.*, 1930, **5**, 473–486.
176. P. Debye and A. Bueche, *J. Appl. Phys.*, 1949, **28**, 679.
177. G. Porod, *Kolloid-Z*, 1951, **124**, 83-114.
178. J. S. Higgins and R. S. Stein, *J. Appl. Crystallogr.*, 1978, **11**, 346-375.
179. G. Kostorz, *Treatise Mater. Sci. Technol.*, 1979, **15**, 227-289.
180. W. Schmatz, T. Springer, J. Schelten and K. Ibel, *J. Appl. Crystallogr.*, 1974, **7**, 96-116.
181. C. G. Windsor, *J. Appl. Crystallogr.*, 1988, **21**, 582-588.
182. J. S. Pedersen, *J. Appl. Crystallogr.*, 1994, **27**, 595-608.
183. C. G. Darwin, *Philos. Mag.*, 1914, **27**, 315-333.
184. S. Mazumder, D. Sen, T. Saravanan and P. R. Vijayaraghavan, *J. Neutron Res.*, 2001, **9**, 39-57.
185. J. A. Lake, *Acta Crystallogr.*, 1967, **23**, 191-194.

186. I. Breßler, J. Kohlbrecher and A. F. Thünemann, *J. Appl. Cryst.*, 2015, **48**, 1587-1598.
187. P. A. Kralchevsky and K. Nagayama, *Langmuir*, 1994, **10**, 23-36.
188. P. Biswas, D. Sen, S. Mazumder, C. B. Basak and P. Doshi, *Langmuir*, 2016, **32**, 2464-2473.
189. K. A. Brakke, *Exp. Math.*, 1992, **1**, 141-165.
190. B. J. Frisken, *Appl. Opt.*, 2001, **40**, 4087-4091.
191. J. Aitchison and J. A. C. Brown, *The Lognormal Distribution*, Cambridge University Press, 1957.
192. R. J. Baxter, *J. Chem. Phys.*, 1968, **49**, 2770-2774.
193. J. Teixeira, *J. Appl. Cryst.*, 1988, **21**, 781-785.
194. T. Freltoft, J. K. Kjems and S. K. Sinha, *Phys. Rev. B*, 1986, **33**, 269-275.
195. G. Beaucage, H. K. Kammler and S. E. Pratsinis, *J. Appl. Cryst.*, 2004, **37**, 523-535.
196. F. Mezei, *Z. Phys.*, 1972, **255**, 146-160.
197. R. Pynn, *Neutron Spin-Echo and Three-Axis Spectroscopy*, Springer, Berlin, 1980.
198. R. Gähler, R. Golub, K. Habicht, T. Keller and J. Felber, *Physica B*, 1996, **229**, 1-100.
199. M. T. Rekveldt, *J. Appl. Phys.*, 1998, **84**, 31-37.
200. M. T. Rekveldt, W. G. Bouwman, W. H. Kraan, O. Uca, S. Grigoriev, K. Habicht and T. Keller, *Elastic Neutron Scattering Measurements using Larmor Precession of Polarised Neutrons*, Springer, Berlin, 2003.
201. M. T. Rekveldt, W. G. Bouwman, W. H. Kraan, O. Uca, S. Grigoriev and R. Kreuger, *Technical Aspects of Larmor Precession with Inclined Front and End Faces*, Springer, Berlin, 2003.
202. O. Uca, W. G. Bouwman and M. T. Rekveldt, *J. Appl. Crystallogr.*, 2003, **36**, 109–116.
203. M. Rekveldt, J. Plomp, W. G. Bouwman, W. H. Kraan, S. Grigoriev and M. Blaauw, *Rev. Sci. Instrum.*, 2005, **76**, 33901–33909.
204. F. Mezei, *Neutron Spin-Echo*, Springer, Berlin, 1980.
205. T. Krouglov, I. M. de Schepper, W. G. Bouwman and M. T. Rekveldt, *J. Appl. Crystallogr.*, 2003, **36**, 1417-1423.
206. W. G. Bouwman, T. Krouglov, J. Plomp, S. V. Grigoriev, W. H. Kraan and M. T. Rekveldt, *Physica B*, 2004, **350**, 140–146.

207. R. Andersson, L. F. van Heijkamp, I. M. de Schepper and W. G. Bouwman, *J. Appl. Crystallogr.*, 2008, **41**, 868-885.
208. R. Piazza and A. Parola, *J. Phys. Condens. Mat.*, 2008, **20**, 153102.
209. K. Hirota and O. Kimura, *Bull. Chem. Soc. Japan*, 1943, **18**, 111-116.
210. R. Rusconi, L. Isa and R. Piazza, *J. Opt. Soc.Am.*, 2004, **21**, 605-616.
211. H. Ning, J. K. G. Dhont and S. Wiegand, *Langmuir*, 2008, **24**, 2426-2432.
212. P. G. Hartley, I. Larson and P. J. Scales, *Langmuir*, 1997, **13**, 2207-2214.
213. F. Boulogne, F. Giorgiutti-Dauphin´e and L. Pauchard, *Soft Matter*, 2013, **9**, 750-757.
214. C. Quilliet, C. Zoldesi, C.Riera, A. van Blaaderen and A. Imho, *Eur. Phys. J. E*, 2008, **27**, 13-20.
215. L. D. Landau and E. M. Lifshitz, *Theory of Elasticity* Pergamon Press, 1970.
216. R. A. Donald, P. F. Pradeep and J. W. Wendelin, *Cengage Learning*, 2011, 84-86.
217. S. Brunauer, P. H. Emmett and E. Teller, *J. Am. Chem. Soc.*, 1938, **60**, 309-319.
218. M. Kruk and M. Jaroniec, *Chem.Mater.*, 2001, **13**, 3169-3183.
219. K. S. W. Sing, *Pure Appl. Chem.*, 1985, **57**, 603-619.
220. R. Schmidt, E. W. Hansen, M. Stoecker, D. Akporiaye and Ole Henrik Ellestad, 117, 4049, *J. Am. Chem. Society*, 1995, **117**, 4049–4056.
221. https://patents.google.com/patent/US3263484.
222. F. Akhtar, L. Andersson, S. Ogunwumi, N. Hedin and L. Bergström, *J. Euro. Ceram. Soc.*, 2014, **34**, 1643-1666.
223. S. L. Suib, *Acc. Chem. Res.*, 2008, **41**, 479-487.
224. C. Klaysom, R. Marschall, S.-H. Moon, B. P. Ladewig, G. Q. M. Lu and L. Wang, *J. Mater. Chem.*, 2011, **21**, 7401-7409.
225. G. Ahuja and K. Pathak, *Indian J. Pharm. Sci.*, 2009, **71**, 599-607.
226. P. Biswas, D. Sen, S. Mazumder and J. Ramkumar, *Colloids Surf. A*, 2017, **520**, 279-288.
227. J. Majeed, J. Ramkumar, S. Chandramouleeswaran, O. D. Jayakumar and A. K. Tyagi, *RSC Adv.*, 2013, **3**, 3365-3373.
228. S. Meng, J. Ren and E. Kaxiras, *Nano Lett.*, 2008, **8**, 3266-3272.
229. S.-M. Alatalo, E. Makila, E. Repo, M. Heinonen, J. Salonen, E. Kukk, M. Sillanpaa and M.-M. Titirici, *Green Chem.*, 2016, **18**, 1137-1146.
230. http://www.rxlist.com/prosed-ds-drug.htm.

231. B. Mokhlesi, J. B. Leikin, P. Murray and T. C. Corbridge, *Chest*, 2003, **123**, 897–922.
232. C. Pelekani and V. L. Snoeyink, *Carbon*, 2000, **38**, 1423-1436.
233. H. Förster, *Molecular Sieves – Science and Technology*, 2004, **4**, 337-426.
234. S. Venkateswaran, R. Yuvakkumar and V. Rajendran, *Phosphorus Sulfur Silicon Relat. Elem.*, 2012, **188**, 1178-1193.
235. K. Bergmann and C. T. O'Konski, *J. Phys. Chem.*, 1963, **67**, 2169-2177.
236. G. H. John Canning, Miles Ma, Alison Beavis, David Bishop, Kevin Cook, Andrew McDonagh, Dongqi Shi, Gang-Ding Peng and Maxwell J. Crossley, *Nanomaterials*, 2014, **4**, 157-174.
237. Y. Umemura, E. Shinohara and R. A. Schoonheydt, *Phys. Chem. Chem. Phys.*, 2009, **11**, 9804-9810.
238. K. Patil, R. Pawar and P. Talap, *Phys. Chem. Chem. Phys.*, 2000, **2**, 4313-4317.
239. R. Bud and D. J. Warner, *Instruments of Science: An Historical Encyclopedia*, Taylor & Francis, Washington, 1998.
240. M. J. Vold, *Anal. Chem.*, 1949 **21**, 683–688.
241. R. M. Prakash R. Somani, A.K. Viswanath, S. Radhakrishnan, *Polym. Degrad. Stab.*, 2003, **79**, 77–83.
242. C. Tsioptsias, A. Stefopoulos, I. Kokkinomalis, L. Papadopoulou and C. Panayiotou, *Green Chem.*, 2008, **10**, 965-971.
243. V. R. Patel and M. M. Amiji, *Pharm. Res.*, 1996, **13**, 588-593.
244. D. J. Bennett, R. P. Burford, T. P. Davis and H. J. Tilley, *Polym. Int.*, 1995, **36**, 219-226.
245. K. Kabiri, H. Omidian and M. J. Zohuriaan-Mehr, *Polym. Int.*, 2003, **52**, 1158-1164.
246. S. Hjertén, J.-L. Liao and R. Zhang, *J. Chromatogr. A*, 1989, **473**, 273-275.
247. C. D. Wood and A. I. Cooper, *Macromolecules*, 2001, **34**, 5-8.
248. H. Everett, *Pure Appl. Chem.*, 1972, **31**, 577-638.
249. D.-H. Choi and R. Ryoo, *J. Mater. Chem.*, 2010, **20**, 5544-5550.
250. C. T. Kresge, M. E. Leonowicz, W. J. Roth, J. C. Vartuli and J. S. Beck, *Nature*, 1992, **359**, 710-712.
251. F. S. An-Hui Lu, *CR Chim*, 2005, **8**, 609–620.
252. F. L. Braghiroli, V. Fierro, J. Parmentier, A. Pasc and A. Celzard, *Green Chem.*, 2016, **18**, 3265-3271.

253. J. Puputti, H. Jin, J. Rosenholm, H. Jiang and M. Lindén, *Microporous Mesoporous Mater.*, 2009, **126**, 272-275.
254. F. R. C. Silva, A. Knoechelmann, M. Benachou and C. A. M. Abreu, *Braz. J. Chem. Eng.*, 1997, **14**, 1678-4383.
255. P. Biswas, D. Sen, S. Mazumder, J. S. Melo, C. B. Basak and K. Dasgupta, *Colloids Surf. B*, 2017, **154**, 421–428.
256. G. Bylund, *Dairy processing handbook*, Tetra Pak Processing Systems AB, 2003.
257. D. Sen, J. Bahadur, S. Mazumder and S. Bhattacharya, *Soft Matter*, 2012, **8**, 10036-10044.
258. R. Bracewell, *The Fourier Transform and Its Applications*, 3rd Edition, McGraw-Hill Book Co., New York, 1999.
259. D. Sen, O. Spalla, L. Belloni, T. Charpentier and A. Thill, *Langmuir*, 2006, **22**, 3798-3806.
260. B. Li, Y.-P. Cao, X.-Q. Feng and H. Gao, *Soft Matter*, 2012, **8**, 5728-5745.
261. X. Han, Y. Zhao, Y. Cao and C. Lu, *Soft Matter*, 2015, **11**, 4444-4452.
262. K. S. Y. Tokudome, T. Kitanaga and M. Takahashi, *Sci. Rep.*, 2012, **2**, 683.
263. D. Y. Khang, J. A. Rogers and H. H. Lee, *Adv. Funct. Mater.*, 2009, **19**, 1526−1536.
264. G. X. Gao, X. Chen and C. R. Li, *Phys. Rev. Lett.*, 2008, **100**, 36102.
265. J. Yin, X. Han, Y. Cao and C. Lu, *Sci. Rep.*, 2014, **4**, 5710.
266. D. Breid and A. J. Crosby, *Soft Matter*, 2013, **9**, 3624–3630.
267. Y. Teraoka, H. Kakebayashi, I. Moriguchi and S. Kagawa, *Electrochemistry*, 1996, **64**, 1189-1194.
268. A. Murugadoss and A. Chattopadhyay, *J. Phys. Chem. C*, 2008, **112**, 11265–11271.
269. A. Das, D. Sen, S. Mazumder, A. K. Ghosh, C. B. Basak and K. Dasgupta, *RSC Adv.*, 2015, **5**, 85052-85060.
270. T.-H. Kim, C. Doe, S. R. Kline and S.-M. Choi, *Adv. Mater.*, 2007 **19**, 929–933.
271. T.-H. Kim, S. M. Choi and S. R. Kline, *Langmuir*, 2006, **22**, 2844-2850.
272. K. Li and Y. Chen, *Colloids Surf. A,* 2012, **415**, 218-229.
273. A. Ortega and J. G. De la Torre, *J. Chem. Phys.*, 2003, **119**, 9914-9919.
274. A. Maestro, E. Guzman, E. Santini, F. Ravera, L. Liggieri, F. Ortega and R. G. Rubio, *Soft Matter*, 2012, **8**, 837–843.
275. H. Yamawaki, M.Yoshida, Y. Kakudate, S. Usuba, H. Yokoi, S. Fujiwara, K. Aoki, R. Ruoff, R. Malhotra and D. Lorents, *J. Phys. Chem.*, 1993, **97**, 11161-11163.

276. A. Jorio, M. A. Pimenta, A. G. S. Filho, R. Saito, G. Dresselhaus and M. S. Dresselhaus, *New J. Phys.*, 2003, **5**, 139.131–139.117.

277. K. Ishikiriyama and M. Todoki, *Thermochim. Acta*, 1995, **256**, 213-226.

278. J. I. Lombrana, *Advances in Food Dehydration*, CRC Press, London, 2008.

279. B. S. Gottfried, C. J. Lee and K. J. Bell, *Int. J. Heat Mass Transfer,* 1966, **9**, 1167–1187.

280. J. R. Levine, J. B. Cohen, Y. W. Chung and P. Georgopoulos, *J. Appl. Cryst.*, 1989, **22**, 528-532.

281. D. Foresti, M. Nabavi, M. Klingauf, A. Ferrari and D. Poulikakos, *Proc. Nat. Acad. Sci. USA*, 2013, **110**, 12549–12554.

282. J. Schuster, R. Kohn, M. Doblinger, A. Keilbach, H. Amenitsch and T. Bein, *J. Am. Chem. Soc.*, 2012, **134**, 11136−11145.

283. Z. Zhang and S. C. Glotzer, *Nano Lett.*, 2004, **4**, 1407-1413.

284. E. Paineau, K. Antonova, C. Baravian, I. Bihannic, P. Davidson, I. Dozov, M. Imperor-Clerc, P. Levitz, A. Madsen, F. Meneau and L. J. Michot, *J. Phys. Chem. B,* 2009, **113**, 15858-15869.

285. K. Ohno, Y. Huang, A.Tsuchida and T. Okubo, *Colloid Polym. Sci.*, 2014 **292**, 723–731.

286. V. Nedovica, A. Kalusevica, V. Manojlovicb, S. Levica and B. Bugarskib, *Procedia Food Sci.*, 2011, **1**, 1806-1815,.

287. M. P. Lettinga, M. A. M. J. van Zandvoort, C. M. van Kats and A. P. Philipse, *Langmuir*, 2000, **16**, 6156-6165.

288. J. R. Lakowicz, *Principles of Fluorescence Spectroscopy*, 3rd Edition, Plenum Press, New York, 1999.

289. J. Gao, Y. Wang, Y. Liu, X. Hu, X. Ke, L. Zhong, Y. He and X. Ren, *Sci. Rep.*, 2017, **7**.

290. H. M. Rootare, *Advanced Experimental Techniques in Powder Metallurgy*, Springer, Boston, 1970.

291. H. Zhang, G. Zeng, Y. Ge, T. Chen and L. Hu, *J. Appl. Phys.*, 2009, **105**, 54314-54318.